ISTANBUL TECHNICAL UNIVERSITY ★ GRADUATE SCHOOL OF SCIENCE ENGINEERING AND TECHNOLOGY

INVESTIGATION OF HYBRID PERMANENT MAGNET ROTOR TOPOLOGY

M.Sc. THESIS

Oğuz KORMAN

Department of Electrical Engineering

Electrical Engineering Programme

JUNE 2018

ISTANBUL TECHNICAL UNIVERSITY ★ GRADUATE SCHOOL OF SCIENCE ENGINEERING AND TECHNOLOGY

INVESTIGATION OF HYBRID PERMANENT MAGNET ROTOR TOPOLOGY

M.Sc. THESIS

Oğuz KORMAN

504151051

Department of Electrical Engineering

Electrical Engineering Programme

Thesis Advisor: Asoc. Prof. Güven KÖMÜRGÖZ

JUNE 2018

ISTANBUL TEKNİK ÜNİVERSİTESİ ★ FEN BİLİMLERİ ENSTİTÜSÜ

HİBRİT KALICI MIKNATISLI ROTOR TOPOLOJİSİNİN İNCELENMESİ

YÜKSEK LİSANS TEZİ

Oğuz KORMAN

504151051

Elektrik Mühendisliği Anabilim Dalı

Elektrik Mühendisliği Program

Tez Danışmanı: Doç. Dr. Güven KÖMÜRGÖZ

HAZİRAN 2018

Oğuz KORMAN, a M.Sc. student of İTU Graduate School of Science Engineering and Technology student ID 504151051, successfully defended the thesis/dissertation entitled "INVESTIGATION OF HYBRID PERMANENT MAGNET ROTOR TOPOLOGY", which he/she prepared after fulfilling the requirements specified in the associated legislations, before the jury whose signatures are below.

Thesis Advisor:	**Assoc. Prof. Güven Kömürgöz** İstanbul Technical University	……
Jury Member:	**Assoc. Prof. Kamuran Nur Bekiroğlu** Yildiz Technical University	……
	Asst. Prof. Derya Ahmet Kocabaş İstanbul Technical University	……

Date of Submission : 2 May 2018
Date of Defense : 11 June 2018

FOREWORD

I would like to express my sincere gratitutes to my supervisor Asoc. Prof. Güven KÖMÜRGÖZ, who guided, informed and helped in creation of this work. It has been very experiencing to work with her.

I am very thankful to AKIM METAL TİC. AŞ. for their generous support in the prototyping and testing.

I am extremely grateful to my colleagues Zuhal TAŞÇI, Enes Maksut KOCABALKAN, Burak ÖZDİNÇER, Hakan KOCAKOYUN and former colleague Oğuzhan OCAK for their both technical and moral supports.

I want to thank to my mother Ayşe Şule EDES, my brother Yavuz KORMAN and my father Fetin KORMAN for having faith in me and supporting me. Special thanks goes to my grandmother Ayfer EDES and my grandfather Mustafa Yüksel EDES for their endless support, back up and encouragement.

Lastly I want to thank all of my friends, colleagues and my dear friend İnci ERBİLEN for being there for me when I needed.

May 2018 Oğuz KORMAN

TABLE OF CONTENTS

Page

ABBREVIATONS

SPM	**:** Surface permament magnet
IPM	**:** Internal permanent magnet
THD	**:** Total Harmonic Distortion
BLDC	**:** Brushless DC Motor
DC	**:** Direct Current
AC	**:** Alternating Current
PMSM	**:** Permanent Magnet Synchronous Motor
BEMF	**:** Back Electromotive Force

SYMBOLS

B_r **:** Remanence of magnet

$B_{r-\vartheta i}$ **:** Remanence of magnet at initial temperature

ϑ_i : Initial temperature of magnet

ϑ_f : Final temperature of magnet

a_B : Temperature coefficient for remanence

Hc : Coercivity of magnet

a_H :Temperature coefficient for remancne

$H_{c-\vartheta i}$: Coercivity of magnet at initial temperature

f : Frequency

n_s : Synchronous speed

p : Number of pole pair(s)

B_{mg} : Peak value of the air gap flux density

B_{mg1} : Peak value of the first harmonic of air gap flux density

a_i : Average to maximum value of the air gap magnetic flux density

E : RMS value of the phase induced voltage

N : Number of turns of one phase

k_w : Winding factor

k_{w1} : Winding factor of first harmonic

ϕ : Flux

ϕ_f : Fundamental component of flux

τ : Pole pitch

L_i : Effective length of the machine

k_{p1} : First harmonic of the pitch factor

k_s : First harmonic of the skew factor

Q : Number of slots per pole per phase

γ : Phase spread

w_s : Coil span in number of slots

m : Number of phases

ζ : Skew in number of slots

A_m : Specific electric loading

I_p : Peak current

D_{si} : Stator inner diameter

J_{RMS} : RMS value of the current density

s_a : Cross section area of all conductors

σ_F : Magnetic stress on surface

σ_{Fn} : Normal component of magnetic stress

$\sigma_{F\tan}$: Tangentinal component of magnetic stress

μ_0 : Permeability of air

H : Magnetic field strength

H_n : Normal component of magnetic field strength

$H_{\tan}$: Tangentinal component of magnetic field strength

$B_{\tan}$: Tangentinal component of flux density

B_n : Normal component of flux density

A_{m-RMS} : RMS value of the specific electric loading

$\cos\varphi$: Power factor

r_r : Rotor radius

S_r : Rotor surface

D_r : Rotor diameter

l' : Rotor length

L_d : Direct axis inductance

L_q : Quadrature axis inductance

L_{md} : Direct-axis magnetizing inductance

L_{mq} : Quadrature-axis magnetizing inductance

$L_{s\sigma}$: Leakage inductance

δ_{def} : Effective air gap length in d-axis

δ_{qef} : Effective air gap length in q-axis

I_{RMS} : RMS value of the stator current

R_s : Resistance of stator windings

δ_{skin} : Skin depth

ω : Angular frequency of current

σ : Electrical conductivity

μ_{cond} : Permeability of conductor

P_{core} : Core loss

k_h : Hystheresis loss coefficient

k_c : Eddy current loss coefficient

k_e : Excess eddy current loss coefficient

P_{m-eddy} : Eddy current loss in permanent magnet

V_m : Volume of permanent magnets

b_m : Width of permanent magnet

ρ_m : Resistivity of permanent magnet

$P_{Windage}$: Windage loss

C_D : Skin friction coefficient for turbulent flow

ρ_d : Density of fluid

r : Radius of rotor

w : Rotation speed of motor

μ : Kinematic viscosity of fluid

l_{gap} : Radial length of air gap

$P_{Bearing}$: Bearing loss

k_b : Bearing loss constant

F_b : Force acting on the bearing

D_b : Bearing inner diameter

$\mathbf{B_{st}}$: Flux density in stator teeth

$\mathbf{B_{sy}}$: Flux density in stator yoke

LIST OF TABLES

Page

LIST OF FIGURES

Page

INVESTIGATION OF HYBRID PERMANENT MAGNET ROTOR TOPOLOGY

SUMMARY

With increasing concerns about environment, technology is evolving towards more efficient usage of materials. The key is to get better performance with less or the same amount of material. Electric motors are one of the most popular research topics in these concerns because it provides mechanical rotation with electrical excitation which is used in almost every single application in world. Moreover, electrical energy is mostly produced and consumed by electric machines and this makes efficient use of materials building up electric machines very critical.

For some decades, with the usage of high performance permanent magnets and electrical steel, permanent magnet electric motors find place in applications where induction machines, electrically excited synchronous mahines and DC (brushed) machines mainly used. Especially with the increased usage of wind turbines and electric vehicles, popularity of permanent magnet machines (both DC and AC) has peaked and this lead to major broadening in the PM motor research field. Many different stator and rotor types are investigated, improved and proposed for obtaining better characteristics by detailed work and pushing the limits.

In this thesis, a recently propesed hybrid permanent magnet strcture is investigated in order to determine the limits and capabilities. In the literature view part, history of electric machines are broadly mentioned and then detailed literature scan is made for hybrid motors where various motor topologies are represented. Later, theory of permanent magnet machines are studied which were then used in the design part.

For the design part, two different stator structures are investigated: fractional slot and integer slot. A surface permanent magnet motor which is used as benchmark motor with fractional slot is analyzed following by the design of an internal permanent magnet (V-type) motor with the same size. After that aforementioned hybrid motor is designed and optimized.

For the integer slot part, by using the analytical equations, a surface permanent magnet motor is designed. By using the geometric quantities of the motor an internal permanent magnet motor is designed and optimized by varying magnet shape and position. After the design of IPM motor is completed, by implementing SPM and IPM magnets into the same rotor initial hybrid motor is formed. By appyling wide range optimisation, final hybrid motor design is obtained.

After the design phase is completed, integer slot motor is resized for prototyping. A prototype is built and tested in laboratory. Fine agreement between analysis and test results is obtained.

Investigated hybrid rotor topology for fractional and integer slot stators are compared with their consequent benchmark surface and internal permanent magnet motors. It is obtained that by using hybrid rotor structure with integer slot stator, it is possible to obtain better performance characteristics in terms of total harmonic distortion and torque ripple.

HİBRİT KALICI MIKNATISLI ROTOR TOPOLOJİSİNİN İNCELENMESİ

ÖZET

Çevresel kaygıların artmasından ötürü, teknoloji günümüzde materyallerin daha verimli kullanılmasına doğru bir gelişim içerisindedir. Daha az ya da aynı miktarda malzeme kullanımıyla daha yüksek performans elde etmek bu gelişimdeki en önemli arayış ve amaçtır. Bu bağlamda elektrik motorları, elektrik enerjisini mekanik harekete dönüştüren ve hemen her uygulamada kullanılan bir makina türü olduğundan, en popüler araştırma konularının başında gelmektedir. Elektrik enerjisinin büyük çoğunlukla elektrik makinaları aracılığıyla üretilmesi ve yine bu makinalar tarafından tüketilmesi elektrik makinalarının yapımında kullanılan malzemelerin verimli kullanımı çok önemli kılar. Elektrik makinalarının spesifik uygulamalara yönelik isterlerinin aynı ya da daha küçük ebatlarda elde edilmesi, sadece elektrik makinalarının yapımında kullanılan malzemelerin daha verimli kullanılmasına değil aynı zamanda, toplam sistem hacminin ve materyallerinin de daha efektif kullanımına olanak sağlayacaktır.

Geçtiğimiz yıllarda yüksek performanslı kalıcı mıknatısların ve nüve malzemelerinin de kullanımıyla, sürekli mıknatıslı elektrik motorları, daha önce klasik senkron, asenkron ve fırçalı doğru akım motorunun sıklıkla kullanıldığı uygulamalarda kendine geniş yer bulmuştur. Sürekli mıknatısların yüksek enerji yoğunluğundan yararlanan mıknatıslı elektrik motorları, diğer motorlara göre daha düşük hacim ve daha yüksek güç yoğunluğu sunmaktadır. Rüzgar türbinleri ve elektrikli araçların popüler hale gelmesi, hem doğru akım hem de alternatif akımla sürülen sürekli mıknatıslı elektrik motorların popülerliğini önemli derecede arttırmış ve bu alanda yapılan çalışmaların genişlemesine olanak sağlamıştır. Hem özel hem de genel uygulamalar için kendilerine geniş yer bulan sürekli mıknatıslı elektrik motorları, daha iyi performans verebilmeleri için, farklı stator ve rotor yapılarıyla beraber incelenmiş, geliştirilmiş ve farklı tipleri önerilmiştir. Gelişmekte olan teknolojiyle beraber bu araştırmalar daha da hızlanarak devam etmektedir.

Bu çalışmada, yakın geçmişte önerilmiş kalıcı mıknatlıslı bir hibrit rotor yapısı, motorun limitlerini ve performans kabiliyetlerini derinlemesine incelenmek amacıyla seçilmiştir. Literatür özeti kısmında elektrik motorlarının tarihiyle ilgili bilgi verilmiş ve daha sonra literatürdeki farklı motor yapıları incelenmiştir. Yapılan araştırmada hibrit yapıda olan motorlara ağırlık verilmiş ve incelenmesinin faydalı olacağı düşünülen bir model seçilmiştir.

Motor ön tasarım sürecinde herhangi bir yazılıma olan bağlımlılığı azaltmak adına, sürekli elektrik motorlarının teorisi incelenmiş ve ilgili denklemler sunulmuştur. Daha sonra, bu denklemler kullanılarak bir ön tasarım yapılmış ve piyasada kullanılan yazılımla yapılan tasarım sonuçlarıyla karşılaştırılmıştır.

Bahsedilen hibrit yapı, yüzeyden mıknatıslı ve gömülü mıknatıslı (V tipi) motorun mıknatıslarının tek bir rotorda birleştirilmiş halidir. Karmaşık olan bu yapının oluşturulabilmesi ve karşılaştırılabilmesi için aynı ebatlarda yüzeyden mıknatıslı ve gömülü mıknatıslı motor tasarımlarına ihtiyaç olduğu belirlenmiştir. Daha önce şirket bünyesinde tasarımı yapılan kesirli oluklu yüzeyden mıknatıslı bir motor üzerine çalışmalar yapılmış ve analiz sonuçları paylaşılmıştır. 27 oluk ve 8 kutup kombinasyonunda olan bu yapı için, stator boyutları ve mıknatıs hacmi sabit kalacak şekilde bir gömülü mıknatıslı (V tipi) motor tasarımı gerçekleştirilmiştir. Tasarım aracı olarak iki boyutlu sonlu elemanlar yöntemi kullanılmıştır. Daha sonra, iki motordaki mıknatıs sayısı yarıya indirilerek, gömülü tip mıknatıslar kuzey, yüzeyden mıknatıslar ise güney kutbu oluşturacak şekilde birleştirme yapılmış ve hibrit yapıya ilişkin ilk tasarım elde edilmiştir. Oluşturulan hibrit yapının mıknatıs şekilleri ve pozisyonları değiştirilerek, bunların motor performansı üzerindeki etkileri incelenmiştir. Geniş bir optimizasyon çalışmasıyla tek bir parametreye odaklanılıp nihai bir tasarım seçilmiş ve detaylı analizleri gerçekleştirilmiştir.

Daha geniş inceleme yapılabilmesi amacıyla, hibrit rotor yapısının, tam sayı oluklu bir kombinasyonda, aynı zamanda daha geniş bir optimizasyon yapılabilmesi adına daha büyük boyutlarda çalışılmasına karar verilmiştir. Bunun için önce, denklemler yardımıyla yüzeyden mıknatıslı bir motor tasarımı yapılmıştır. Sonuçlar piyasada kullanılan yazılım ile elde edilenlerle kıyaslanmış ve daha sonra detaylı tasarım için iki boyutlu sonlu elemanlar yazılımı kullanılmıştır. Optimizasyonu yapılan yüzeyden mıknatıslı motorun en düşük moment dalgalılığı noktası bulunarak nihai tasarım tamamlanmıştır. Gömülü tip bir mıknatıslı motor, iki boyutlu sonlu elamanlar yazılımı kullanılarak tasarlanmış ve yine en düşük moment dalgalılığı elde edilmek üzere optimizasyon çalışması gerçekleştirilmiştir. Gerekli analizlerin tamamlanmasının ardından, önceki bölümde olduğu gibi iki motora ait mıknatıslar birleştirilerek hibrit yapı oluşturulmuştur. Mıknatıs boyutları mümkün olan sınırlar çerçevesinde değiştirilip etkileri incelendikten sonra, en düşük moment dalgalılığı noktası bulunarak nihai tasarım yapılmıştır.

Tasarım kısmının tamamlanmasının ardından, tam sayı oluklu motorun prototip üretiminin yapılmasına karar verilmiştir. Üretim ve test kolaylığı bakımından şirket bünyesinde daha önceden üretilmiş bir motor boyutlarına yakın boyutlara ulaşılabilmesi için hibrit motor yeniden boyutlandırılmıştır. Rotor yapısının özel olmasından ötürü, mıknatısların düzgin bir biçimde yerleştirilebilmesi ve konumlarını koruyabilmesi adına, gömülü tip mıknatısların alt ve üst kısmındaki rotor olukları kaydırılarak mıknatısların kayması engellenecek şekilde tasarım revize edilmiştir. Aynı zamanda yüzeyden mıknatısların istenilen biçimde yerleştirilebilmesi için, rotora küçük çıkıntılar verilmiştir. Bu işlemler tasarımdan ayrı olarak, yine iki boyutlu sonlu elemanlar yazılımı kullanılarak analiz edilmiş ve motorun manyetik olarak etkilenmediği değişiklikler yapılmasına özen gösterilmiştir. Motor sac kesimi için gerekli teknik resimler hazırlanmış ve hassas lazer kesim makinasında kesilmiştir. Mıknatısların temini için de teknik resimler hazırlanmış ve mıknatıslar istenilen hassas boyutlara uygun olarak temin edilmiştir. Hassas lazer kesim makinası ile kesilen stator ve rotor laminasyonları, gerekli yerlerden kaynaklar yapılarak birleştirilmiştir. Stator ve rotor saclarının birleştirilmesinin ardından özel yapıştırıcı ile mıknatıslar yapıştırılmış ve sarım işlemi yapılmıştır. Prototip üretimin tamamlanmasının ardından motor laboratuvar ortamında test edilmiştir. Analiz ve test sonuçları arasında güzel bir örtüşme elde edilmiştir.

Yapılan çalışmalarda, kesirli oluklu motor yapısının mevcut olan motor boyutlarında referans olarak kullanılan yüzeyden mıknatıslı ve gömülü tip mıknatıslı motorlara göre daha düşük performans gösterdiği sonucuna varılmıştır. Öte yandan tam sayı oluklu hibrit motor moment dalgalılığı ve toplam harmonik bozulma parametreleri bakımından referans olarak kullanılan yüzeyden mıknatıslı ve gömülü tip mıknatıslı motorlara göre daha iyi performans göstermiştir.

1. INTRODUCTION

Electrical energy is the most frequently used type of energy and with the growing population and increasing demand, its generation and usage have great importance. In Figure 1.1, worldwide electricity generation is given, projecting from 2012 to 2040. As it is seen, production is expected to reach nearly 35 trillion kilowatt-hours in 2040, whereas the amount was near 20 trillion kilowatt-hours in 2012. Other than solar panels and some minor production ways of electricity, all electricity production is achieved by electric generators to produce electricity. Moreover, according to [1] and [2] 30-40% of all electricity produced is used by electric motors. This brings out that electrical energy heavily depends on rotating electring machines. By using proper smart systems and improving efficiency of electric motors and generators, 2 trillion watt-hours can be saved per year until 2030 [1]. In order to improve production and consumption quality of electrical energy, improvement in any parameter of electric machines proposes a better and sparing future.

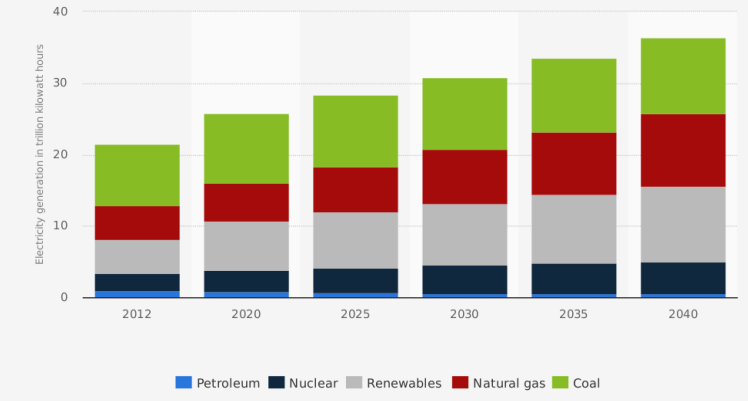

Figure 1.1: Worldwide energy production by sources from 2012 to 2040 [1].

Nowadays, electric motors can have very high efficiencies, up to 99% in some very high power applications [3], however motors with improved efficiencies for low power applications have high initial costs and this makes them unfavourable even though they will pay back for themselves in a short amount of time.

First rotating machines using electric current, permanent magnets or electromagnets with different kinds of mechanicsms were invented back in 1820's. Micheal Faraday made experiments in 1821, which wire moves circularly on a plate with a magnet in center. In 1822, Peter Barlow invented a spinning wheel, which is a simple unipolar machine. William Sturgeon became the first person to use concept of electromagnet, where current is passed through a wire stranded around a horse-shoe shapede iron core in 1825-1826. In 1827-1828, Jedlik used electromagnets and a commutator to build the first rotary machine. In 1831, Micheal Faraday and Joseph Henry, independent from each other, found electromagnetic induction and Henry built a magnetic rocker. Savatore del Negro, thought to be inspired by Joseph Henry's work, built a lifting device, developing approximately 30mW power in 1832. Again in 1832, an anonymous letter, describing a rotating electrical machine, reached Micheal Faraday and he published it with the name "First description of a rotating electrical machine by P.M". Until 1834 there are more examples like these, but in that year Moritz Hermann Jacobii builds an electric motor which resembles motors similar to today's, producing 15 W of power. Later Jacobi moves to St. Petersburg in 1838, where he improves his motor by supports of Russian Tsarand and makes an electrically powered boat. Robert Davidson, who was also developing electric motors, had buildt the first electrically powered car in 1839 which created 0.74 kW of power. Werner Siemens, in 1856, builds a generator with double T armature windings and places them into slots. This is the first time slots were used in the history and until now, majority of electric motors are built with slots. In 1861, James Clerk Maxwell works for all theoretical information until that time and summarizes them in 20 equations, later in 1882 by the work of Oliver Heaviside, these equations are further decreased to 4 equations with 4 variables and takes the current form which is known as Maxwell's Equations. Between the years 1885-1893 multi-phase systems and induction motors are studied by Nicola Tesla, Galileo Ferraris, Charles Schenk Bradley, Micheal Dolivo-Dobrowolsky and Jonas Wenström [4][5].

After the invention of electromagnet in 1825 by Sturgeon, permanent magnets used in the preliminary motors lost interest because at that time it was more advantegous to use electromagnets. In 1882, John Urquhart said use of electromagnets instead of permanent magnets leads to lower size and cost meanwhile increasing power [6]. Until the invention of induction motor, electromagnetic DC motors were the only motor used

in industry. With the AC induction motor's invention a new and a simpler motor has born. Although the induction motor was simpler than DC motor, difficulties in operation and control did not provide the AC motor superiority [7].

Until the invention of new permanent magnet in 1930s, AlNiCo magnets which are formed by addition of elements Al,Ni,Co,Mn,W, permanent magnets were limited to magnetite also known as loadstone. These magnets had very low power and needed to be used in high amounts to create a useful magnetic field which decreased the interest in making motors with permanent magnets. But the gamechanger became AlNiCo magnets, which had 100 times the power of loadstone [8]. Later in 1950's ferrites, also known as ceramic permanent magnets are discovered and they are still used in electric motors. With the invention of SmCo and NdFeB magnets in 1960 and 1980s, permanent magnet DC motors took place in markets in 1970s. Development of drive circuits remove the necessity of physical commutation which supported the usage of permanent magnets in brushless structure [7].

High power permanent magnets are widely used in electric motors since they are invented. At the present time, permanent magnet electric motors can be used in all applications. The usage of electric motors including permanent magnets are quite advantegous from low to high power because of their smaller size, higher efficiency and higher power factor.

Nowadays, research topics of permanent magnet motors include reducing torque ripple, reducing total harmonic distortion of back EMF, increasing average torque, reducing cogging torque, decreasing losses, increasing maximum speed, increasing the filling area of stator slots as well as developing new techniques and improving materials used in a motor.

1.1 Purpose of Thesis

In this thesis, hybrid rotor topology containing both surface and internal permanent magnets are investigated. In order to design the hybrid rotor, first a surface permanent magnet then an internal permanent magnet motor is designed and they are combined. Optimizations are done by changing magnet shapes and positions and keeping the magnet volume constant in order to get best design with minimum torque ripple and total harmonic distortion. Hybrid motor is designed for a 27 slot 8 pole fractional slot

and a 48 slot 8 pole integer slot combinations to clearly see the effects of hybrid topology. Flux2D is used as a finite element analysis software for analysis. Comparison between surface, internal and hybrid motors are presented. Finally a prototype motor is produced and tested.

1.2 Literature Review

This section provides brief technical information for research topic. Properties and benefits of using permanent magnets in electric motors, types of electric motors and lastly hybrid motor are technically summarized by previous studies.

1.2.1 Permanent magnets

Permanent magnets have been used early in the history for various applications including systems providing rotation. Today, there are many types and classes of permanent magnets with different properties for numerous applications. Production technique of these magnets as well as internal structure plays important role to determine magnetic and physical properties of permanent magnets.

1.2.1.1 Properties of permanent magnets

Permanent magnets are very important materials for electric motors because of their high energy. Ferrite, SmCo (Samarium-Cobalt), AlNiCo (Aluminium-Nickel-Cobalt) and NdFeB (Neodymium-Iron-Boron) are the most common types of magnets used in the industry. Ferrite magnets are the mostly used magnets because of their low price whereas NdFeB is the strongest magnet with high price. Magnets can be produced either by bonding or sintering. Bonding process is done by shaping magnet powder and some other holder materials by pressing or die molding. Bonded magnets do not have high power because of their production technique whereas they can be freely shaped. Sintered magnets are produced by complicated heating process after they are shaped. Bonded magnets can be shaped to have more complex geometries and they are easy to manufacture on the other hand sintered magnets have more plain shapes and they are brittle. Figure 1.2 shows the demagnetization curves for NdFeB, SmCo, AlNiCo and ferrite type magnets. Vertical axis shows remanence and horizontal axis shows coercivity of the magnets. Coercivity of a magnet refers to the maximum magnetic field intensity which a magnet can resist before demagnetization.

Remanence of a magnet is the flux density which remained in the magnet after magnetization process. Hc [kA/m] and Br [T] together gives the maximum energy product of a magnet.

It is also important to know the effect of temperature on magnetic properties. Magnetic materials shows different magnetic properties at different temperatures. Permanent magnets lose some of its magnetic properties at increasing temperature. Typically remanence and coercivity decreases with increasing temperature. Magnetization curve of N30UH class Neodymium magnet is shown Figure 1.3 for various temperatures [10].

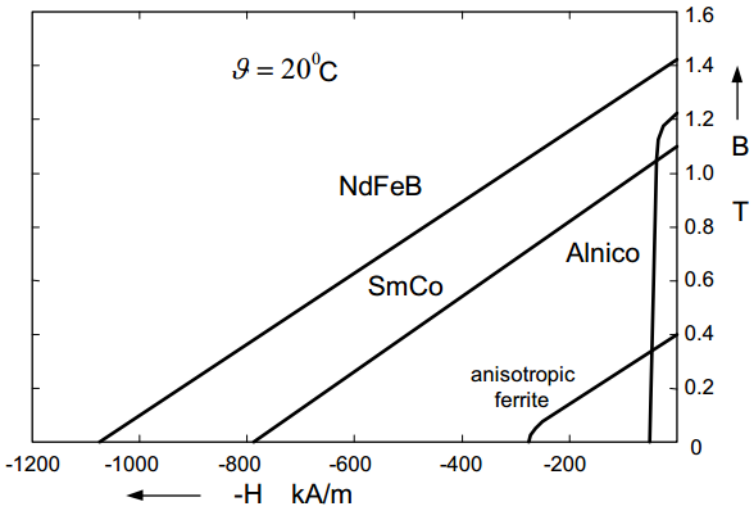

Figure 1.2: Magnetization curves of different permanent magnets [10].

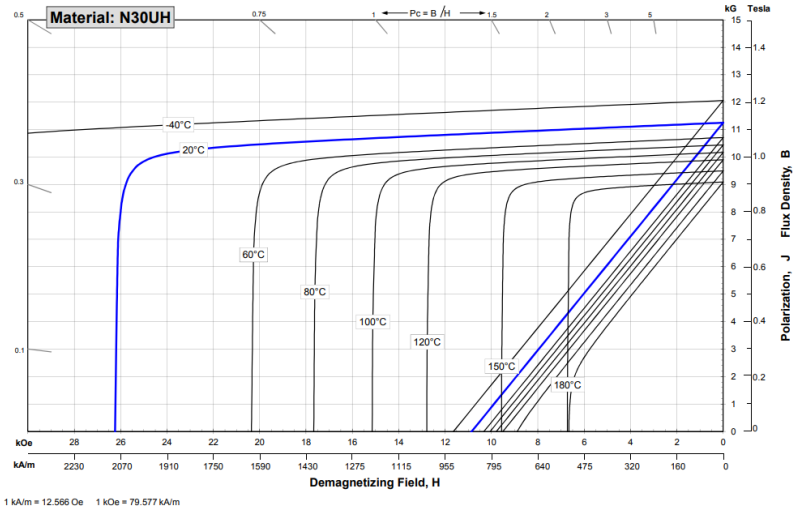

Figure 1.3: Magnetization curves of N30UH class type Neodymium magnet for different temperatures [10].

According to the magnet type this deterioration changes. In (1.1) and (1.2) equations for determining the remanence and coercivity are given [9]. It is important to know that, a_B and a_H are temperature coefficients for reversible changes. Values for a_B and a_H are -0.12 and -0.465 respectively for N30UH class Neodymium magnet from Arnold Magnetics.

$$Br = B_{r-\vartheta i}[1 + \frac{a_B}{100}(\vartheta_f - \vartheta_i)] \tag{1.1}$$

$$Hc = H_{c-\vartheta i}[1 + \frac{a_H}{100}(\vartheta_f - \vartheta_i)] \tag{1.2}$$

Another important parameter for permanent magnets is the Curie temperature. Curie temperature is the critical temperature at which ferromagnetic materials lose their magnetism and start to behave like a paramagnetic material. When Curie temperature is exceeded for a permanent magnet material, magnet does not produce any magnetic field even after the temperature is decreased. Small areas in the material have magnetic fields but since they are randomly directed, no usefull magnetic field occurs. (These fields are called Weiss fields.) The material has to go under a similar magnetization process which it first gained it magnetic properties.

1.2.1.2 Usage of permanent magnets

Permanent magnets are widely used in many applications such as hand tools, jewelry, superconductivity applications and electric motors with high power density. The reason for employing permanent magnets in electric motors is to create a constant magnetic field. Also, when permanent magnets are not used in electric motors, rotating part of the motor has to include an electromagnet which needs brush and collector system. This system leads to many diffuculties in production and maintenance and reduces the lifespan of electric motors. In Figure 1.4 the same magnetic field magnitude is reached by passing a current of 13A through a 220 turn coil and by a NdFeB magnet with 3mm thickness and 20mm length. The corresponding cross sectional areas are 300 mm^2 and 60 mm^2. The coil has 5 times the area of the magnet with resistive losses of approximately 50W [11]. It is depicted that in order to produce magnetic field, a permanent magnet has great advantage in terms of area and losses.

This brings out that, motors which do not contain permanent magnets will chronically have resistive losses while producing a magnetic field plus tendency to have larger volume or lower power.

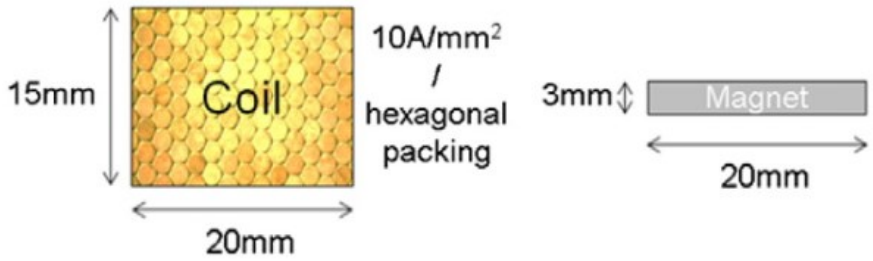

Figure 1.4: Comparison of a NdFeB PM with a current carrying coil in order to generate the same magnetic field [11].

1.2.2 Types of electric motors

There are many different types of electric motors, where a number of them are used only in special applications. Electric motors can be classified as AC or DC according to the waveform of current supplied. DC motor family has two main subtypes which are brushed and brushless. AC motor family has also have two types which are asynchronous (induction) or synchronous.

Brushed DC motors are the oldest type of motors historically. They have brushes in order to transfer current to rotating part where the polarity of current is changed by the help of the brushes. Series excited, parallel excited (shunt), series-parallel excited (compound) and permanent magnet motors are the types of brushed DC motors. Permanent magnet brushed DC motors have permanent magnets fixed to the housing and they have windings in the rotating part. Other DC motor types' fixed and rotating parts include windings which are either in series, parallel, both or seperately excited. In series connected DC motors, field and armature windings are connected in series. Although high starting torque is obtained with this type, motor speed varies greatly under no-load and on-load conditions. Parallel connected DC motors and seperately excited DC motors offer good torque-speed characteristics with enhanced ability to operate in variable speed drives. The compund DC motor is a combination of series and parallel connected. Although good starting torque and speed characteristics can be obtained, contol of the motor is difficult.

AC motor types are named as asynchonous and synchronous according to their rotation. A synchronous motor rotates synchronously with the rotating magnetic field created by three phase currents supplied to the armature of the machine whereas an asynchronous motor (induction motor) does not. An induction motor works on the principle of induction and induction only occurs when there is a relative speed difference between rotating part of the machine and the rotating field of the machine created in fixed part. Induction motors are further classified into squirrel-cage and wound rotor motors. Squirrel-cage rotor has a number of conducting bars (mostly aluminum and copper) which are shorted at the ends. This type of rotor does not have any connection to outside. Wound-rotor has three phase coils wound on the rotor connected to three slip-rings which are connected to seperate terminals. Figure 1.5 shows the squirrel-cage and wound rotor induction machines.

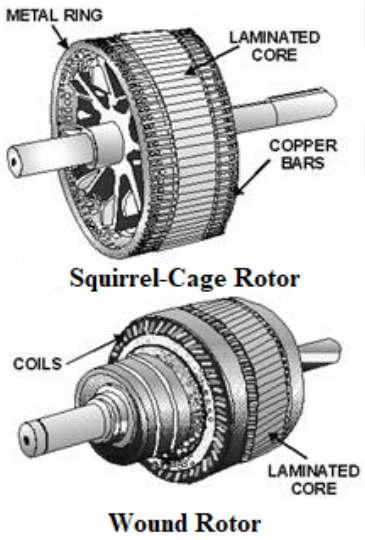

Figure 1.5: Rotors belonging to squirrel-cage and wound rotor induction machines.

Synchronous machines can be classified according to their field excitations. Salient-pole and cylindrical-rotor synchronous machines are the two types of synchronous machines having DC windings in their rotor to create constant magnetic poles. Figure 1.6 shows the two rotor constructions of synchronous machines. In both rotors, windings are excited via slip rings previously mentioned in wound-rotor induction motors. Electromagnetic poles of a cylindrical rotor are distributed on the periphery of the rotor where the air gap between the stator and rotor is uniform. In the case of a

salient-pole rotor, electromagnetic poles are projected towards the stator where the air gap is non-uniform.

Permanent magnet synchronous machines are quite similar to the cylindrical-rotor and salient-pole synchronous machines except the excitation to create poles are done by using permanent magnets. By using permanent magnets as poles, no contact regions like slip-rings or brushes as in the case of DC motors are needed, also winding losses are eliminated. Brushless DC motors and permanent magnet AC motors are in fact the same motors in construction perspective. BLDC motor is supplied a switching direct current determined by signals coming from hall sensors. PMSM is given alternating current and it is controlled by signals coming from either resolver or encoder.

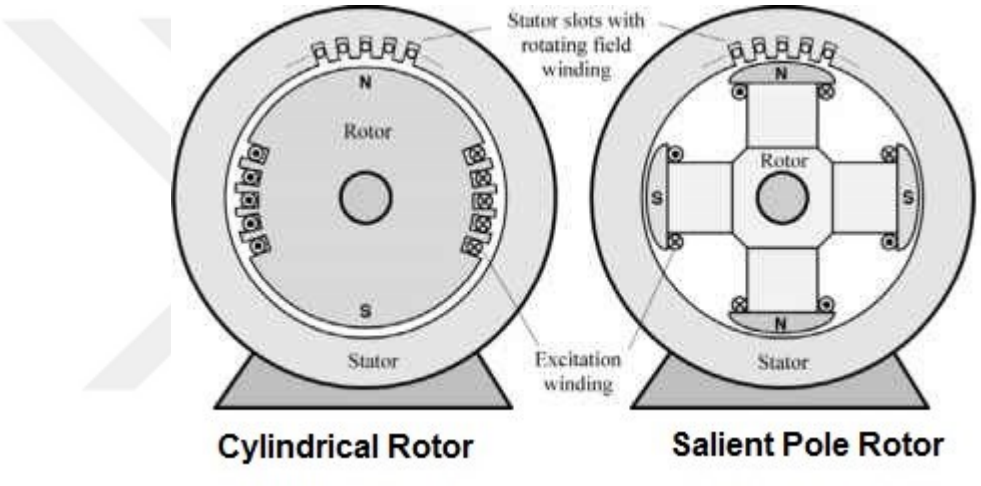

Figure 1.6: Cylindrical and salient-pole rotor types of synchronous machines.

Another type of synchronous motors is reluctance motor which is shown in Figure 1.7.

Figure 1.7: Rotor of a synchronous reluctance motor.

Synchronous reluctance motors do not have any type of excitation in rotor, their working principle is based on the alingment of magnetic materials in the presence of a magnetic field. Rotor is shaped so that at a position reluctance with respect to the stator changes, and rotor moves towards to a lower reluctance position.

1.2.2.1 Types of brushless permanent magnet motors

Brushless permanent magnet motors are either DC or AC, according to their type of excitation as well as BEMF waveform. Although there are differences in control, their constructions are quite the same. They can be further classified into surface permanent magnet and interior (buried) permanent magnet motors. Different rotor types of surface mounted permanent magnet motors are shown in Figure 1.8.

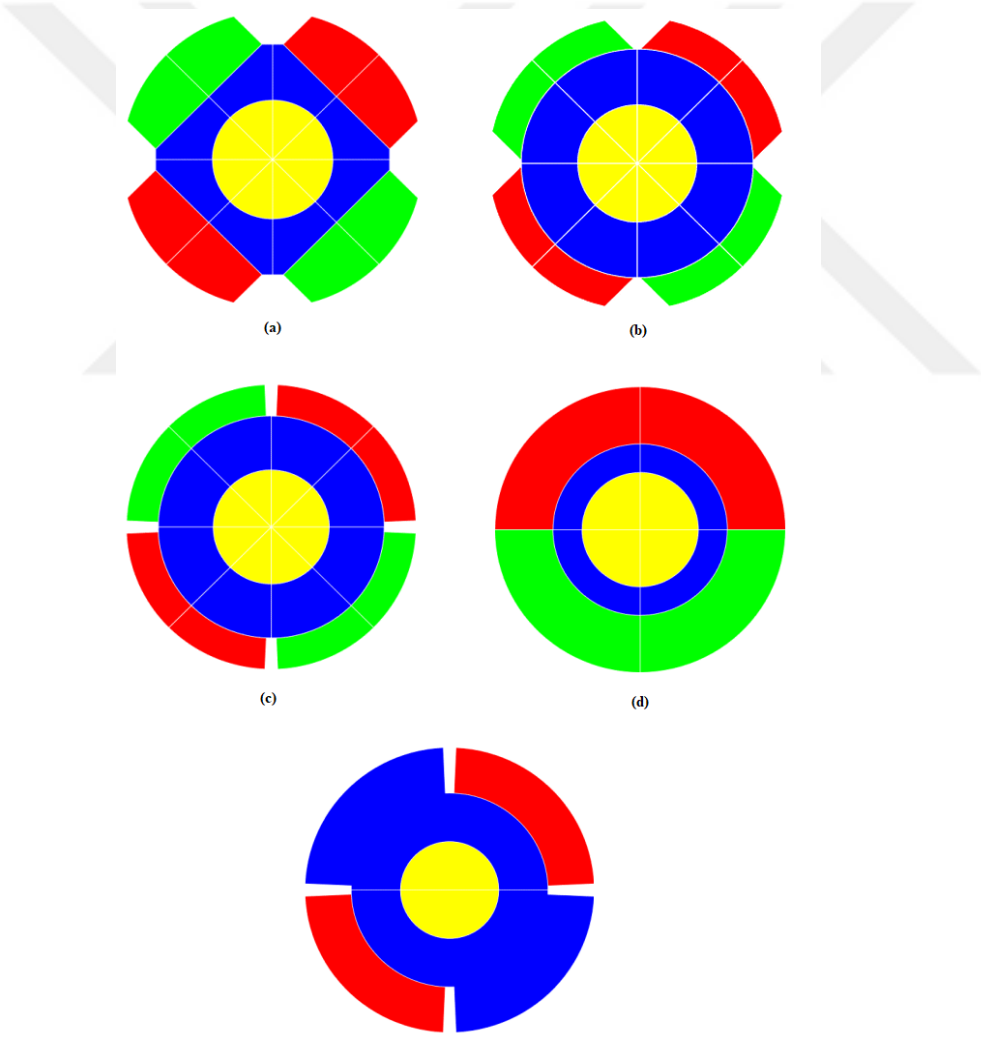

Figure 1.8: Different rotor types of surface permanent magnet motors: (a) breadloaf type, (b) surface parallel type, (c) surface radius type, (d) ring type, (e) consequent pole type [12].

Type (a), (b) and (c) are the most common types of surface permanent magnet motors. Type (d) is generally used in special motors like small outer rotor motors and slotless motors. Type (e) is a special configuration where there are two magnets having the same polarities and two projections of rotor electrical steel. Type (e) is used to create a saliency and reluctance difference. Type (a) is generally preferred to be used for PMSMs as the magnet builds up in the middle and this has tendencay to create a sinusoidal BEMF waveform. Type (b) and (c) is also used for PMSMs despite it is generally used for BLDC motors as it can decrease torque ripple.

Figure 1.9 shows different types of IPM motors. Among them, (b) V-type, (c) PM assisted synchronous reluctance type, (d) V-type (2) and (f) spoke type are top research topics in the literature and also commonly used in applications.

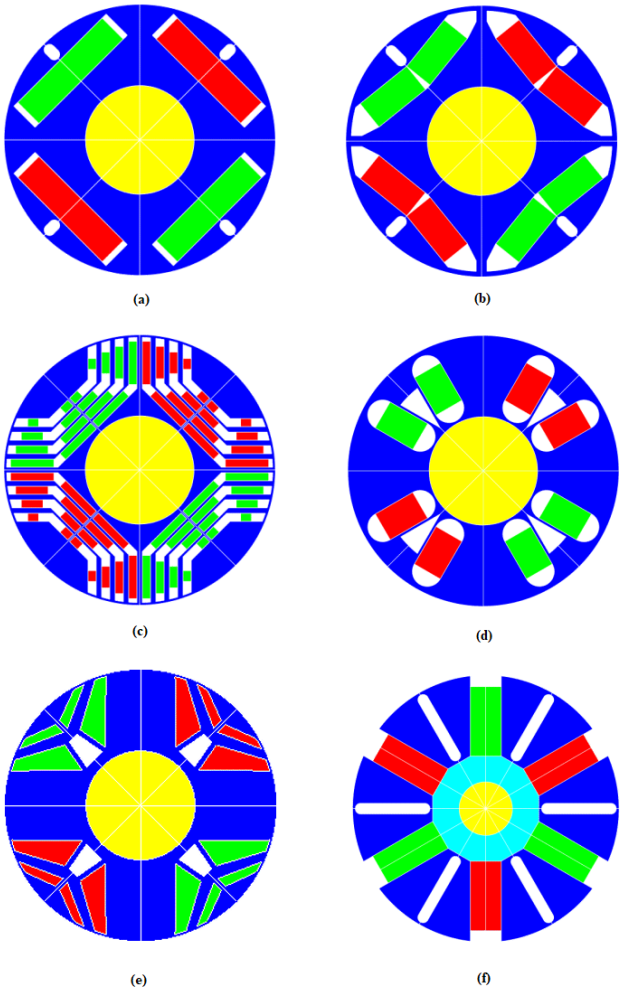

Figure 1.9: Different types of IPM motors: (a) buried, (b) V-type, (c) PM assisted synchronous reluctance, (d) V-type-2, (e) double V-type, (f) spoke type [12].

SPM motors are highly in demand in many areas because of their simple design and construction. They have high power density and robust rotor. As drawbacks, magnets have risk of demagnetization and dislocation at high speeds. Generally special coatings are applied to the SPMs in order to reduce the risk of demagnetization and sleeves are used for dislocation issues. Another weakness of SPM motors is that they lack saliency. Since magnets are placed on the surface of the rotor and they have permeability nearly equal to the air, there is no difference in reluctance and this causes very low, ideally no saliency. Equation (1.3) is the well-known permanent magnet synchronous machine torque equation where L_d is the d-axis inductance, L_q is the q-axis inductance, λ_{PM} is the permanent magnet flux linkage, i_d is the d-axis current, i_q is the q-axis current is the number of pole pairs. The first term in the equation (1.3) is the permanent magnet torque produced by permanent magnets and the second term is reluctance torque created by the difference of reluctance in direct and quadrature axis inductances.

$$T = \frac{3}{2} p(\lambda_{PM} i_q + (L_d - L_q) i_d i_q) \tag{1.3}$$

In an ideal SPM motor d-axis and q-axis inductances are equal but in practise inductances are very close to each other. In both scenarios second term in equation (1.3) becomes zero, eliminating the contribution of reluctance torque to the total torque. Saliency ratio is defined as L_q / L_d in [13] , and different types of motors have different saliency ratios. In Figure 1.10 and Figure 1.11 saliencies of different electric motors and consequent power-speed curves are given respectively. These concepts are first introduced in [13] and referred as IPM parameter plane. In Figure 1.10 saliency ratios of different types of motors are given according to the normalies magnet flux linkage and in Figure 1.11 power versus speed curves are given according to same parameters. In [13] it is mentioned that power versus speed characteristics of an IPM machine can be evaluated according to these two parameters, saliency ratio and ratio of magnet flux linkage to all flux linkage (normalised magnet flux linkage) due to its hybrid utilization. In Figure 1.11 it is seen that SPM machines have nearly 1 normalized magnet flux linkage meaning that torque is produced by permanent magnet flux. Towards the upper left part of the graph magnet flux decreases as the usage of permanent magnets decreases and saliency increases. It is also underlined that usage

of permanent magnets does not change saliency ratio but increases magnet flux linkage leading to higher power density, higher inverter utilization and higher power factor. Machines having high saliency also have higher speed ranges [13].

Other than being a very good candidate for variable speed applications, IPM type motors are more suitable for high speed applications when compared to SPM type motors. Magnets being inside the rotor removes the risk of dislocation and magnets are also naturally protected for demagnetization.

In some high speed applications where maximum speed is also higher than the rated speed IPM type motors are used. For example, electric motor of Toyota Prius is a V-type IPM motor and electric motor of BMW i3 is a double-layered IPM motor [14][26].

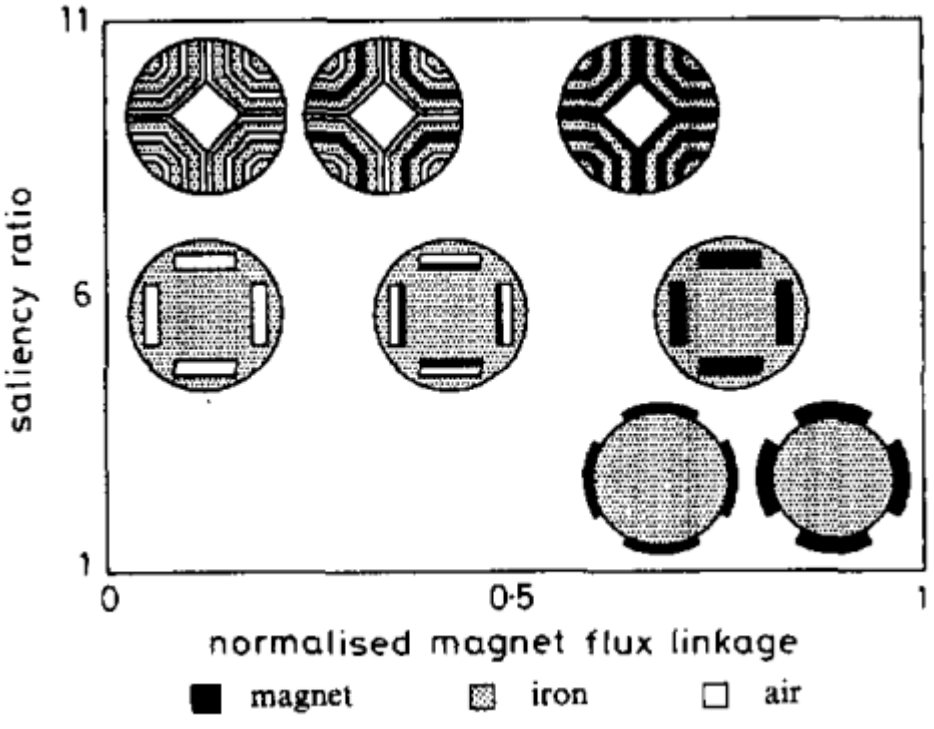

Figure 1.10: Saliency ratio versus normalised magnet flux linkage of different types of motors [13].

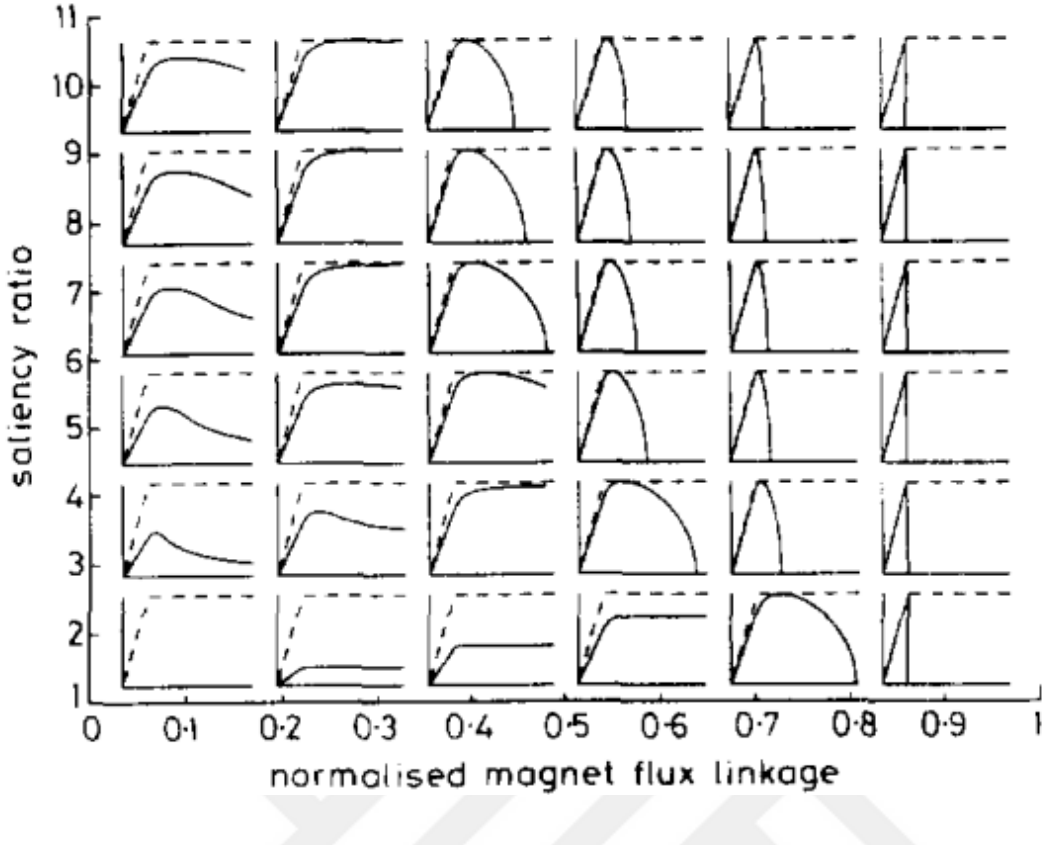

Figure 1.11: Various power versus speed graphs according to saliency ratio and normalised magnet flux linkages [13].

1.2.3 Hybrid Motors

Term hybrid comes from mixing two or more different types to get a new type of product. In electric motors this can be done by creating a rotor or stator which is composed of generally two different types of motor having different magnetic or electric properties. For example in [13], Miller and Soong described all internal permanent magnet motors as hybrid motors because of their PM and reluctance characteristics while analyzing field weakening capability.

One of the first papers investigating the hybrid motors is [16], where permanent magnet motors with saliency as well as having self-starting capability is investigated. Binns et al. objected to investigate PM synchronous motors having cage bars to provide self-starting, and to do so, synchronous and asynchronous performances are evaluated individually. Some history of permanent magnet motors are mentioned, such as the Merrill's motor and other research about usage of flux barriers and configuration of cage bars are summarized. Relevant designs are shown in Figure 1.12. Later in [17],

authors further studied on the designs and investigated effect of pole arc, pole-shoe width, magnet depth, width of the iron bridge and flux barrier width on pull-out torque.

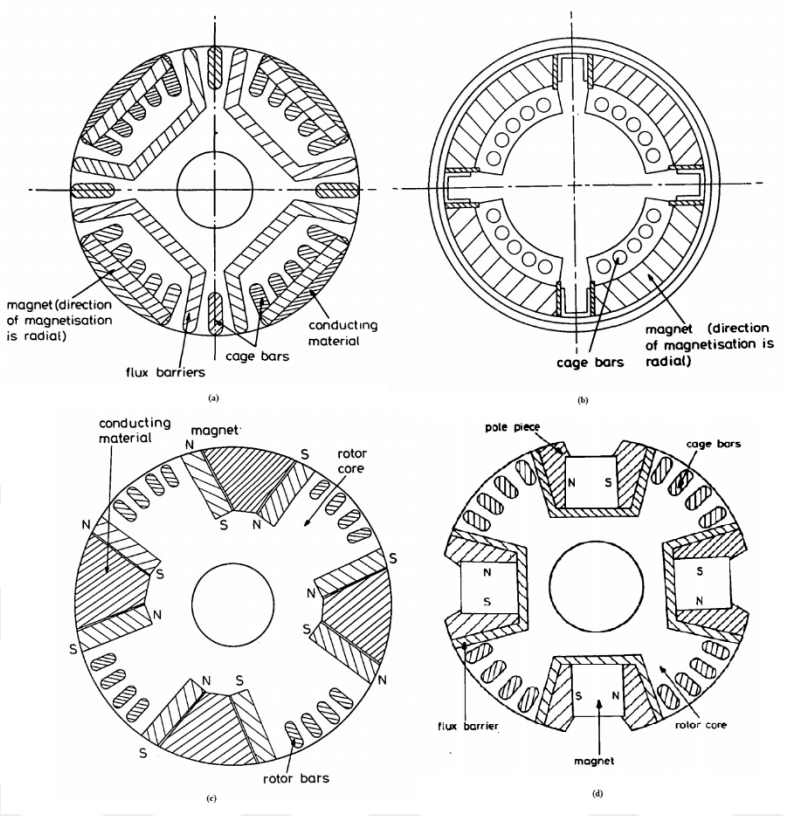

Figure 1.12: Different permanent magnet hybrid rotors with cage bars in rotor: (a) Honsinger's propesed with flux barriers, (b) Siemens's permanent magnet motor with cage bars being under magnets, (c) proposed motor with 2 magnets per pole, (d) proposed motor 1 magnet per pole with flux barriers [16].

A new rotor geometry for line-start PM synchronous motor is proposed by Chaudhari et al. and FEA analysis results are given in [18]. The structure is shown in Figure 1.13. Effect of magnet width and incline angle is studied along with magnet material in order to obtain high air gap flux density as well as good starting characteristics.

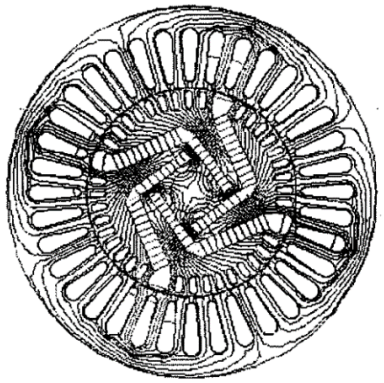

Figure 1.13: Proposed line-start PM synchronous motor no load flux density [18].

Petrov et al. investigated a line-start PM reluctance machine with ferrite magnets [19]. It is aimed to obtian a motor topology which has capability of self starting to be used in industrial pump or ventilation systems and which has higher efficiency than induction machines. Proposed machine is designed by optimizing the number and thickness of air barriers and thickness of ferrite magnets. Furthermore, possible risk of demagnetization is also taken into design consideration. Thus PM width, rotor cage shape and barriers are carefully designed and analysed to meet the objectives.

A synchronous generator is designed with a hybrid rotor having air barriers and cages [20]. Studied structure is given in Figure 1.14. The aim of the study is to design a generator which is brushless so that it can be used in explosive and inflammable place. To do so, two different windings are placed in stator having different pole numbers, one to generate torque by rotating magnetic field and the other to provide excitation by a constant magnetic field. Designed generator is manfucatured and comparisons are provided.

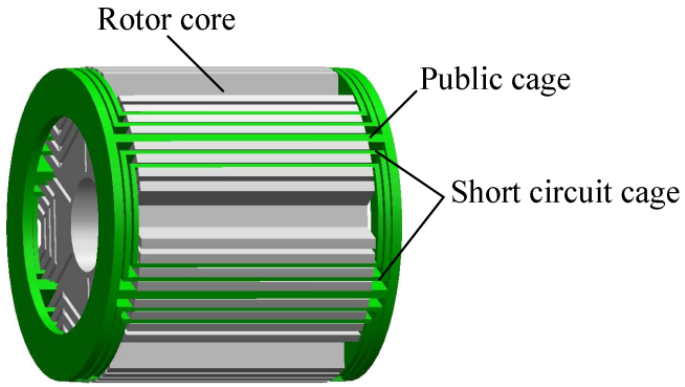

Figure 1.14: Rotor of the brushless, electrically-excited reluctance type synchronous generator [20].

A new five-phase motor is proposed for electric vehicles where it is aimed to obtain a fault-tolerant motor by Zhang et al. in [21]. In order to achieve the objectives, a single layer concentrated winding is adopted with unequal tooth widths as well as an asymmetrical air gap. Moreover, rotor excitation is applied with two windings, one for field winding and other for compressing the high harmonic component caused by stator winding. Windings are placed to upper part of V-shaped magnets.

Zhu et al. proposed a spoke type hybrid PM motor for electric vehicles where both neodymium and ferrite PMs are used [22]. The aim is to achieve both cost-effective and high performance motor that can be used for electric traction motors. To do so, volume of neodymium magnets are minimized and ferrite magnets are maximized. The structure of proposed hybrid spoke motor is shown in Figure 1.15 with a conventional type spoke motor. Relevant analysis are done, computing: torque, cogging torque, BEMF and inductances in order to compare the performances of two motors. It is shown that torque and BEMF amplitude of the proposed motor is slightly lower than the conventional one, whereas cogging torque is a little lower. Also higher saliency is achieved with the proposed hybrid motor.

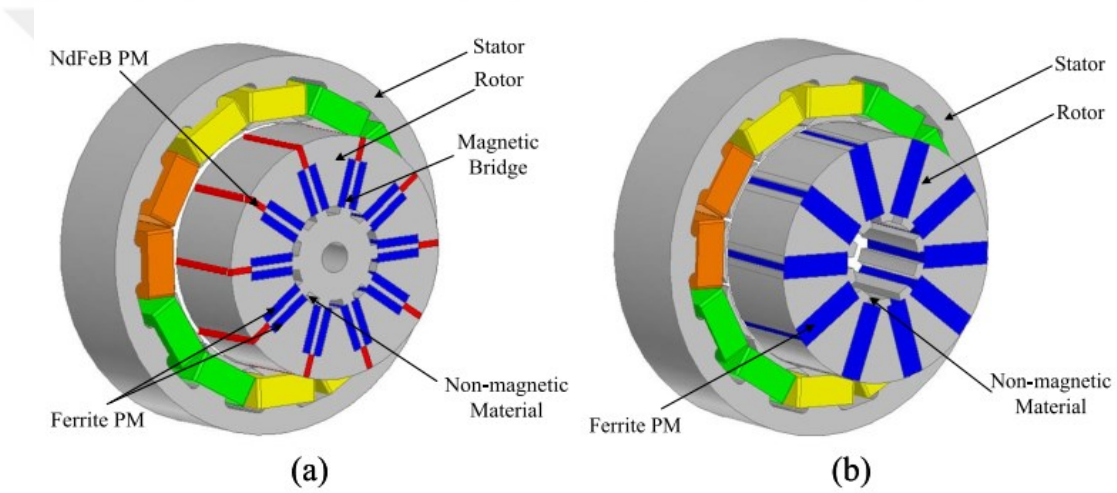

Figure 1.15: Proposed hybrid and conventional type spoke motors: (a) proposed motor, (b) conventional motor [22].

A novel structure is designed to fully benefit from reluctance and PM torque in [23]. The structure consists of two different rotors, one consists of SPMs and other is a air-barriered reluctance motor rotor. In order to design the motor, a PM- assisted synchronous reluctance motor is decomposed into two equal length rotors, extracting the magnets and leaving the remaining part as a synchronous reluctance rotor. The first part which will have PMs is converted into an SPM rotor and the other part is leaved as it is. After that in order to benefit from reluctance and PM torque, their axes are made to be same by shifting the reluctance rotor by 45 degrees. Designed motor is compared with Toyota Prius 2010 electric motor and it is shown that the novel designed motor has better characteristics in terms of torque producing capability in the

whole speed range with low lower torque ripple and efficiency. The proposed structure is shown in Figure 1.16.

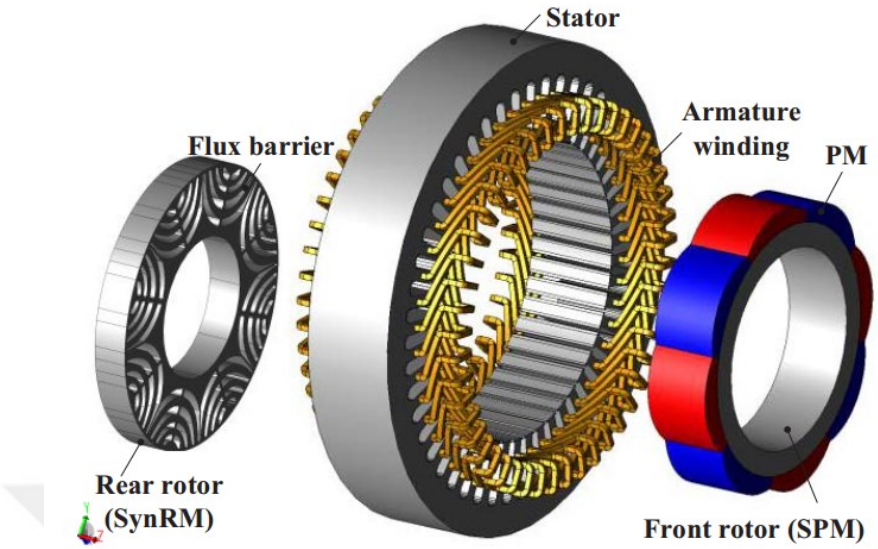

Figure 1.16: Novel motor design having two rotors [23].

Liu et al proposed a hybrid rotor configuration consisting of both SPMs and IPMs. It is aimed to enhance the torque characteristics in terms of average torque and torque ripple [24]. In order to reach the objectives, SPMs are used as inset and IPMs are included in the structure. Surface magnets are shifted in order to get air barriers for better characteristics by introducing further asymmetry. Shifting of inset SPMs ar optimized for higher average torque and lower torque ripple. Comparisons are made between SPM, IPM and hybrid motor and through analysis and test verification results are given. It is seen that by employing the structure in Figure 1.17, authors managed to achieve their objectives. Later, hybrid structure is verified analytically by reluctance network model [25].

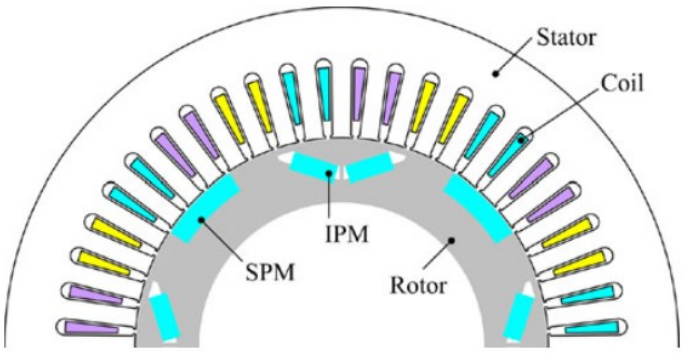

Figure 1.17: Proposed hybrid rotor with both SPMs and IPMs [24].

2. THEORY OF PERMANENT MAGNET SYNCHRONOUS MACHINES

Synchronous machines operate at a speed which is the imaginary speed of the rotating magnetic field created by stator windings for a conventional inner rotor and radial flux motor configuration. Magnetic field of the rotor locks with the rotating magnetic field of the stator in which synchronism is achieved. There are many types of synchronous machines either with permanent magnets or not as mentioned earlier. In this section some important relationships will be discussed and later they will be applied for a machine design.

2.1 Synchronous Speed

Synchronous speed is the speed at which a synchronous machine rotates and it is given by equation (2.1).

$$n_s = \frac{60f}{p} \tag{2.1}$$

2.2 Air Gap Flux Density (Specific Magnetic Loading)

Air gap flux density is one of the key parameters in any electric machine. In one extend it shows how well field excitation, either by electromagnets or permanent magnets, is formed. Generally for high power density machines its value is between 0.7 and 1 Tesla.

$$B_{mg1} = \frac{2}{\pi}\int_{-0.5a_i\pi}^{0.5a_i\pi}(B_{mg}\cos a)da = \frac{4}{\pi}B_{mg}\sin(\frac{a_i\pi}{2}) \tag{2.2}$$

First harmonic of the air gap flux density , is given by equation (2.2) as in [9], where a_i is given by equation (2.3).

$$a_i = \frac{B_{avg}}{B_{mg}} \tag{2.3}$$

Here it is important to note that a_i is a unique value for different motor configurations. For example when the air gap flux density is sinusoidal its value is $\frac{2}{\pi}$ in case of a slotless motor where sinusoidal air gap flux can be achieved.

2.3 Back Electromotive Force

BEMF is the voltage induced at the terminals when the motor is rotated. BEMF waveform gives direct insight about total harmonic distortion and indirect insight about torque and torque characteristic. For instance if BEMF waveform of machine is high in harmonics then high torque ripple and/or cogging torque can be expected.

$$E = \pi\sqrt{2} f N k_{w1} \phi_f \tag{2.4}$$

Equation (2.4) gives the root mean square value of the phase voltage induced, where equation (2.5) gives first harmonic of air gap flux.

$$\phi_{f1} = \frac{2}{\pi} \tau L_i B_{mg1} \tag{2.5}$$

Here an important parameter is the first harmonic of winding factor . Winding factor is expressed as equation (2.6), product of distribution, pitch and skew factor if skewing is applied either on stator or rotor.

$$k_{w1} = k_{d1} k_{p1} k_s \tag{2.6}$$

Distribution factor is the ratio of the induced voltage in a distributed winding and concentrated winding and given by equation (2.7).

$$k_{d1} = \frac{\sin(Q\gamma/2)}{Q\sin(\gamma/2)} \tag{2.7}$$

Pitch factor is used when coil sides forming a coil are not placed radians apart from each other. Generally short pitching is applied in order to reduce specific harmonics such as the 5th harmonic. Equation (2.8) is the expression for pitching factor.

$$k_{p1} = \sin(\frac{\pi}{2}\frac{w_s}{Qm}) \tag{2.8}$$

$$\gamma = \frac{\pi}{mQ} \tag{2.9}$$

There are mainly two winding types according to the value of . Number of slots per pole per phase simply determines if the winding is a fractional slot or integer slot type.

Skewing factor is given by equation (2.10). Generally stator or rotor of a machine is optimally skewed for one slot pitch in order to eliminate or decrease cogging torque, increasing BEMF and output torque quality, in integer slot machines [26]. Skewing is generally not applied to fractional slot machines for torque ripple reduction and increasing BEMF harmonic quality as usage of fractional slots do this at the first place [26] . In [27], [28] and [29] skewing is deeply investigated. It is shown that optimal skew angle may not be one slot angle for different slot/pole combinations, also unconventional skewing is investigated.

Another important point is that, it is not always appropriate to account for skewing by just using skew factor because of 3D effects, especially in case of skewing magnets. Since it is not cost effective to apply skewing to one piece of magnet, axial length is divided into segments and skew is applied afterwards. In some cases where magnet shape is unusual, 3D leakage flux may affect the total flux, therefore detailed 3D analysis has to be done.

$$k_s = \frac{\sin(\frac{z\pi p}{2Q})}{\frac{z\pi p}{2Q}} \tag{2.10}$$

2.4 Specific Electric Loading and Current Density

Specific electric loading is defined as peak current flowing through stator inner circumference. Current density is the curret flowing through conductor area [9].

$$A_m = \frac{m2NI_p}{\pi D_{si}} = \frac{m\sqrt{2}NJ_{RMS}s_a}{p\tau} \tag{2.11}$$

Common values of magnetic and specific electric loadings are given in Table 2.1 and Table 2.2 where standart values of regional flux density values are given for different electric machines. Since flux density in electrical steel parts are restricted according to the steel property, these values may vary according to the material, in order to keep core losses in certain levels. Also in high flux densities, permeability of electrical steel decreases. In a complete saturation, permeability of steel can decrease down to air's which tremendously increases reluctance affecting motor performance.

Table 2.1: Magnetic flux density values for various parts of machine for different electric machine [30].

Flux Density [T]				
	Asynchronous machines	Salien-pole synchronous machines	Nonsalient-pole synchronous machines	DC machines
Air gap	0.7-0.9	0.85-1.05	0.8-1.05	0.6-1.1
Stator yoke	1.4-1.7	1-1.5	1.1-1.5	1.1-1.5
Tooth	1.4-2.1	1.6-2	1.5-2	1.6-2
Rotor yoke	1-1.6	1-1.5	1.3-1.6	1-1.5
Pole core	-	1.3-1.8	1.1-1.7	1.2-1.7
Commutating poles	-	-	-	1.3

Standart electric loading and current density values are shown in Table 2.2. It is seen that current density values can be increased with a more effective cooling technique but in standart air cooling 4-6.7 A/mm2 are generally preferred to prevent excess heating. Current density is a measure of motor temperature, therefore high values are generally not preferred or used in short duty times. Overheated motor can harm insulations leading to decreased life time and demagnetization of magnets. In special applications like traction, in order to decrease volume liquid cooling is used to overwhelm the heating effect of high current density. Also in some applications superconducting windings are used with exceptionally high current densities. In a

specific example of [31], a synchronous machine with superconducting field windings is used with 168 A/mm2 current density, in order to increase power and decrease volume.

Table 2.2: Specific electric loading and current density for different electric machines [30].

		Salient-pole synchronous machines or PMSMs	Nonsalient-pole synchronous machines		
			Indirect cooling		Direct cooling
			Air	Hydrogen	Water
A-kA/m		30-65	30-80	90-110	150-200
J-A/mm^2	Stator winding	4-6.5	3-5	4-6	7-10
J-A/mm^2	Field winding	2-4	3-5	3-5	6-12

2.5 Maxwell's Stress Tensor and Torque Production

Electric and magnetic loading are two main parameters of all electric machines determining the limits thus volume. While the electric loading determines the temperature, magnetic loading specifies the limits of magnetic materials. Another importance of these parameters is that, they are directly associated with torque production.

$$\sigma_F = \frac{1}{2}\mu_0 H^2 \tag{2.12}$$

Maxwell's stress theory indicates that, magnetic stress is generated in the vacuum between two objects having magnetic field. This stress is expressed as equation (2.12).

$$\sigma_{Fn} = \frac{1}{2}\mu_0 (H_n{}^2 - H_{\tan}{}^2) \tag{2.13}$$

$$\sigma_{F\tan} = \mu_0 H_n H_{\tan} \tag{2.14}$$

It is also beneficial to further look into this stress and divide it into tangentinal and normal components as given in equations (2.13) and (2.14). Applying Ampere's law to a current carrying single slot and corresponding rotor surface, equation (2.15) is found when permeability of iron is considered to be infinite.

$$H_{\tan} = A \text{ and } B_{\tan} = \mu_0 A_m \tag{2.15}$$

By using (2.15), (2.14) can be rewritten as (2.16).

$$\sigma_{F\tan} = B_{\mathrm{n}} A \tag{2.16}$$

Equation (2.16) can be further modified to give instantaneous value of tangentinal stress according to time and position as shown in equation (2.17).

$$\sigma_{F\tan}(x,t) = B_n(x,t) A_m(x,t) \tag{2.17}$$

Equation (2.17) gives tangentinal stress according to position and time in terms of position and time dependent normal flux density (magnetic loading) and linear current density (specific electric loading). Values for magnetic and electric loadings are presented in Table 2.3.

Equation (2.17) can also be modified to depend on RMS value of the linear current density and peak value of the flux density if current and flux density is assumed to be sinusoidal. Equation (2.18) is the modified version of equation (2.17) where power factor is also taken into consideration because of its relation with current.

$$\sigma_{F\tan} = \frac{A_{m-RMS} B_{mg} \cos\varphi}{\sqrt{2}} \tag{2.18}$$

Finally by using directly equation (2.19) and motor parameters torque value can be reached. Torque is produced when there is a magnetic tangentinal stress on a surface [30].

$$T = \sigma_{F\tan} r_r S_r = \sigma_{F\tan} \pi \frac{D_r^{\,2}}{2} l' \tag{2.19}$$

Table 2.3: Specific magnetic loading, electric loading and tangentinal stress values for different types of machines [30].

	Salient-pole synchronous machines or PMSMs	Nonsalient-pole synchronous machines		
		Indirect cooling		Direct cooling
		Air	Hydrogen	Water
Electric loading [kA_{RMS}/m]	35-65	30-80	90-110	150-200
Magnetic Loading [T]	0.85-1.05	0.8-1.05	0.8-1.05	0.8-1.05
Tangentinal stress	33500	36000	65500	114500

2.6 Inductances and Flux Linkages

Inductances are very important parameters determining the characteristics of setups including windings and magnetic cores. Changing from simple to complex, inductance of a magnetic system is the key to understand its properties and behaviour. Generally when talking about inductances for synchronous machines, two inductances L_d and L_q are of greater interest which are shown in Figure 2.1.

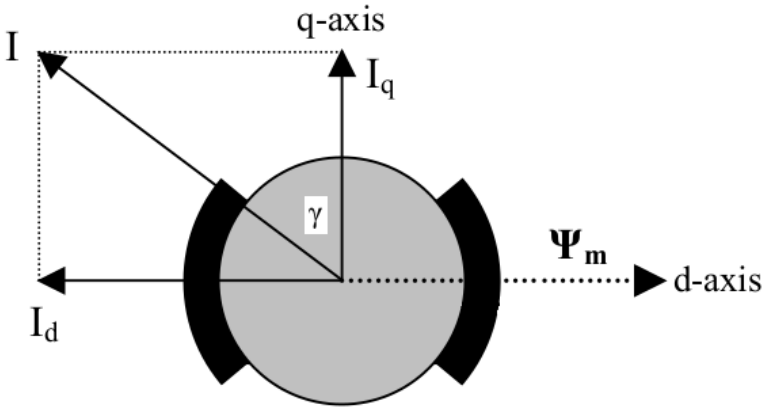

Figure 2.1: Rotor of a two pole SPM machine.

In equation (1.3) which is well known and widely used expression when analysing a synchronous machine , torque is expressed in terms of flux linkages and these inductances.

$$L_d = L_{md} + L_{s\sigma} \tag{2.20}$$

$$L_q = L_{mq} + L_{s\sigma} \tag{2.21}$$

Equation (2.20) and (2.21) states that both d and q-axis inductances are composed of magnetizing and leakage inductances. In equation (2.22) and (2.23) d and q-axis magnetizing inductances are given in terms of motor parameters.

$$L_{md} = \mu_0 \frac{2m\tau}{p\pi^2 \delta_{def}} l' (k_{w1} N)^2 \tag{2.22}$$

$$L_{mq} = \mu_0 \frac{2m\tau}{p\pi^2 \delta_{qef}} l' (k_{w1} N)^2 \tag{2.23}$$

Another important parameter is the flux linkage given in equation (2.24), if there is no saturation [22]. Here B_{mg} is the peak value of the air gap flux density and the flux linkage of d and q axes can both be found by using peak value of the d-axis and q-axis air gap flux density values.

$$\Psi_m = k_{w1} N \frac{2}{\pi} \tau l' B_{mg} \tag{2.24}$$

2.7 Losses of PM Machines

In any electric motor losses are divided into three categories which are electric, magnetic and mechanical losses. Stator copper losses, stray losses, stator and rotor core losses, friction and windage losses are seen in each type of motor if there is winding and electrical steel. Machine specific losses are magnet losses for PM motors, field winding losses for non-PM current excited motors and cage-copper losses for induction motors.

2.7.1 Copper and stray losses

Copper losses are classical joule losses that are very basic in electric circuits. In case of an electric machine copper losses are expressed as equation (2.25). Except in high speed motors where core loss of stator and rotor reaches very high values, copper losses are the main building block of losses in standart machines.

$$P_{cu} = m I_{RMS}^{\ 2} R_s \tag{2.25}$$

Stray losses consist of skin effect and proximity losses. Skin effect is the flow of AC current through the outer part of a conductor due to the occurance of high impedance caused by high magnetic flux in the center of a conductor. Equation 2.26 shows the skin depth of a conductor at a certain frequency. Proximity effect is the flow of current in unwanted patterns due to the magnetic fields created by near conductors. In a DC current flow skin effect and proximity effect can not be seen as they are both associated with varying magnetic fields.

$$\delta_{skin} = \sqrt{\frac{2}{\omega \mu_{cond} \sigma}} \tag{2.26}$$

R_s in equation (2.25) is considered to be nearly equal to the equivalent DC resistance conductor because these effects are generally occur in high frequencies. Moreover, in electric machines diameter of strands of a winding composing a coil is selected smaller than skin depth so that skin effect becomes negligible [32]

Another important point in copper losses is the temperature. As the temperature increases resistance of copper increases and this causes a further rise in copper losses. In order to correctly account for copper losses, temperature of the conductor has to be known.

2.7.2 Core losses

Core loss is divided into two parts, hystheresis and eddy current losses. Hystheresis loss occurs in molecular level by friction when there is a varying magnetic field. Eddy current loss occurs due to the circulating currents formed by induced voltage in the magnetic material in the presence of a varying magnetic field.

$$P_{core} = k_h B^2 f + k_c (Bf)^2 + k_e (Bf)^{3/2} \tag{2.27}$$

Equation (2.27) is mostly used for calculating the iron losses in electric machines, assuming flux density is sinusoidal [33]. Loss coefficients in equation (2.27) are obtained from manufactureres loss data by applying appropriate curve fitting.

There have been many investigations for core loss expression. Steinmetz, Jordan and Bertotti studied and many updates are applied by others. In [33], wide range investigation and comparison of various methods are represented.

2.7.3 Magnet losses

Eddy current losses and hystheresis losses are also seen in permanent magnets. Although they are very low to be neglected, they have to taken into consideration in a well designed machine. Also, it is necessary to know the magnet losses to get temperature distribution of a PM machine via static thermal or CFD analysis as well as equivalent circuit.

Eddy current losses are generally very low in permanent magnets so that they are neglected, especially in ferrite magnets which have high resistivity. However, in rare earth magnets, resistivity is low and this leads eddy current losses of rare earth permanent magnets to become relatively high.

$$P_{m-eddy} = \frac{V_m (b_m B_{mg} f)^2}{12 \rho_m} \tag{2.28}$$

Equation (2.28) gives the eddy current loss in permanent magnets according to physical dimensions, peak value of the flux density in magnet area, electrical resistivity and frequency.

Generally hystheresis loss of permanent magnets are not considered, but in [34], [35] and [36] hystheresis phenomena in magnets are investigated. Although there are no formulations presented, in [35] hystheresis loss of magnets are calculated by curve fitting using measured data assuming that hystheresis loss is proportional to the square of flux density.

Hystheresis loss of permanent magnets is a very deep, standalone topic to be investigated, but to sum up: other than in machines having strong armature reaction, permanent magnets operating in second quadrant does not have accountable hystheresis loss [36].

2.7.4 Windage losses

Windage losses are mechanical losses caused by the surrounding media of a rotating object. Imagine a solid rotating cylinder where there is air surrounding it. Since the air is not rotating itself, it shows a resistance to the movement of cylinder.

$$P_{Windage} = C_D \pi \rho_d w r^4 l' \tag{2.29}$$

Windage losses depend strictly on the rotating object. In case of a rough surface it becomes harder to analytically express the loss. In electric machines, windage loss depends on the rotor shape, stator tooth roughness and length of air gap. If the machine is a salient pole type where there are poles on the rotor surface causing a non-uniform air gap in radial direction it becomes harder to find windage loss analytically, for the other types of rotor where air gap is mechanically uniform in radial direction windage loss is expressed as equation (2.29) [37].

$$\mathrm{Re} = w\frac{\rho_d}{\mu} l_{gap} \tag{2.30}$$

$$\frac{1}{\sqrt{C_d}} = 2.04 + 1.768 \ln(\mathrm{Re}\sqrt{C_d}) \tag{2.31}$$

In equation (2.29) , Re can be find by using equation (2.30) where skin friction coefficient (for turbulent flow) is expressed as equation (2.31). It is also important to know that windage losses also change according to the temperature of air as the rotation itself causes heating. For more detailed extraction of windage losses CFD analysis is generally used in order to account for heating.

2.7.5 Bearing losses

Bearing losses are simply the losses caused by bearings. Bearings losses can be expressed by equation (2.32).

$$P_{Bearing} = 0.5 w k_b F_b D_b \tag{2.32}$$

in equation (2.32) is the force acting on the bearings and it is the mass of the rotor multiplied by the gravity [38].

2.8 Efficiency

Efficiency of the machine can be calculated considering all of the losses with equation (2.33) where mechanical power is the output torque multiplied by the rotation speed.

$$\eta = \frac{P_{mechanical}}{P_{mechanical} + P_{copper\&stray} + P_{core} + P_{magnet} + P_{windage} + P_{bearing}} \tag{2.33}$$

3. 27-SLOT 8-POLE MOTOR DESIGN

In the literature view (section 1.2.3) various hybrid motor design are reviewed and presented chronologically. The hybrid rotor topology proposed in [24] is used to increase average torque and decrease torque ripple by employing both internal permanent magnets and surface magnets on the same rotor. Authers have shifted the SPMs in order to further increase reluctance torque and enhance the torque characteristics. However, in case of a such structure there are many more parameters that can be examined to fully ascertain the characteristics. In order to do so, first an SPM and IPM benchmark is designed, then hybrid rotor is formed by using the benchmark motors as reference.

3.1 SPM Motor Design

It is convenient to start with relatively simpler motor (SPM) before designing IPM and hybrid motor. Here a benchmark SPM motor is used which is designed and manufactured in and for Akım Metal Sanayi ve Ticaret A.Ş. The motor is used for a servo application and its design criteria is given in Table 3.1. Design of the SPM motor is done analytically by using SPEED software and then it is verified by detailed FEA analysis using Flux2D.

Table 3.1: Design criteria of the SPM motor.

DC Voltage	21 V
Torque	3.85 Nm
Speed	2000 RPM
Cogging Torque	<5%
Torque Ripple	<5%

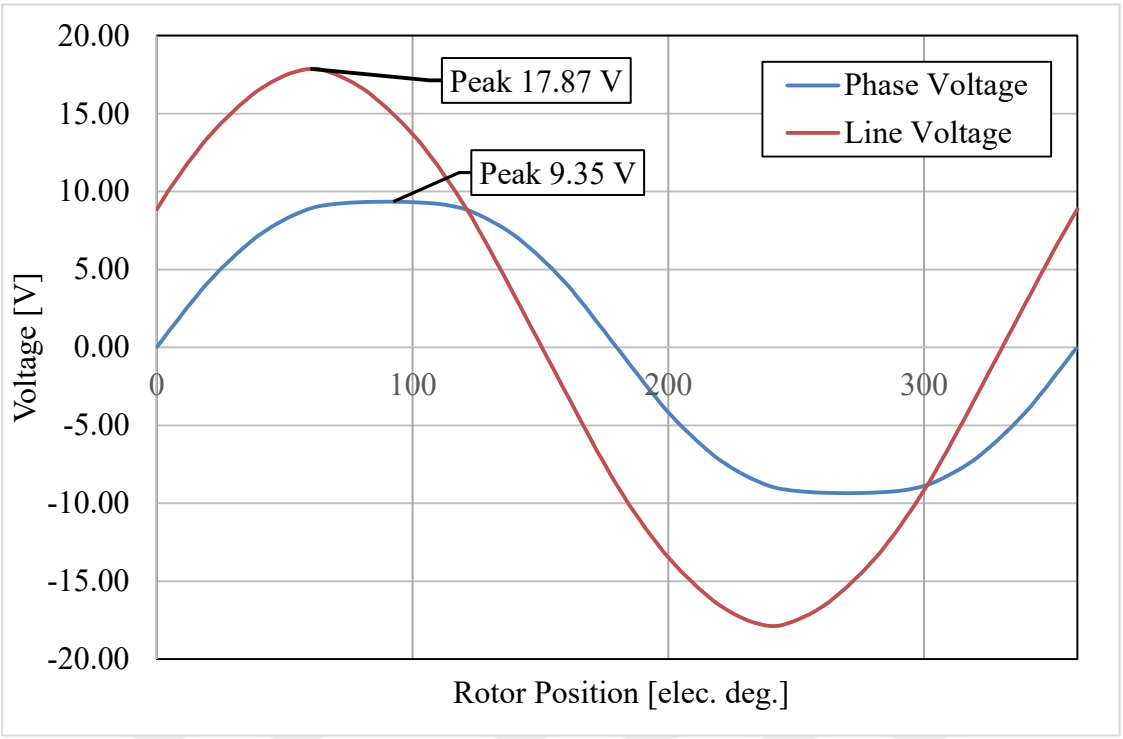

Figure 3.1: Phase and Line voltage waveforms of the initial SPM motor design obtained by SPEED software.

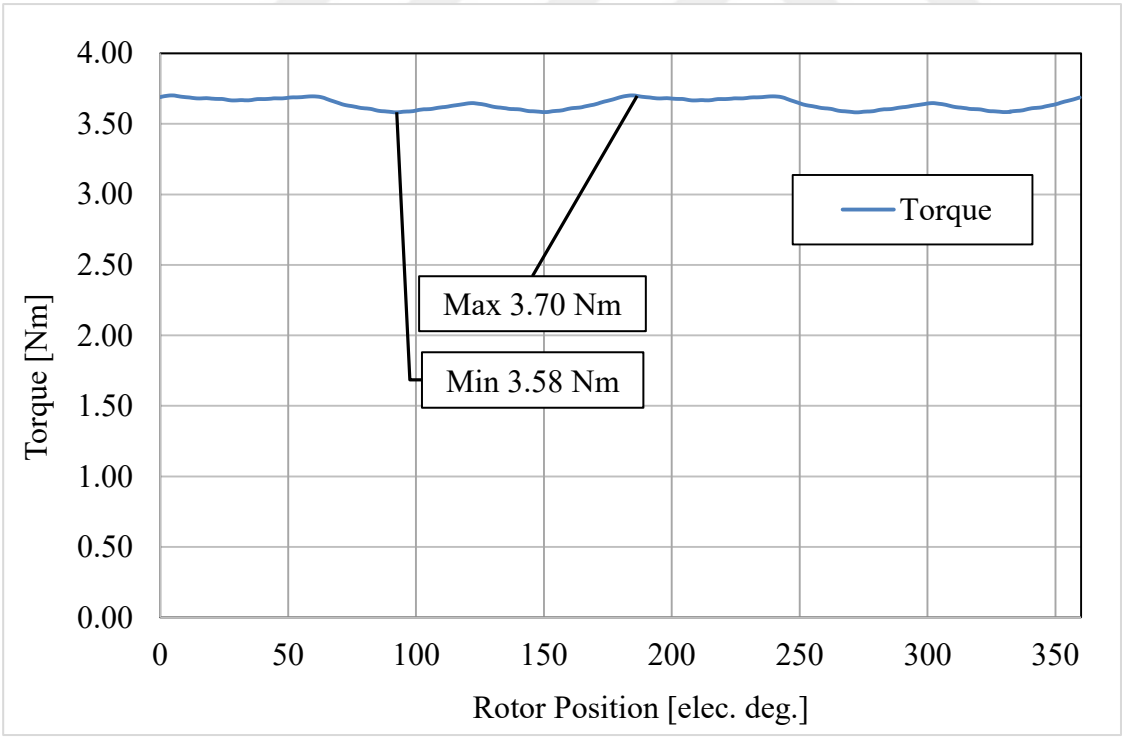

Figure 3.2: Output torque waveform of the initial SPM motor design.

3.1.1 Initial design with SPEED

In Figure 3.1 induced voltage waveforms of the initial design are given and in Figure 3.2 output torque waveform is given. Line voltage peak value is 17.87 V and average torque is 3.64 Nm. In Table 3.2 some performance characteristics are given. RMS value of the current density 5.7 which is a good value in order to limit heating. Stator teeth and yoke peak flux densities are 1.37 and 1.29 T respectively whereas peak flux density in the air gap is 0.97. Current density and flux densities in the motor are kept in the levels described previosly in [30]. Efficiency is calculated as 93.3% with a peak current of 50 Amperes. Stator and rotor lamination material is M270 steel and the permanent magnet is N30UH. (Further detail about the materials can be find in Appendix A and Appendix B). Winding configuration of the motor is given APPENDIX C.

Table 3.2: Other important parameters of the initial SPM motor design obtained by SPEED software.

J_{RMS}	5.7 A_{RMS}/mm^2
B_{st}	1.37 T
B_{sy}	1.29 T
Efficiency	93.3%
Peak Current	50 A

3.1.2 Detailed design with Flux2D (FEA)

It is convenient to do FEA analysis after the initial design with SPEED software as it gives more realistic results. In FEA analysis generally optimization is done because of unconvenient results obtained by other methods. Such optimization is done by varying pole-arc, motor axial length and air gap length, however only the final results will be given because of privacy. Cogging torque and induced voltage waveforms are investigated at no-load condition and output torque is obtained at on-load conditions.

3.1.2.1 No-load simulations

In Figure 3.3 no-load flux density distribution is presented. Here maximum flux density on the legend is set to 1.5 T because other than tooth tips of stator, maximum value for the flux density is 1.5 T. Figure 3.4 shows the cogging torque waveform with maximum and minimum values. It is known that, cogging torque of a PM machine is very critical because it can affect overall torque and can cause vibrations. It is the reason in the first place to choose a 27-slot 8-pole combination as it can provide smooth torque characteristics with low torque ripple and THD.

Figure 3.5 shows the induced voltage waveforms of the final design at 1000 rpm. It can be seen that line voltage waveform is a very fine sinusoidal and it meet the demand of 21 V DC voltage at 2000 rpm. In Figure 3.6 harmonic spectrum of the phase and line induced voltages are depicted. Line voltage waveform, which is directly in use in drive circuit has very little harmonic distortion with 0.34%. Such a value is very good for electric motors. Total harmonic distortion for the phase voltage is 9.31%.

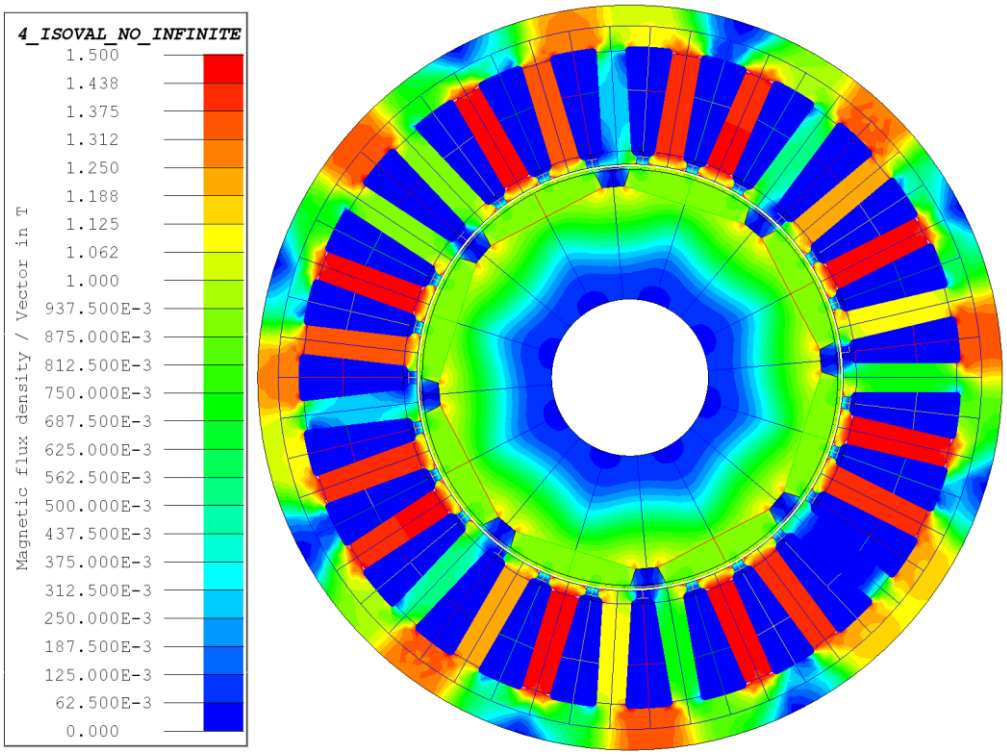

Figure 3.3: No-load flux density distribution obtained by 2D FEA.

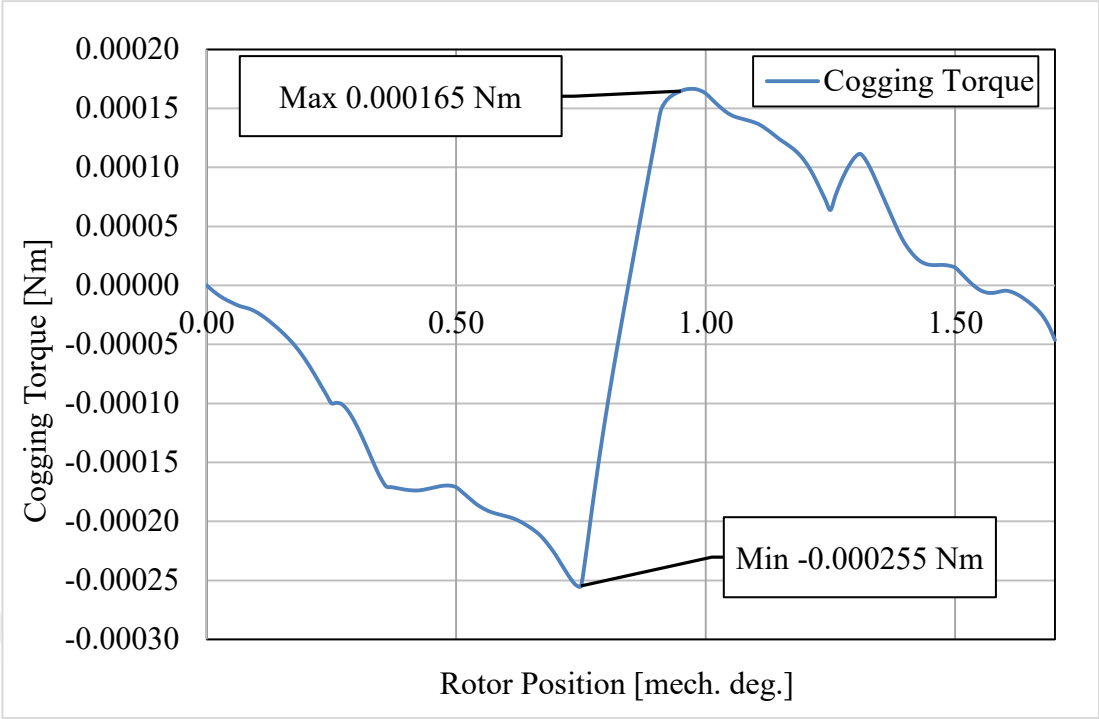

Figure 3.4: Cogging torque waveform of final SPM motor design obtained by 2D FEA.

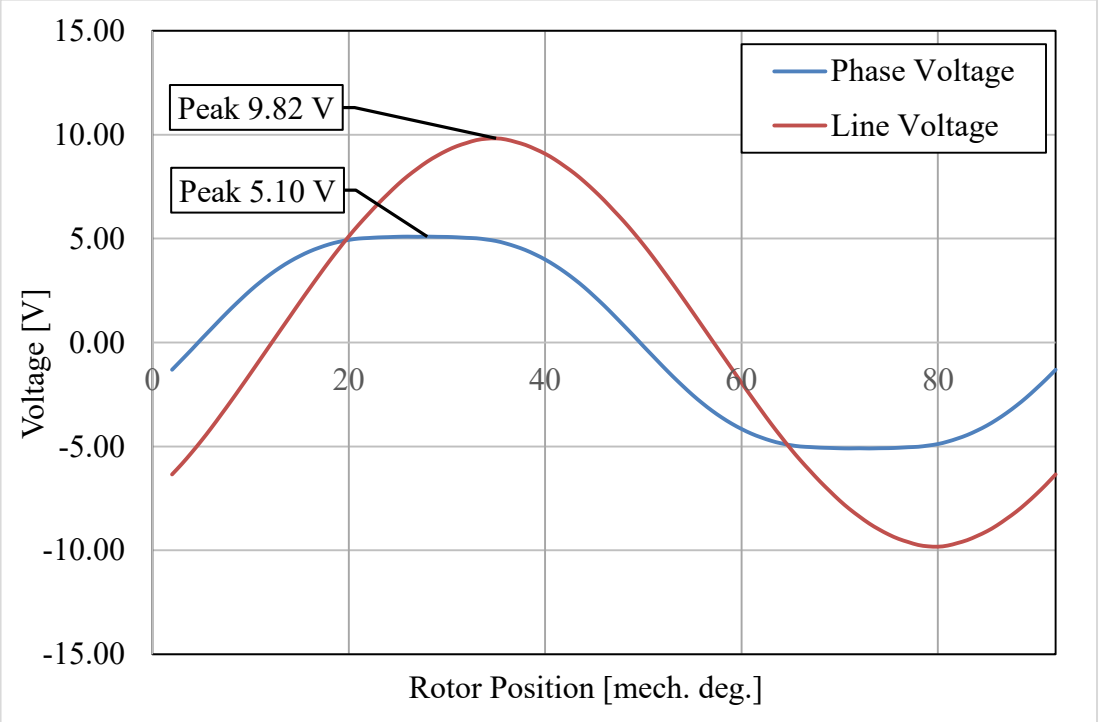

Figure 3.5: Phase and line induced voltage waveforms obtained by 2D FEA.

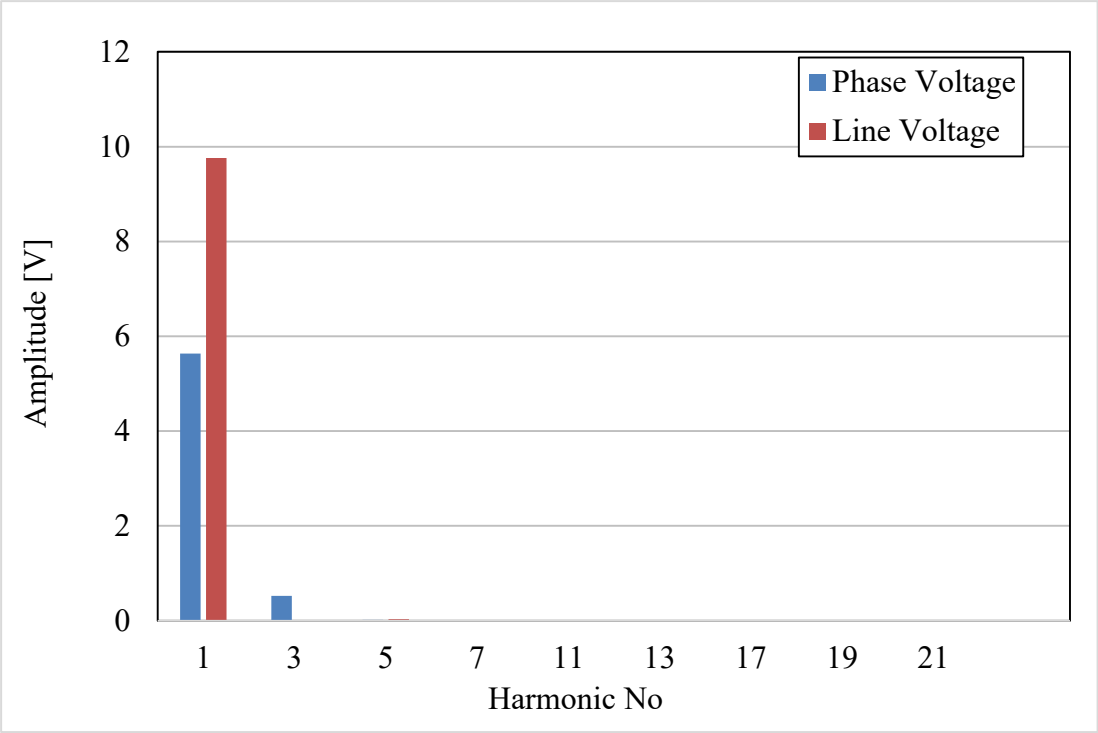

Figure 3.6: Harmonic spectrum of the final SPM motor design according to BEMF data obtained by 2D FEA.

3.1.2.2 On-load simulations

In Figure 3.7 output torque waveform is shown. Another zoomed view is also included in the figure to show maximum and minimum values of the output torque waveform. Maximum value of the torque is 4.004 Nm and minimum value is 3.973 making an average of 3.984 Nm with 0.77% torque ripple. Low cogging torque, low THD and low torque is obtained by choosing a good combination of slots and poles with a good optimization afterwards.

Flux density and flux lines distribution is also obtained by 2D FEA analysis and are depicted in Figure 3.8 and Figure 3.9 respectively. Maximum value of the flux density is again limited with 1.5 T and it is seen that only small areas in tooth tips exceed that value. Flux lines distribution is a little bit complicated because of the asymmetric magnetic structure of the motor. It is seen that stator teeth share flux for consequent poles.

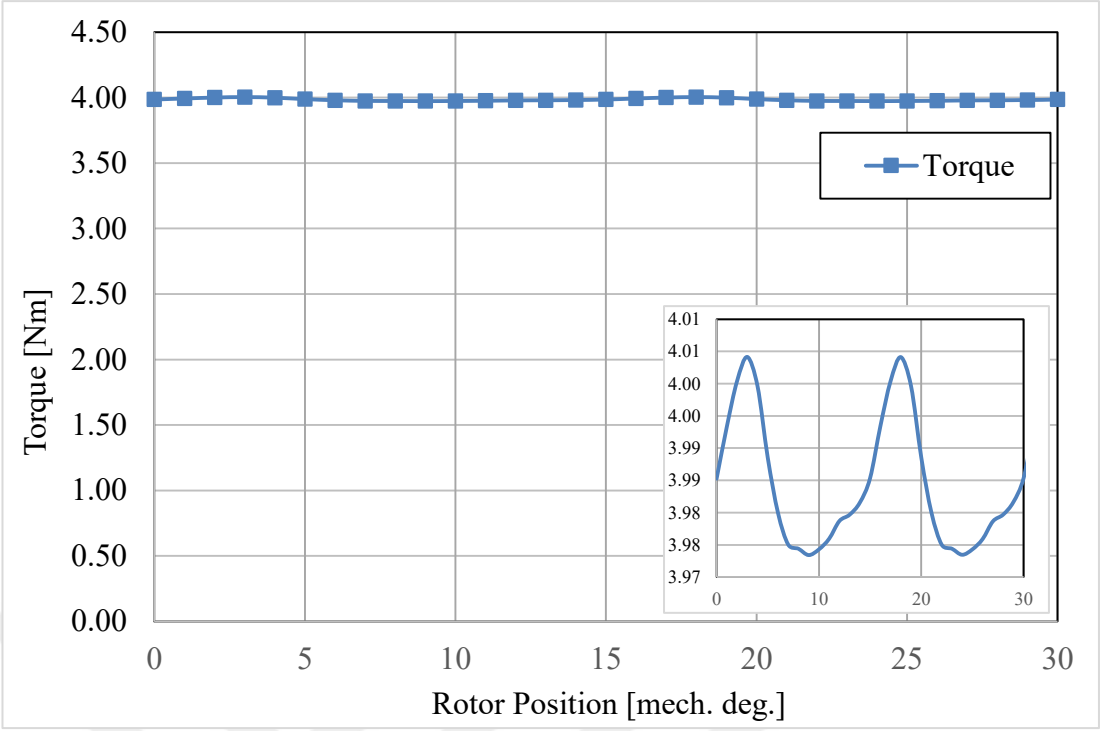

Figure 3.7: Output torque of the final SPM motor design obtained by 2D FEA.

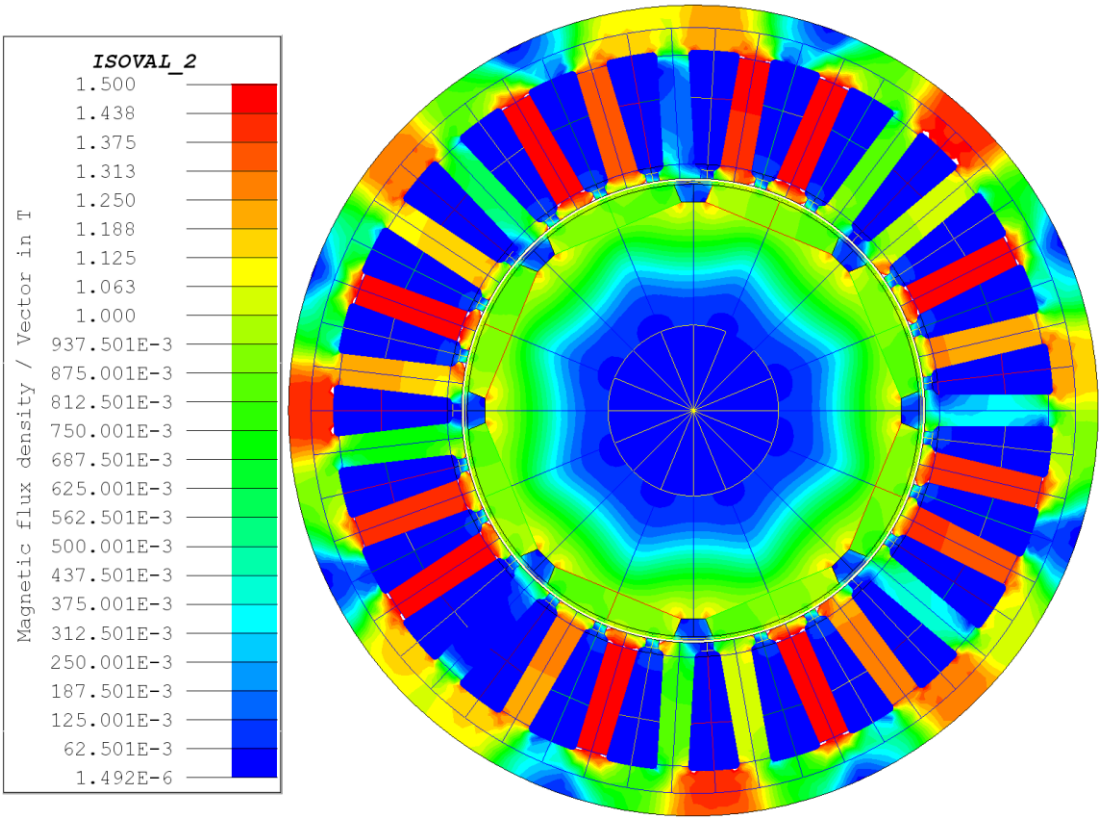

Figure 3.8: On-load flux density distribution of the final SPM motor design obtained by 2D FEA.

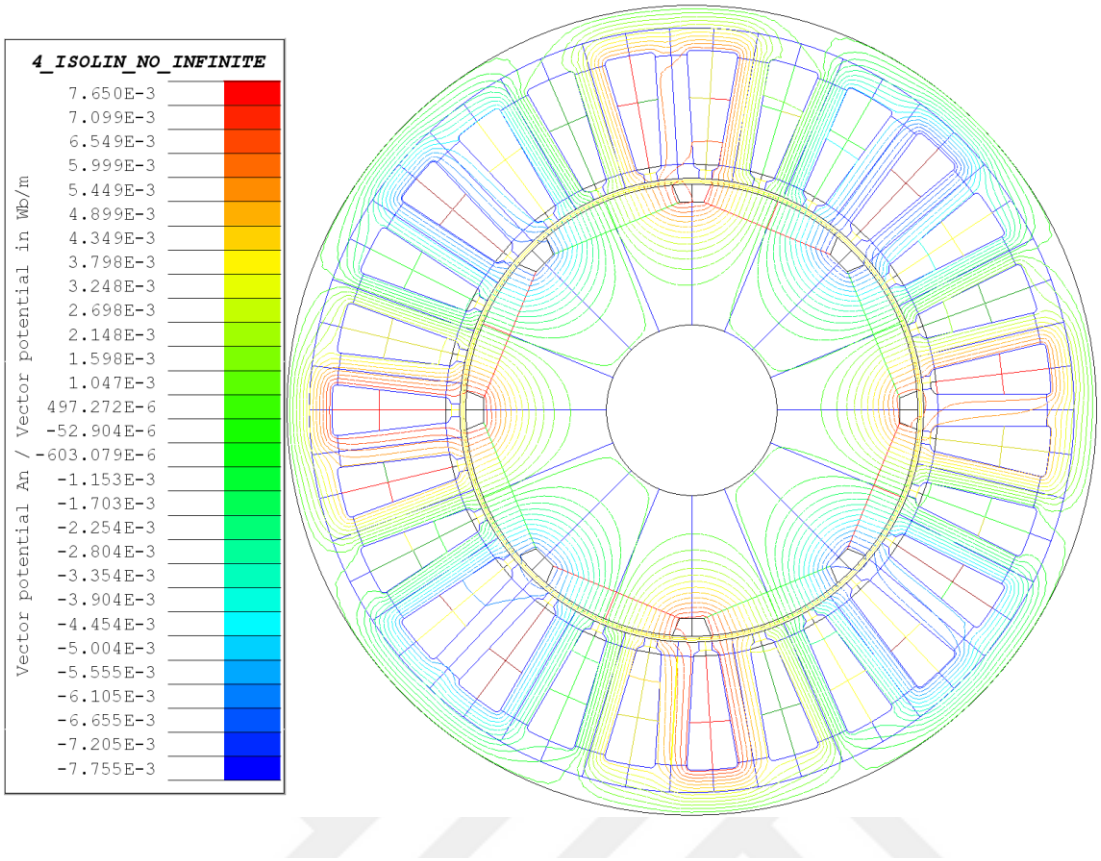

Figure 3.9: Flux lines distribution of the final SPM motor design obtained by 2D FEA.

3.2 IPM Motor Design

Since the SPM design is obtained, an IPM motor is designed by only editing the rotor. The IPM motor topology is chose to be well-known V-type. By taking the magnet volume of the SPM motor as a design constant, V-type motor is designed. The rotor radius of the SPM is 26.5 mm and the magnet area is 24 mm^2 with 58 mm stack length. These values are also kept constant.

IPM motor is designed so that it gives nearly the same average torque of SPM motor. In order to that, IPMs are preferred to be used in a long and narrow rectangular configuration because in other way thicker and shorter rectangular magnets had to be used and in such configuration desired average torque is hard to be reached. The drawback of using magnets like that is, the saliency of the machine becames small.

3.2.1 Detailed design with Flux 2D (FEA)

As ordinary analytical methods do not give realistic results in IPM motor design, IPM motor is studied by using 2D FEA.

3.2.1.1 No-load simulations

Flux density distribution of the designed IPM motor is shown in Figure 3.10. Again in this figure maximum value is limited to be 1.5 T in the legend. It is seen that upper parts of the magnets in the rotor region are saturated. This saturation is a special characteristics of a V-type machine because magnets are desired to be as close as possible to the rotor surface and at the same time they have to be distant enough to assure mechanical integrity. This makes the upper part region saturated because a portion of the magnets' flux is shorted through that area. The thickness of this region is 0.65mm as shown in the Figure 3.11. The shape of the magnet barrier is also optimized to give the lowest cogging torque and torque ripple. Figure 3.12 shows the cogging torque waveform of the IPM motor where 0.00056 Nm peak to peak cogging torque is obtained which is close to the 0.00042 Nm value of SPM motor. Phase and line induced voltage BEMF waveforms are shown in Figure 3.14 at 1000 rpm. Harmonic spectrum of the BEMF waveforms are presented in Figure 3.13 where amplitudes of the harmonics are shown. THD for phase voltage is 10.72% whereas line voltage THD is 0.48%.

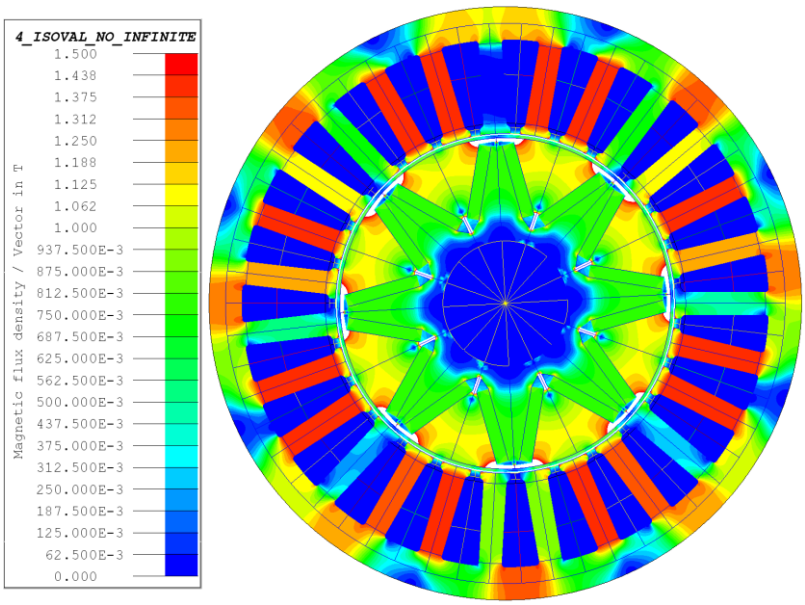

Figure 3.10: Flux density distribution of the IPM motor design on no-load condition obtained by 2D FEA.

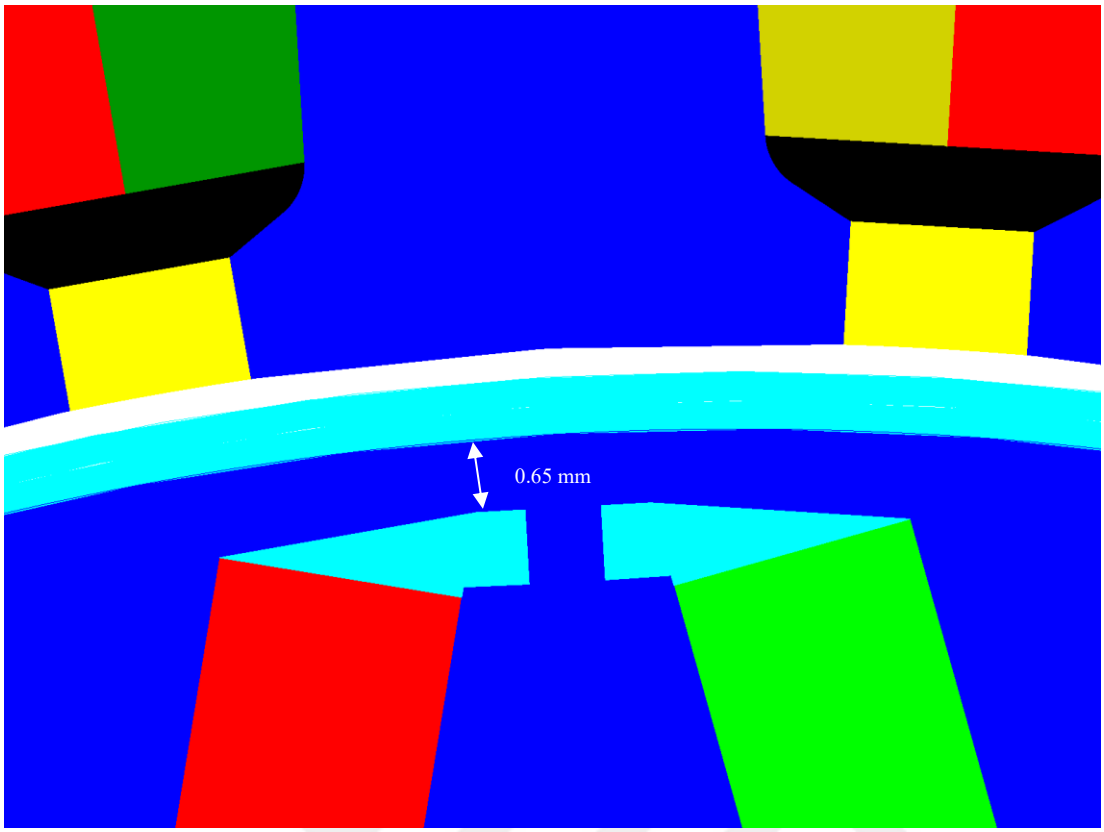

Figure 3.11: Shaped flux barrier of the IPM motor .

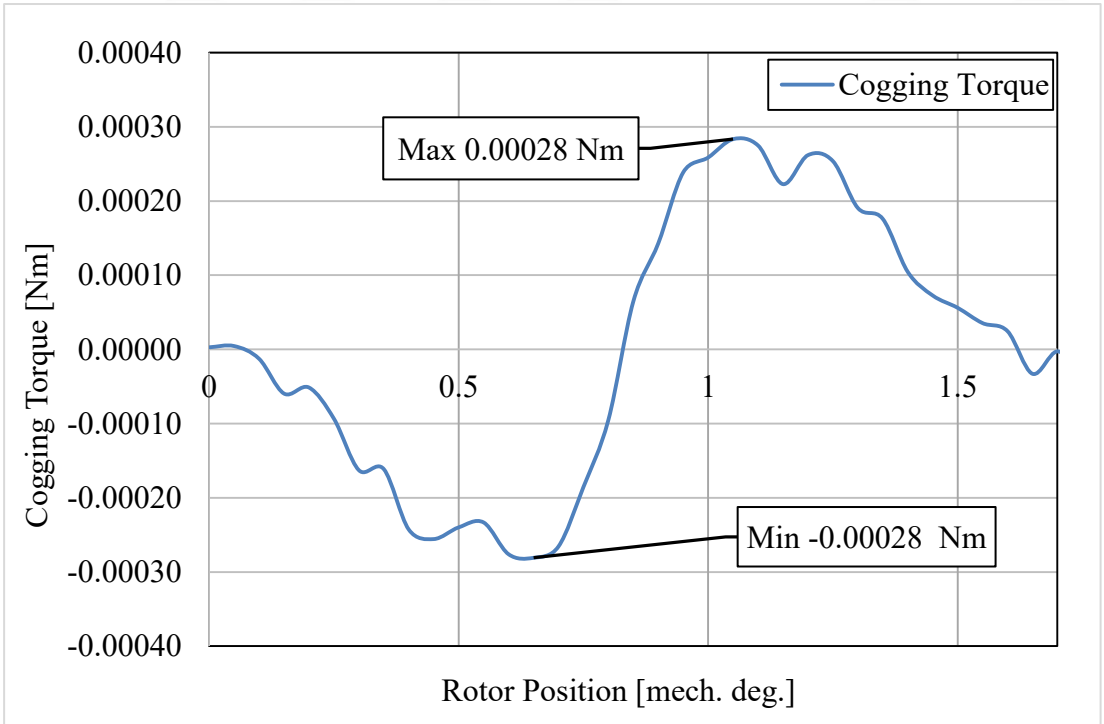

Figure 3.12: Cogging torque waveform of the IPM motor design obtained by 2D FEA.

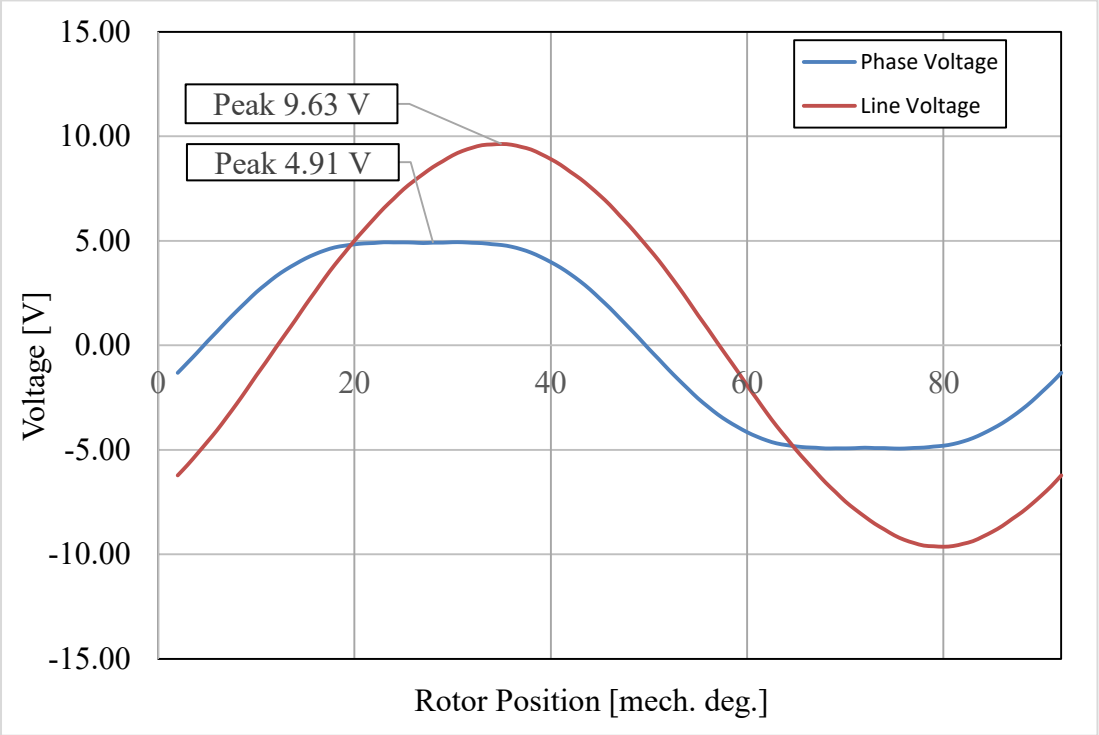

Figure 3.13: Phase and line induced voltage waveforms obtained by 2D FEA.

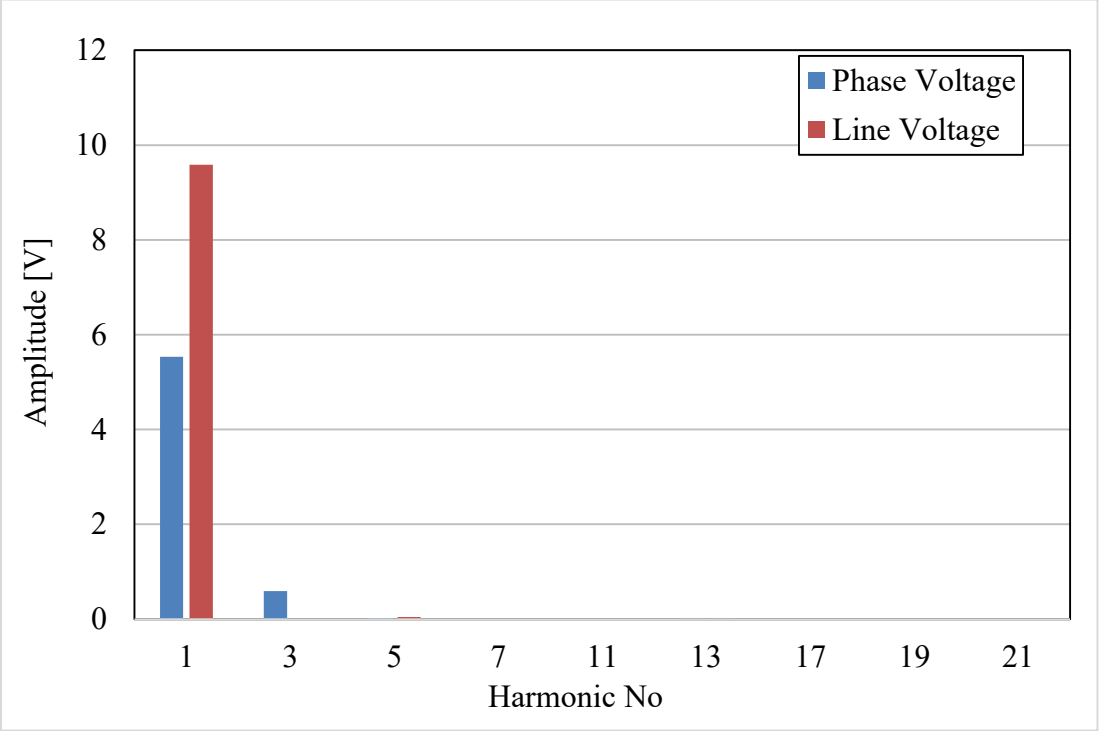

Figure 3.14: Harmonic spectrum of the IPM motor design according to BEMF data obtained by 2D FEA.

3.2.1.2 On-load simulations

In order to obtain the final design of IPM motor, V-angle (angle between two consequent rectangular magnets forming a pole) is varied between 30° to 74° in 2D FEA. The highest torque ripple with 5.41 % is obtained at 45° with 3.65 Nm average torque and lowest torque ripple is obtained at 70° with 0.5% torque ripple with 3.83 Nm average torque. The highest average torque obtained is 3.85 Nm with 1.7% torque ripple at 65°. The final design is thus chose to be the one having 70° V-angle. The output torque waveform is shown in Figure 3.15 and aforementioned optimisation is given in Figure 3.16 where coloring is applied according to torque ripple. Also zoomed view of the output torque waveform is illustrated onto the figure to clearly distinguish maximum and minimum points. In Figure 3.17 flux lines distribution is shown. Figure 3.18 shows the flux density distribution of the IPM motor on rated load. Maximum flux density value excluding the saturated rotor region is found to be 1.6 T.

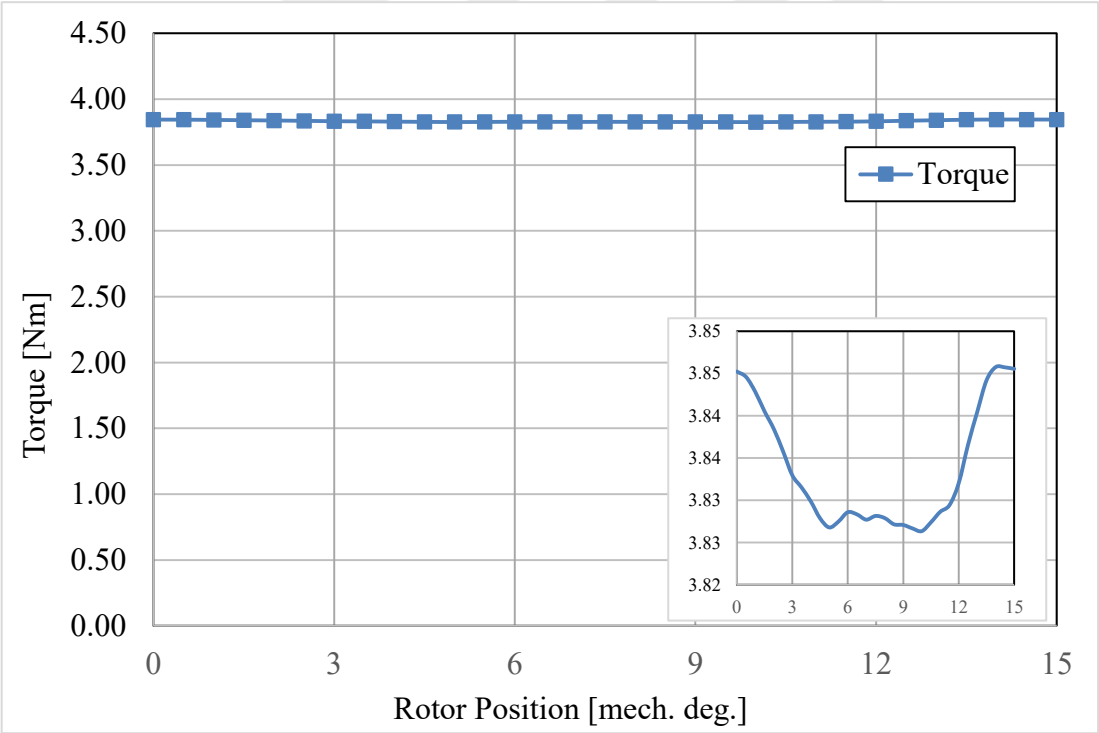

Figure 3.15: Output torque of the final IPM motor design obtained by 2D FEA.

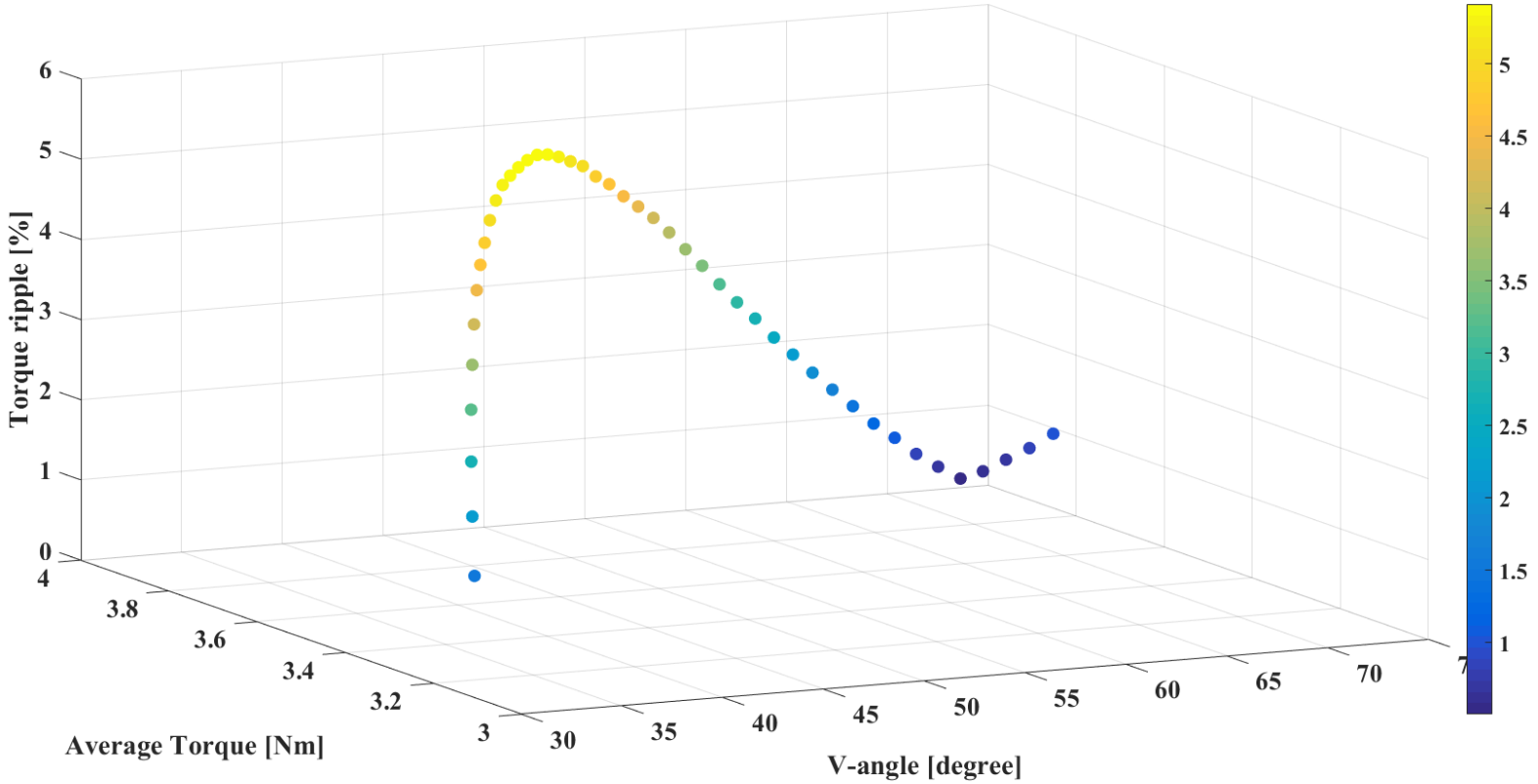

Figure 3.16: V-Angle optimization of the IPM motor.

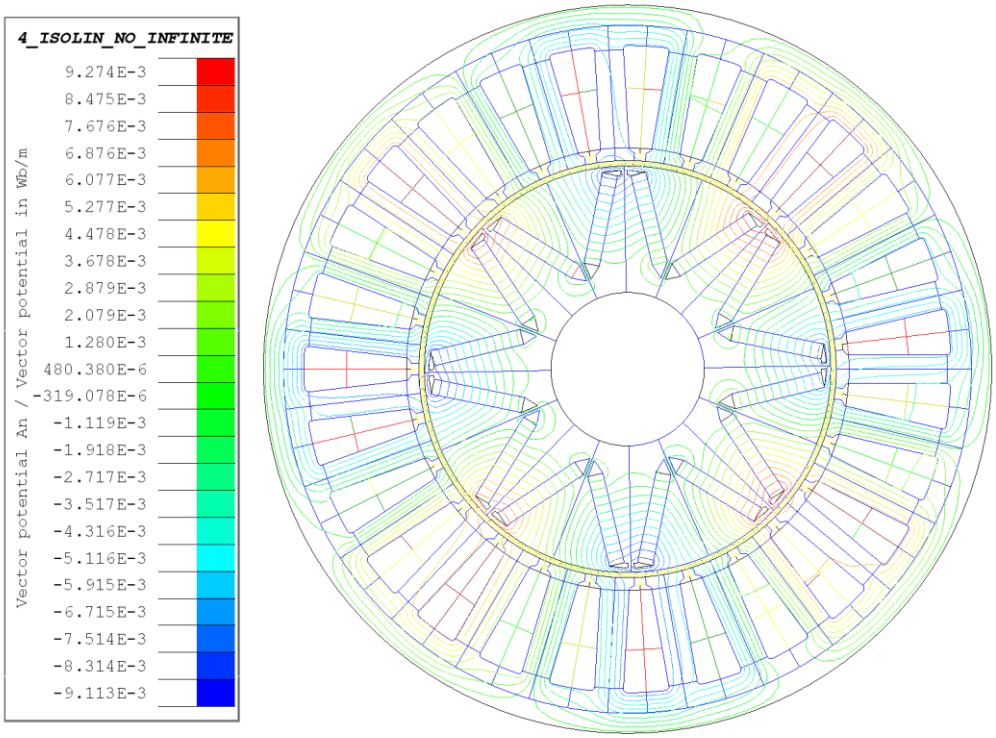

Figure 3.17: On-load flux lines distribution of the final IPM design obtained by 2D FEA.

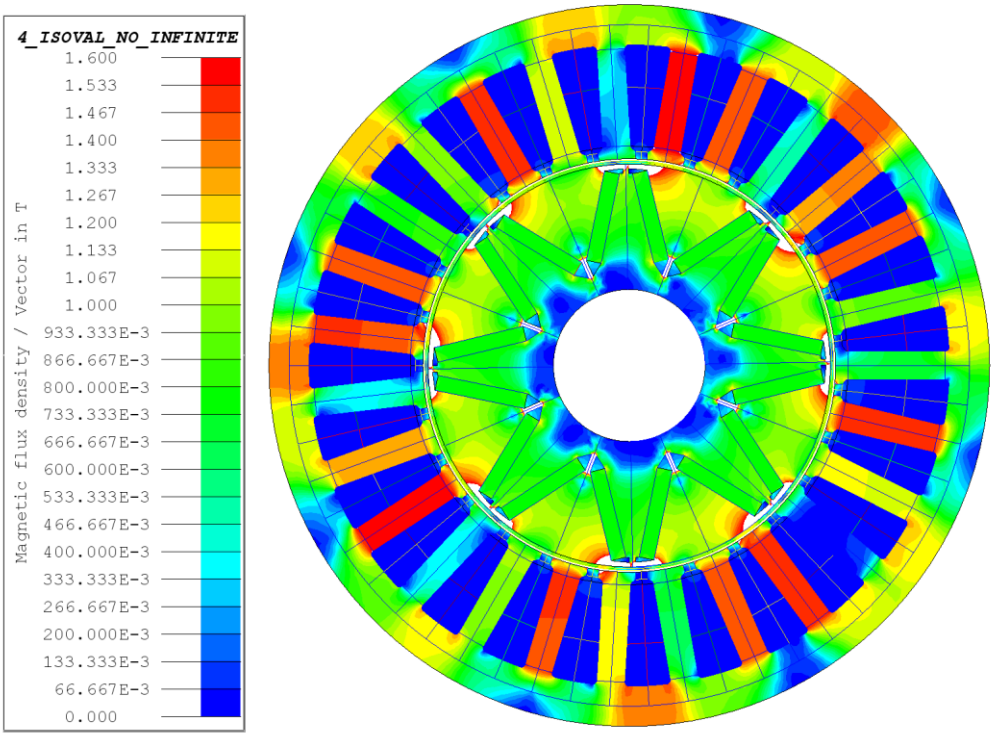

Figure 3.18: On-load flux density distribution of the final IPM design obtained by 2D FEA.

3.3 Hybrid Motor Design

Since two benchmarks are designed and analysed it is appropriate to move on with the design of the hybrid motor. Hybrid motor design will be done, first by employing the SPMs of the SPM motor and IPMs of the IPM motor directly on the same rotor which will be called as initial design, afterwards optimization will be done and final design will be obtained.

3.3.1 Initial hybrid motor design

For the preliminary design of hybrid rotor topology surface permanent magnets and internal permanent magnets are directly employed to a rotor with the same dimensions. No-load and on-load (rated) analysis are done to obtain cogging torque, induced voltages, THD and output torque.

3.3.1.1 No-load simulations

In Figure 3.19 preliminiary hybrid model is shown. V-angle of IPMs are 70^0 and pole-arc of SPMs are 141^o (electrical degree).

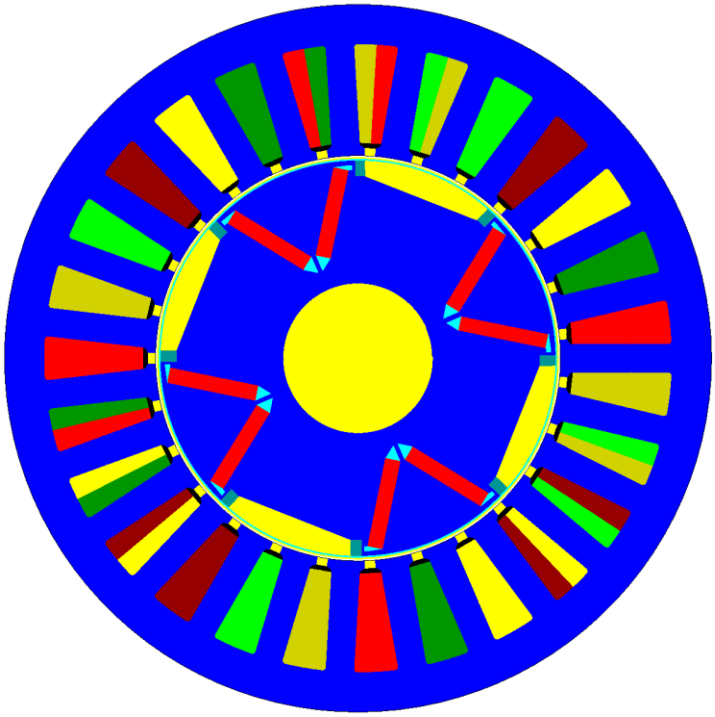

Figure 3.19: Initial hybrid motor design by directly placing SPM and IPM magnets.

In Figure 3.20 cogging torque waveform of initial hybrid design is shown. The peak value of the cogging torque is 0.0045 Nm which is 16 times the peak cogging torque of the IPM motor and 27 times the peak cogging torque of the SPM motor.

In Figure 3.21 phase and line induced voltage waveforms are given at 1000 rpm . Peak values of the line voltages of initial hybrid design and SPM motor is almost the same with 9.78V and 9.83 V whereas IPM motor has 9.63 V peak value which is slightly lower. Harmonic spectrum of the initial hybrid design is given in Figure 3.22, THD of phase voltage is 11.3% and the THD of line voltage is 0.24%.

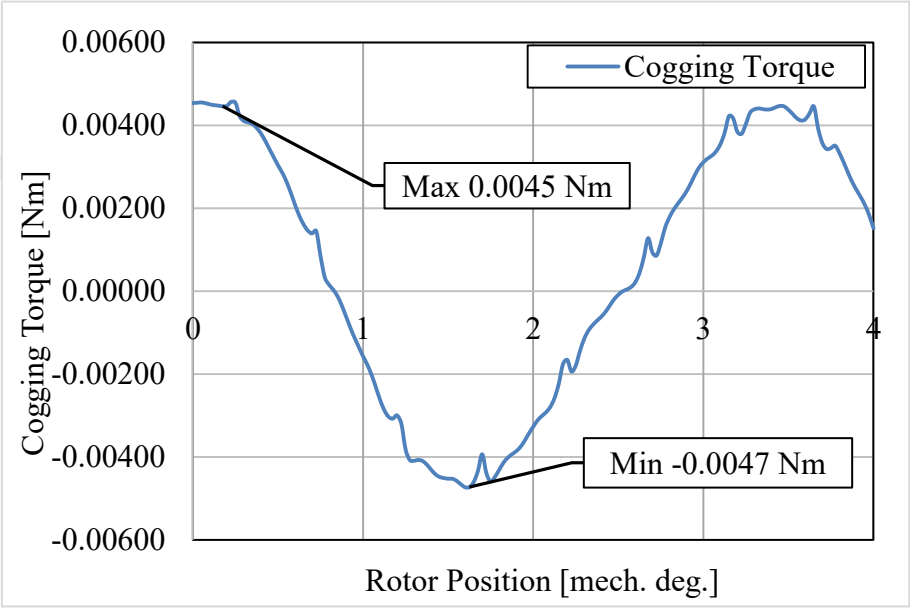

Figure 3.20: Cogging torque waveform of the initial hybrid design.

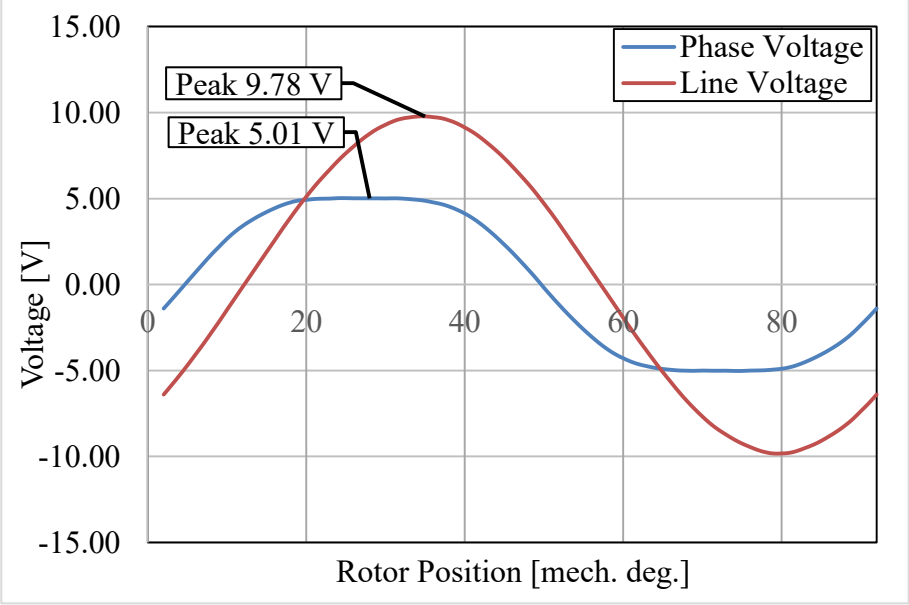

Figure 3.21: Phase and line induced voltage waveforms obtained by 2D FEA.

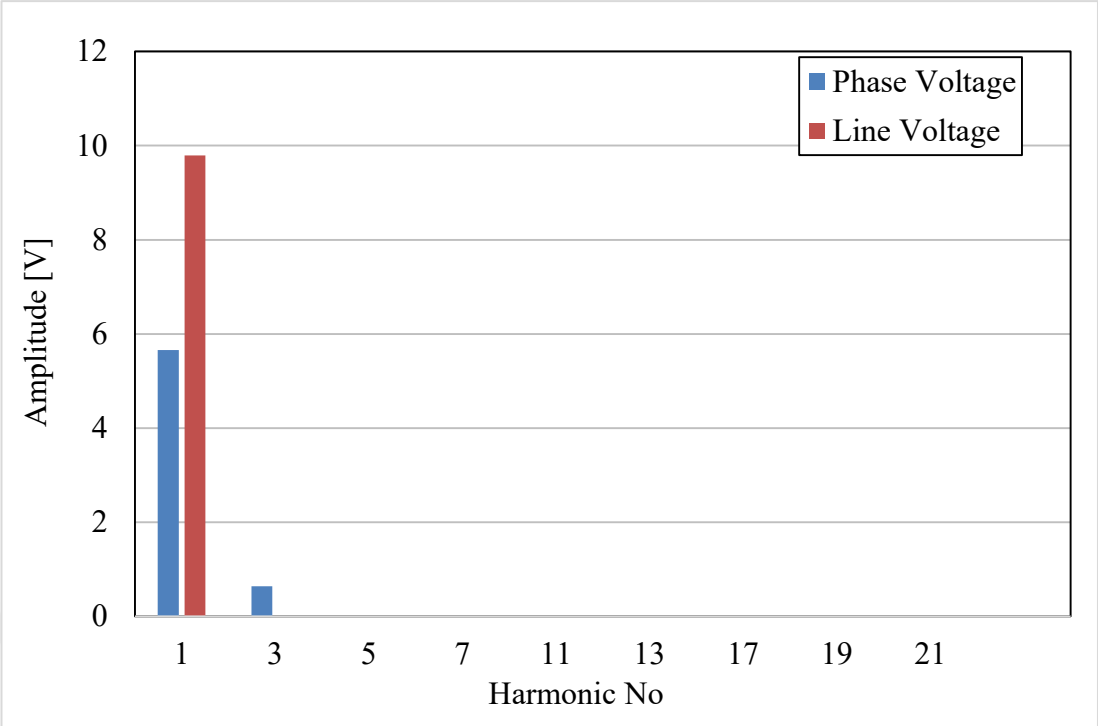

Figure 3.22: Harmonic spectrum of the initial hybrid design according to BEMF data obtained by 2D FEA.

3.3.1.2 On-load simulations

By using 2D FEA, output electromagnetic torque of initial hybrid design is obtained and shown in Figure 3.23. In this preliminary design, average torque is 3.97 Nm with 1.37% torque ripple. Peak to peak cogging torque to average value of the output torque value is thus 0.22%. Although the torque ripple and ratio of cogging torque to average torque is quite good alone, when they are compared with SPM and IPM motor they are not satisfying. The reason for this is the asymmetric structure of the 27/8 slot/pole combination which is further increased by employing SPMs and IPMs together. The assymmetric structure of 27/8 pole structure can be seen in Figure 3.24, in (a) and (b) where SPM and IPM motors' flux densities are shown, air gap flux density has a little asyymetry whereas in (c) air gap flux density of hybrid motor is has more as positive and negatatice peaks are not even similar in shape.

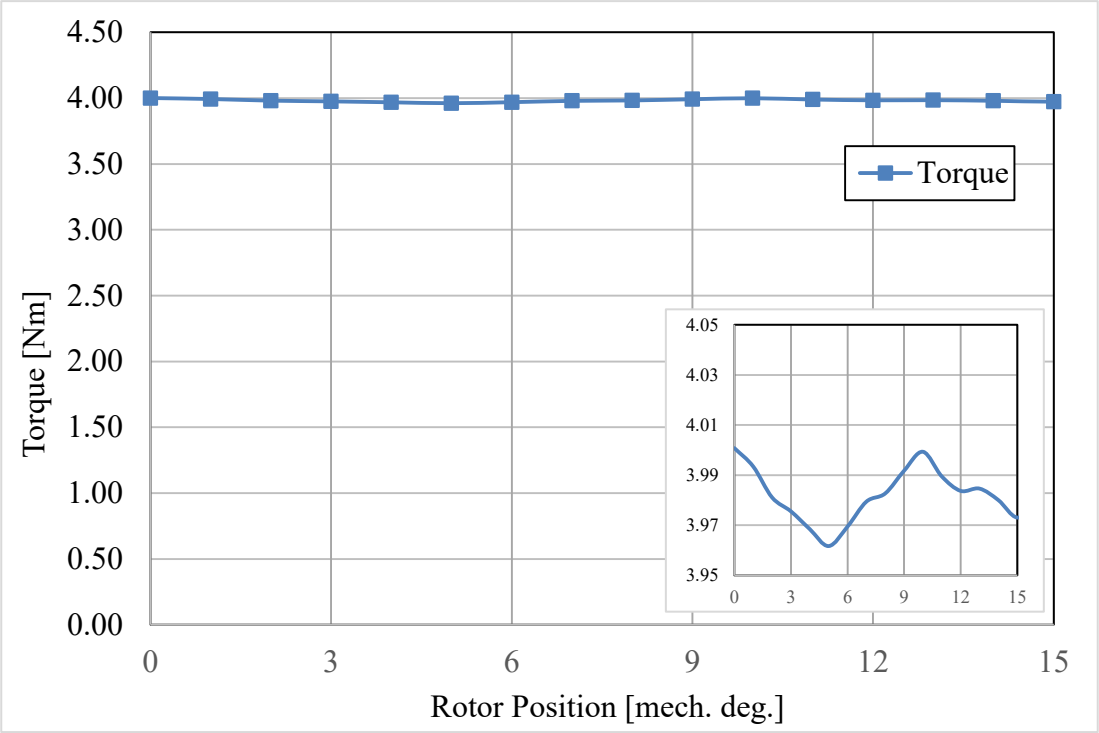

Figure 3.23: Output torque of the initial hybrid design obtained by 2D FEA.

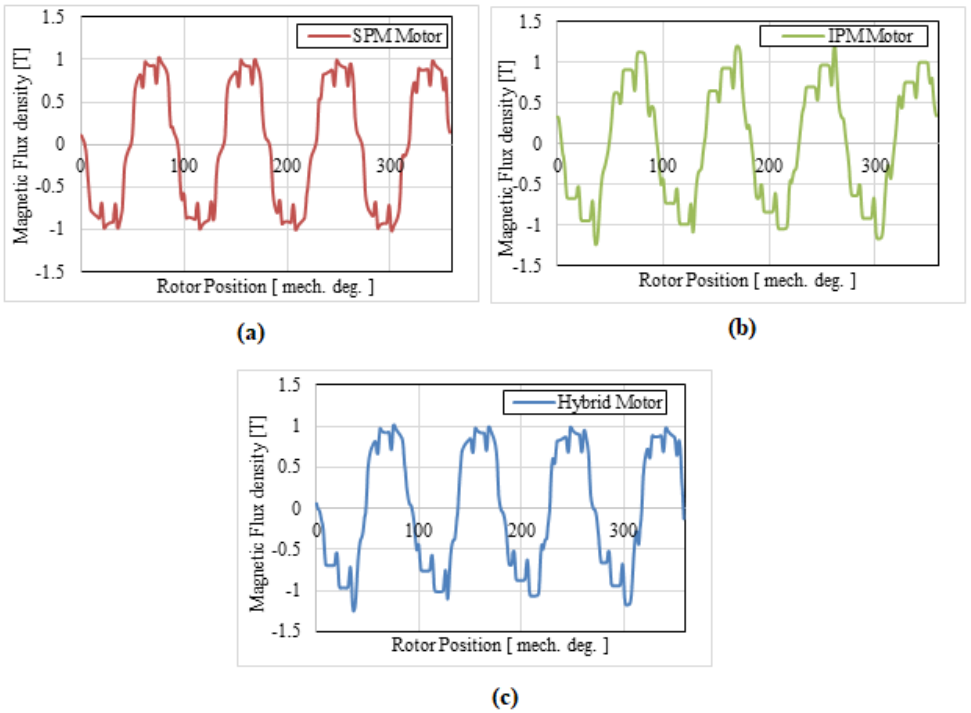

Figure 3.24: Air gap flux densities of three motors: (a) SPM motor, (b) IPM motor and (c) initial hybrid motor.

3.3.1.3 Optimization of hybrid motor

In the previous section, initial hybrid motor is formed by directly placing the magnets of SPM and IPM motors where 2D FEA analysis is done and presented for on-load and rated load conditions. It is seen that results are quite different than the SPM and IPM motors. In order to enhance the performance and investigate the capabilities of hybrid rotor, parametric variations are solved with FEA in order to optimize and find the best result.

In [24] where the hybrid rotor is first proposed only variation done after placing the magnets of SPM and IPM is the shifting of inset SPM magnets. It is shown that average torque and torque ripple may be improved by using such a configuration, however no other changes are applied to the rotor. The opportunities include reshaping of magnets, mainly pole arc of SPMs, redimensioning of rectangular IPMs as well as V-angle.

An optimization is done to achieve a certain value for a parameter or various parameters can be aimed to achieve by a very wide range optimization. In this study, aim is to achieve largest average torque and lowest torque ripple.

Two parametric analysis is held for the optimization where pole arc and V-angle are varied together for cogging torque and output torque. V-angle is varied in the range of 52^o to 70^o in 2^o steps and pole arc is varied in the range of 27^o to 43^o in a total 21 steps, making a total of 210 step analysis.

In general, cogging torque, THD and torque ripple of a motor is related to each other because they are formed by mainly slotting effects and space harmonics. For example if cogging torque is high, it is also exptected to have high THD and torque ripple. However hybrid structure is a special case with asymmetrical air gap flux density distribution and effects of different magnet variations may cause abnormal conditions where low cogging torque is obtained with high torque ripple. Foreseeing the possibility of encountering this, for the same parametric steps, two analysis is done to obtain cogging torque and output torque.

In Figure 3.25 cogging torque values in accordance with V-angle and pole arc variations are shown. It is seen, there is no pattern of flow from low to high which is a unique property of the hybrid rotor structure where assymmetry is highly seen. Maximum peak to peak value of the cogging torque is obtained as 0.047 Nm and minimum value is 0.001 Nm. Highest value of the cogging torque is approximately 5 times the initial hybrid design and the minimum value is one ninth of it, hence it is prooved that cogging torque value can be greatly reduced by proper changes applied to the magnet shapes. The lowest value obtained at 62^o V-angle and 36^o pole arc.

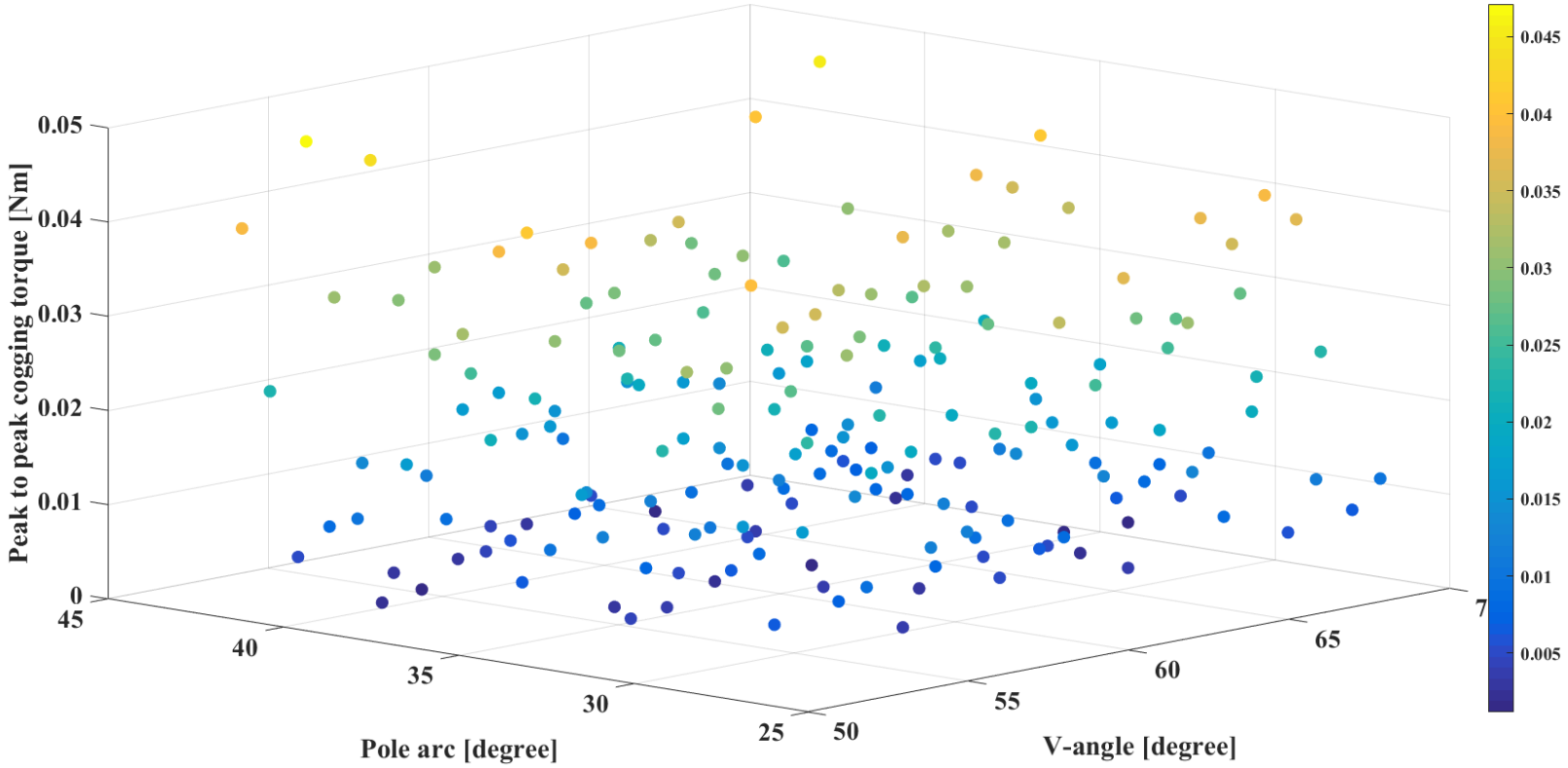

Figure 3.25: Peak to peak cogging torque value variation with changing V-angle and pole arc.

V-angle and pole arc variation and corresponding average torque and torque ripple results are presented in Figure 3.26 where points show the average torque values and coloring is made in accordance with torque ripple. According to the Figure 3.26, for a certain V-angle of IPMs, with increasing pole arc of SPms average torque increases and torque ripple decreases. Increase in average torque can be explained by increasing SPM volume. Maximum values of the average torque is obtained at near 43º pole arc for different V-angles and minimum values lie near 27º. Maximum torque ripple is obtained as 6% at 50º V-angle and 27º pole arc whereas minimum torque ripple obtained is 1.265% at 66º V-angle and 40.5º pole arc. It is interesting to note that, at the lowest peak to peak cogging torque value, average torque is 3.9 Nm with 2.63% ripple and at the highest peak to peak cogging torque value, average torque is 4.08 Nm with 2.32% ripple. As discussed previously, cogging torque and output torque designs are not in harmony with each other. If maximum average torque design is chose, which is at 56º V-angle and 43º pole arc, average torque is obtained as 4.08 Nm with 2.14% ripple whereas cogging torque peak to peak value is at one of its highest values, 0.047 Nm. If minimum torque ripple (with 1.265%) design is choose at 66º V-angle and 40.5º pole arc, cogging torque peak to peak value is 0.033 Nm where the average torque is 4.02Nm. At these values ratio of peak to peak cogging to average torque is 1.15% and 0.82% respectively.

It is shown that, by doing a wide range optimization slightly higher average torque can be obtained with higher torque ripple as well as higher cogging torque. Torque ripple and cogging torque values may be good enough when considered wihtout comparison, however when they are compared with previously designed SPM and IPM motors, they barely compete.

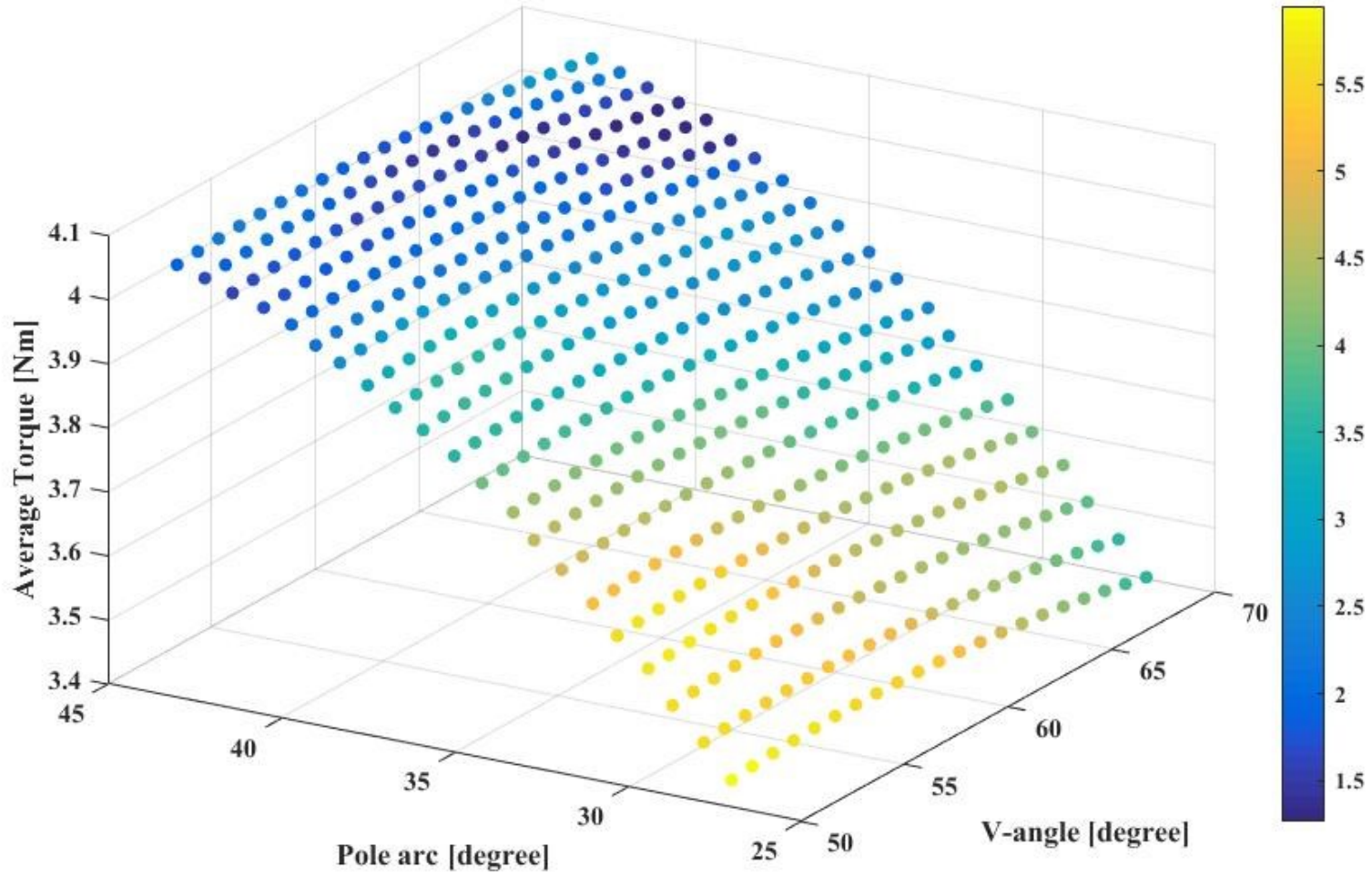

Figure 3.26: Average torque and torque ripple variation with V-angle and pole arc.

4. 48-SLOT 8-POLE DESIGN

In the previous chapter, 27-slot 8-pole IPM and hybrid motor designed and results are given. Wide range optimization is done by varying V-angle and pole arc of IPMs and SPMs. It is seen that when asymmetric structure of 27-slot 8-pole combination is brought together with further asymmetry by using surface and internal permanent magnets, obtained design could not compete with the SPM and IPM motors.

In order to investigate hybrid rotor structure in more detail, same steps will be repeated in this section on a 48-slot 8-pole integer slot motor. The reason for the choice of 48-slot 8-pole combination is that, its winding factor is high which means winding utilization is higher than other combinations. Also, an integer slot motor has poor performance when compared to fractional slot motors in terms of cogging torque, torque ripple and THD.

First, an SPM motor will be designed and optimised then an IPM motor will follow the same steps. After that, like in the previous chapter, hybrid motor will be designed and detailed analysis will be done.

4.1 SPM Motor Design

By using equations given in chapter 2, main dimensions of the machine is obtained for nearly 16 Nm. analytical design is accomplished. Winding of the machine is a double-layer winding where coils are placed in a slot adjacently, winding configuration is given in APPENDIX B. Current is 35.3 A_{RMS}. Air gap flux density is considered to be 0.95T and by building a simple reluctance equivalent model, magnet dimensions and flux density in stator teeth and yoke are roughly acquired. Slot dimensions are determined in order to limit current density to nearly $5A_{RMS}/mm^2$. Slot fill factor is limited to 40% and 9 strands of a coil with 0.95 mm diameter is chose.

Later by using SPEED, detailed dimensioning is done. Dimensions of the machine obtained by analytical methods and SPEED software is given in Table 4.1. In Table 4.2 analytically calculated performance values and SPEED (software) values are given for the decided dimensions. It is seen that good agreement is achieved between calculated values and SPEED outputs. Detailed design is needed in order to fully

evaluate motor performance to obtain cogging torque, THD and torque ripple. 2D FEA analysis is used further analyse and optimise the designed motor.

Table 4.1: Dimensions and important parameters of the designed motor.

Number of slots	48	
Number of poles	8	
Number of turns	2	
Rotor radius	50	mm
Air gap length	1	mm
Stack length	75	mm
Stator outer radius	83	mm
Thickness of a stator tooth	4.5	mm
Slot opening length	2	mm
Radial length of slot	20	mm
Radial length of slot opening	2	mm
Slot opening angle	20	^{o}
Number of strands	9	
Copper diameter	0.95	mm
Winding factor	0.966	
Air gap flux density	0.95	T
Tangential stress	13631	Pa
Electric loading	21360	A/mm
Rated speed	2000	RPM

Table 4.2: Calculated output data and SPEED design results.

	Calculated	SPEED	
Average torque	16.06	16.02	Nm
J_{RMS}	5.53	5.54	A/mm^2
Peak phase BEMF	42.3	40.6	V
Stator teeth flux density	1.3	1.21	T
Stator yoke flux density	0.8	1.08	T
Phase resistance	0.0285	0.0267	Ohm
Ld	0.18	0.191	mH
Lq	0.18	0.188	mH
Copper loss	106	100	W
Core loss	38.7	33	W
Magnet loss	1.3	1.44	W
Friction loss	0.67	-	W
Windage loss	0.16	-	W
Efficiency	95.76%	96%	

4.1.1 Detailed design with Flux 2D

In order to enhance motor performance, magnet shape optimisation is done by varying pole arc. Since there is a correlation with cogging torque value, THD and torque ripple, average torque and torque ripple are evaluated for different pole arcs. The results are given in Figure 4.1 Figure 4.2. It is expected to see increasing average torque with increasing pole arc of magnet as the magnet volume increases accordingly. However some positive and negative peaks are expected to be seeing in torque ripple with changing pole arc because magnet flux covers different number of stator teeth. Generally with increasing pole arc gives decreasing torque ripple as the magnet flux covers increased number of stator teeth. Average torque changes between 14 and 19 Nm in Figure 4.1 and torque ripple changes between 7.68% and 33%. Design point is chose to be the lowest torque ripple point with highest average torque which is at 154° (electrical degree) pole arc where 18.58 Nm average torque and 7.68% torque ripple is obtained.

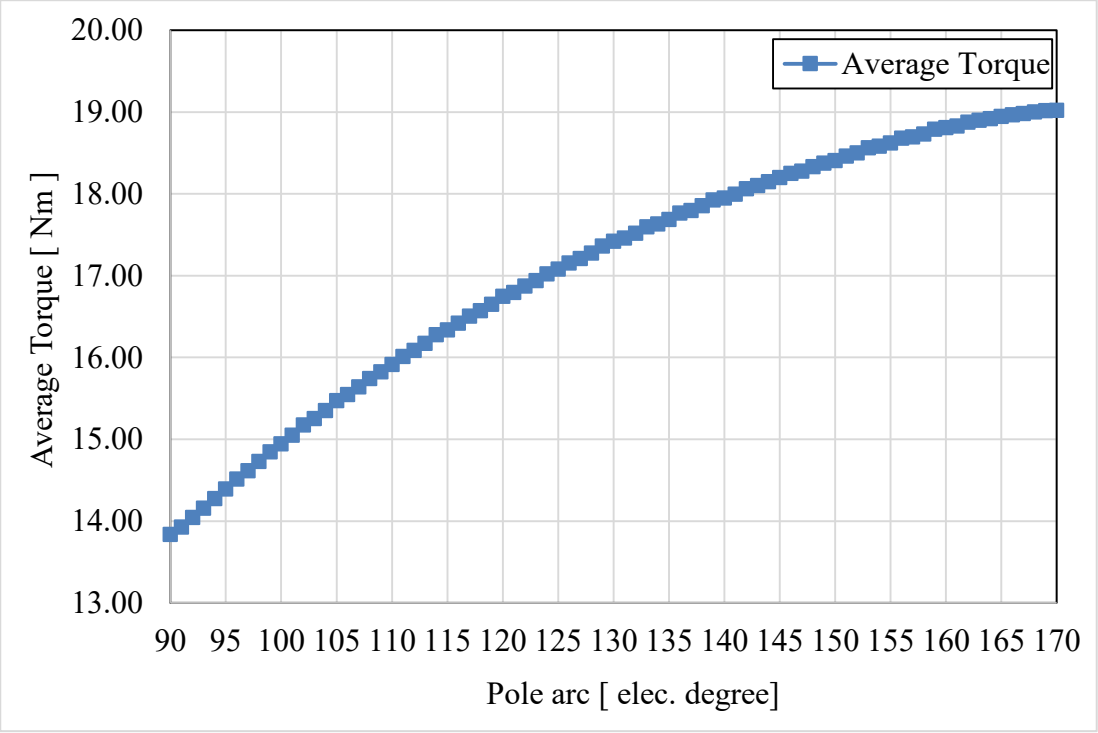

Figure 4.1: Variation of average torque with varying pole arc obtained by 2D FEA.

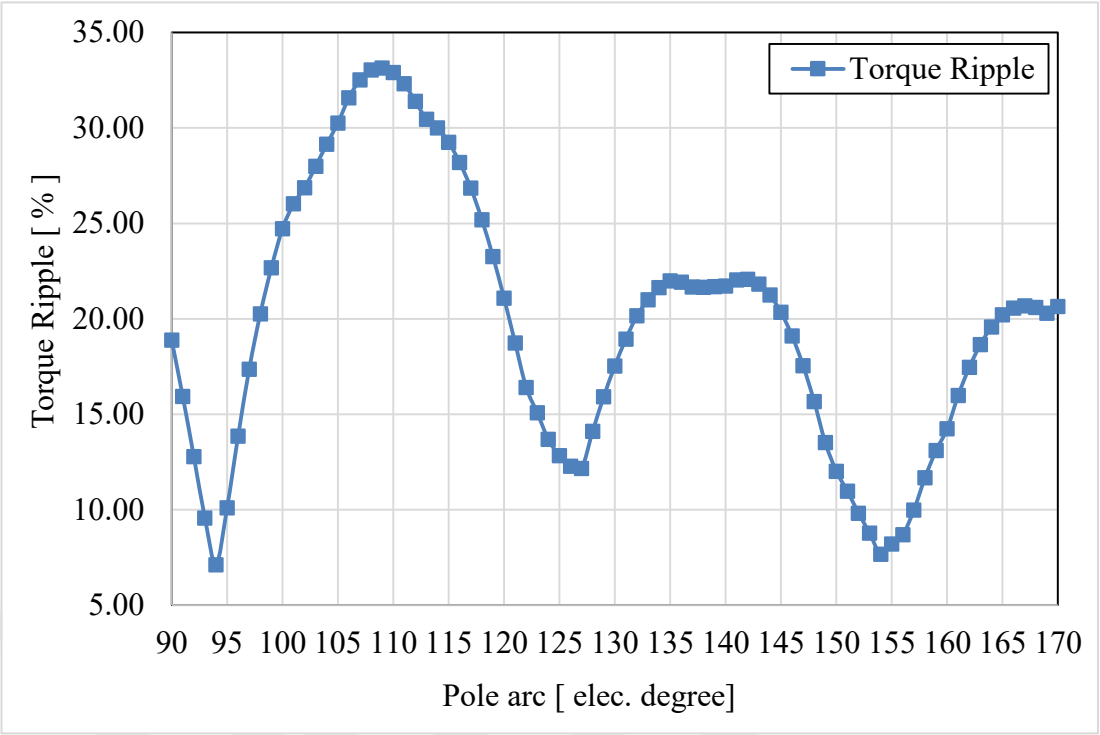

Figure 4.2: Variaton of torque ripple with varying pole arc obtained by 2D FEA.

4.1.1.1 No-load analysis

No load analysis is done in order to evaluate flux density distribution without armature effects. No load flux density distribution is obtained by using 2D FEA in FLUX 2D and it is given in Figure 4.4. Maximum flux density is limited to 1.5T in legend and the maximum value seen in the motor is lower than 1.5T close to 1.4T. It is important keep flux density around these values in order to limit core losses.

In Figure 4.3 cogging torque waveform is given where 0.6 Nm peak to peak value is obtained. Peak to peak cogging torque to average torque ratio is 3.22% which is a little high value for electric motors where smooth and vibrationless operation is desired.

Induced voltage waveforms are obtained for phase and line voltages and are given in Figure 4.5. It is seen that the waveforms are seen to be distorted which is caused by slotting effect. Integer slot choice is the main reason for this much distortion in waveform. Figure 4.6 shows the harmonic spectrum of the phase and line induced BEMF and it can be concluded that the machine is rich in harmonics. THD for phase voltage is 15.36% and 4.44% for line voltage. These amounts are also high in an electric motor, showing that higher order harmonics exist which causes high frequency iron losses in stator and rotor as well as in magnets.

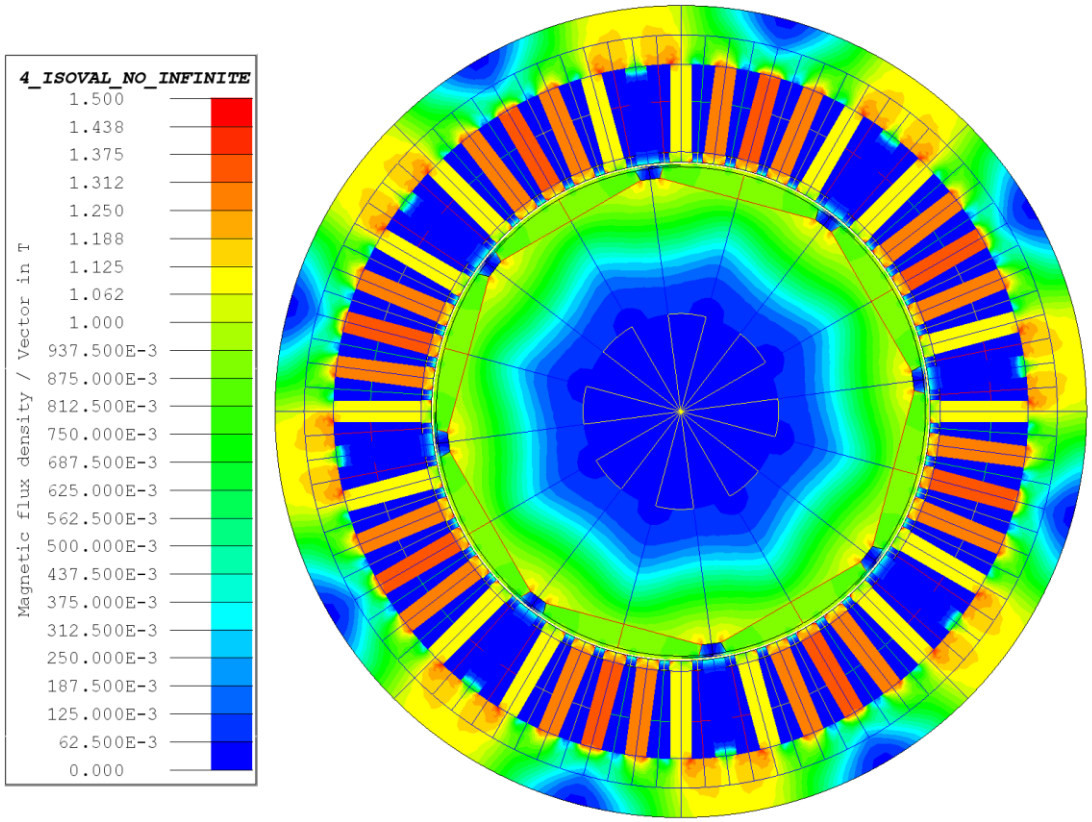

Figure 4.3: No load flux density distribution of the final SPM design obtained by 2D FEA.

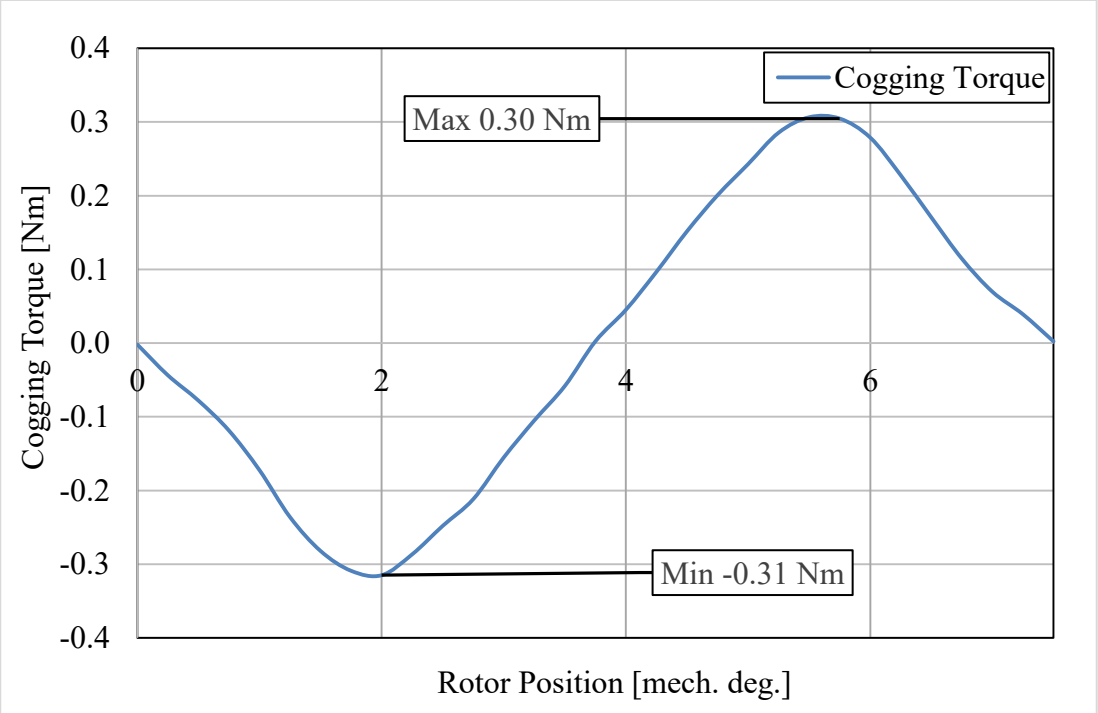

Figure 4.4: Cogging torque waveform of the final SPM motor design obtained by 2D FEA.

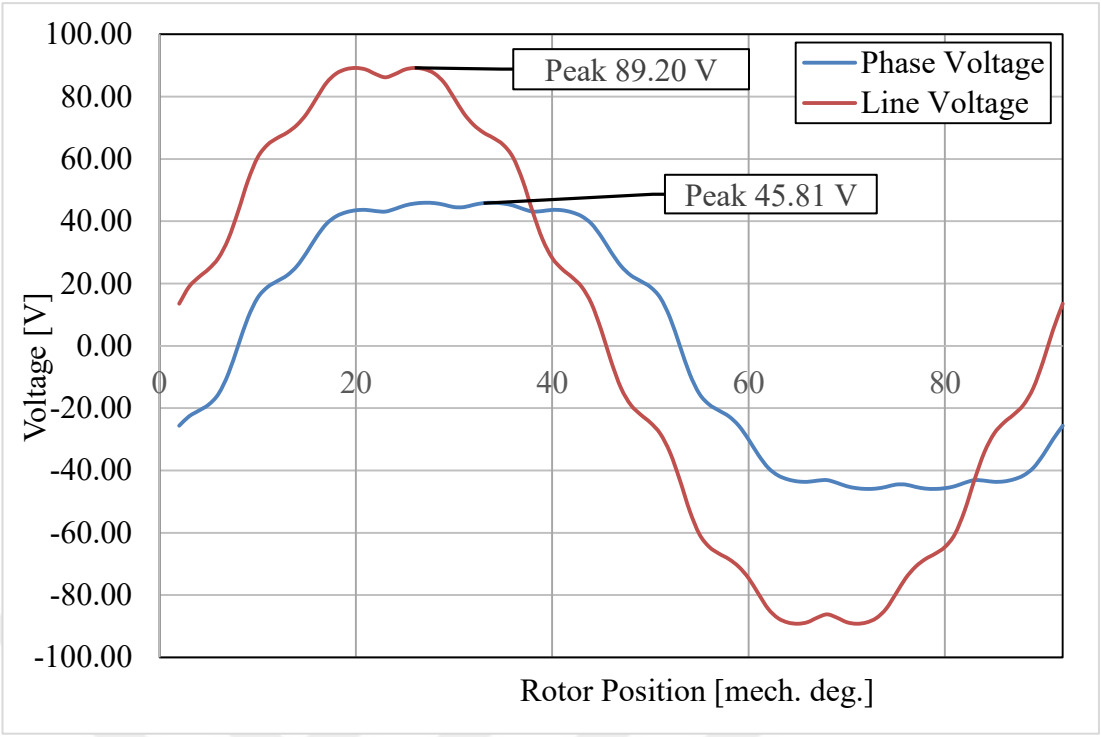

Figure 4.5: Phase and line induced voltage waveforms of the final SPM motor design obtained by 2D FEA.

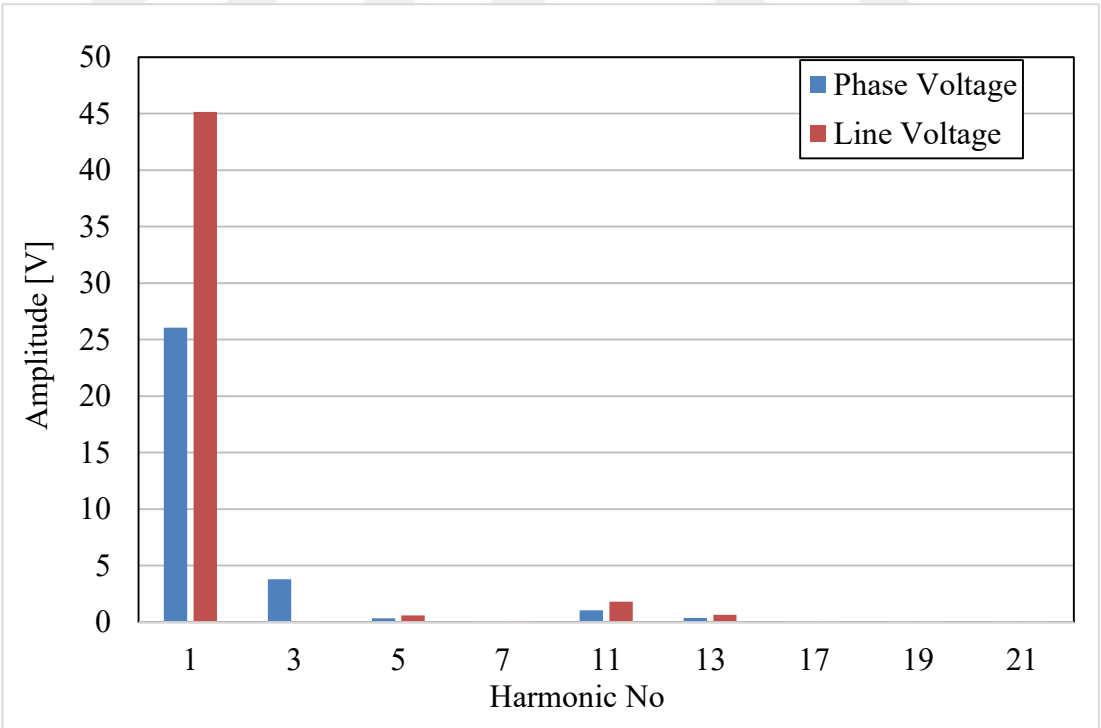

Figure 4.6: Harmonic spectrum of the final SPM motor design according to BEMF data obtained by 2D FEA.

4.1.1.2 On-load analysis

On-load analysis is done to obtain magnetic flux distribution considering the armature effect also to compute electromagnetic torque of machine. Here in Figure 4.7 and Figure 4.8 magnetic flux density and flux lines distributions are given. Again, maximum value is flux density is lower than 1.5 T and and a proper flux dines distribution is obtained. Although the flux distribution of the final SPM seems to be good, because of the slotting effect, space harmonics do exist in the motor as previosly shown in no load analysis part. This also has effect on output torque which is shown in Figure 4.9. There is 1.41 Nm difference between the maximum and the minimum points of the torque waveform which causes 7.68% torque ripple. This amount of torque ripple, cogging torque and THD is generally reduced by taking some precauitons such as choosing fractional slot number and skewing.

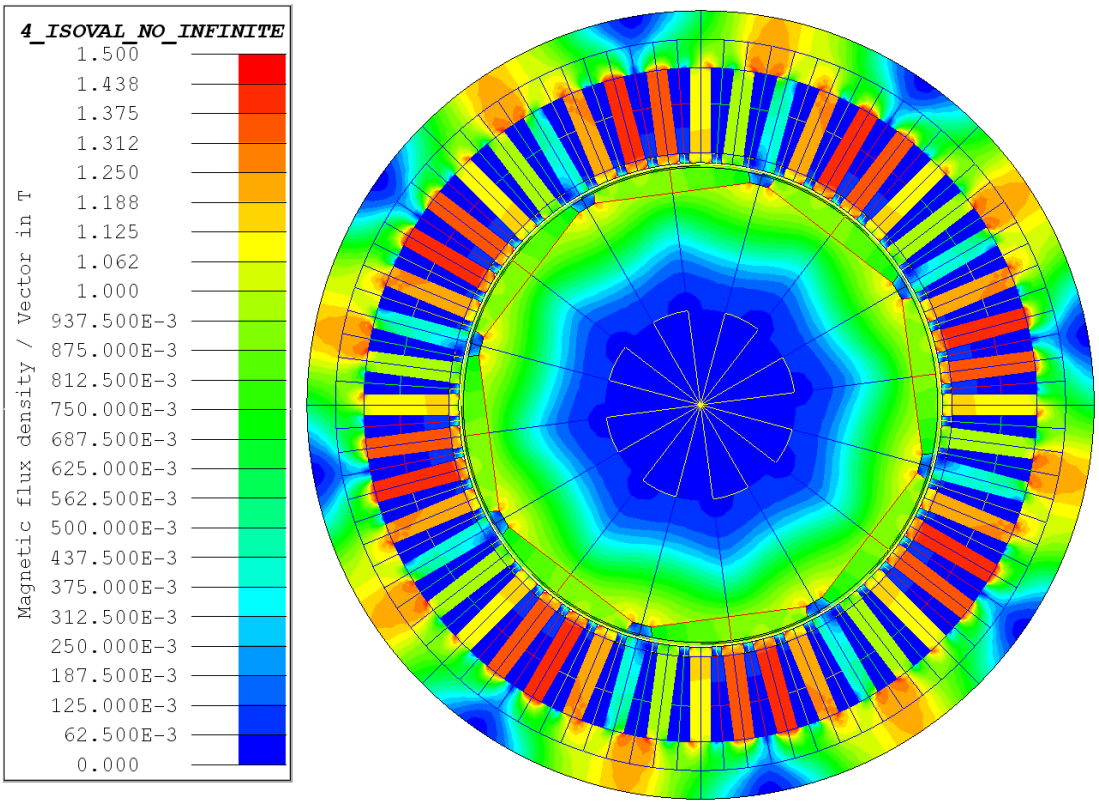

Figure 4.7: On-load flux density distribution of final SPM motor design obtained by 2D FEA.

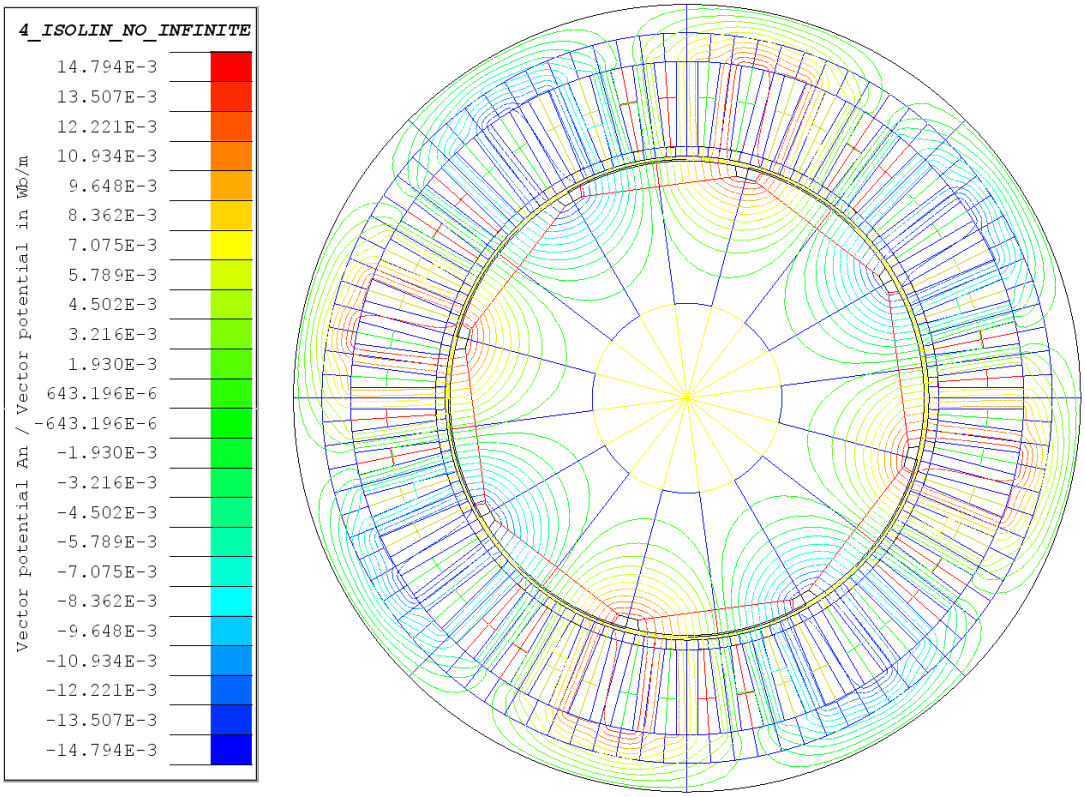

Figure 4.8: On-load magnetic flux lines distribution of the final SPM motor design obtained by 2D FEA.

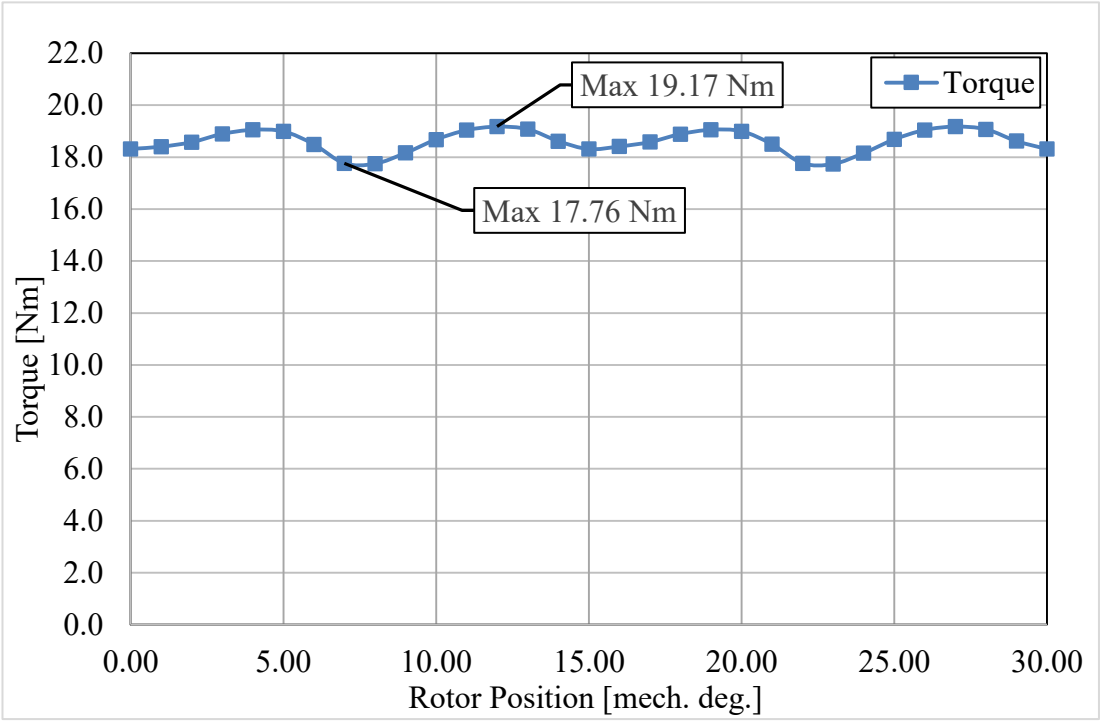

Figure 4.9: Output torque of the final SPM motor design obtained by 2D FEA.

4.2 IPM Motor Design

Since the SPM motor design is completed previously, it is now appropriate to move on with the IPM motor design. Magnet volume of the SPM motor will be kept constant in order to make a fair design comparison. Before moving on with the design, if a comment about V-type IPM motor is going to be made, it can be said that it is expected to obtain poor performance compared to SPM motor in terms of THD and torque ripple. The reason for this lies in the structure of IPM. Two magnet parts creating a pole will have leakage flux short circuting on themselves and unproper flux distriubtion is expected to be seen.

4.2.1 Detailed design with FLUX 2D

Since analtical methods does not work well in internal permanent magnet motors, IPM motor is designed directly by using finite element method. By taking magnet volume constant, IPM motor is designed. Optimisation is done by changing magnet V-angle and magnet length which is given in Figure 4.10.

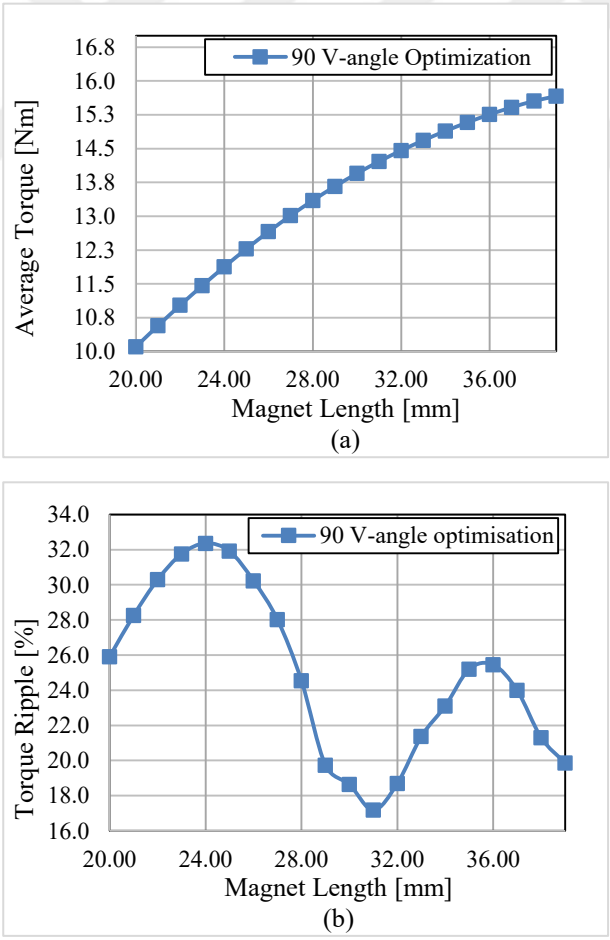

Figure 4.10: Effect of magnet length on output torque: (a) average torque, (b) torque ripple.

In Figure 4.10 magnet length is changed along with magnet width at 90° V-angle to investigate average torque and torque ripple. It is seen that the optimisation result is similar to that of SPM motor pole arc variation. Another optimisation result is presented in Figure 4.11, where magnet length is varied at 100° V-angle. When compared with previous figure it is seen that lower average torque is obtained with 100° V-angle, whereas torque ripple is slightly lower.

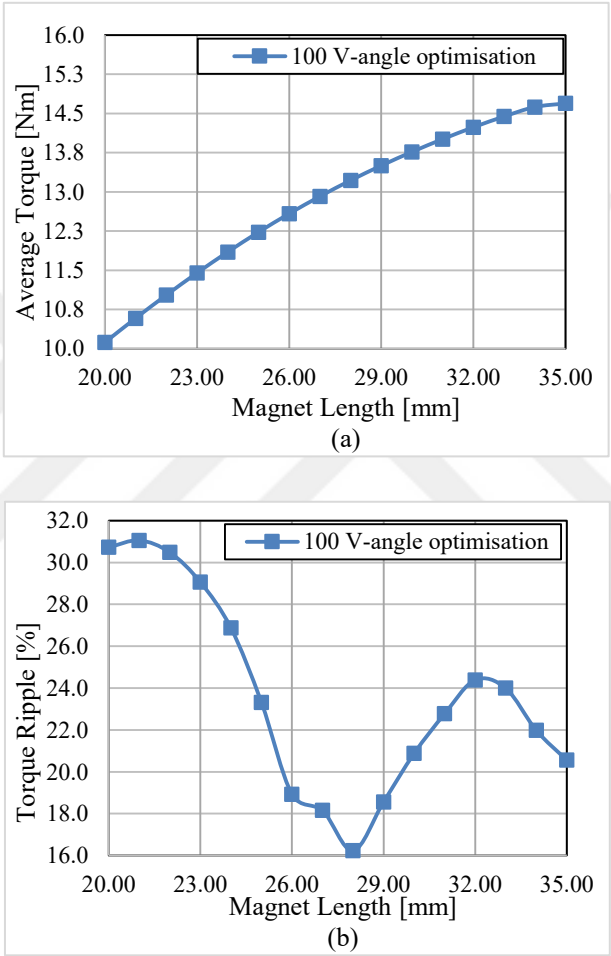

Figure 4.11: Effect of magnet length on output torque: (a) average torque, (b) torque ripple

In Figure 4.12 V-angle is varied between 30° and 97° for 36 mm magnet length where magnet width is 3.75 mm. Average torque and torque ripple graphs are obtained. It is seen that average torque value also dependent on the V-angle of the magnets along with magnet length. Torque ripple value goes up to 43% and down to 13.9%.

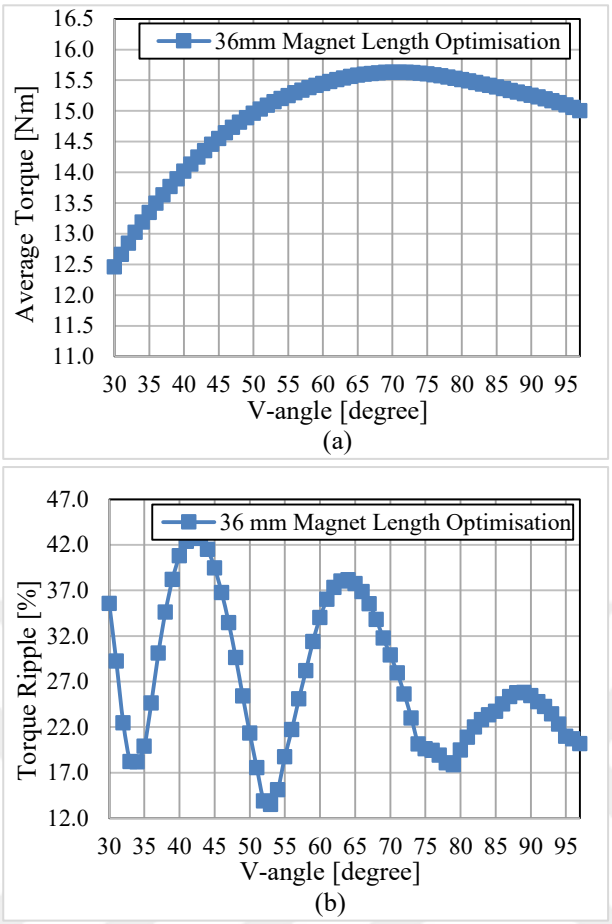

Figure 4.12: Effect of V-angle on output torque: (a) avereage torque, (b) torque ripple.

In Figure 4.13 V-angle is varied for 45mm magnet length where magnet width is 3mm. Highest average torque and lowest torque ripple values are obtained in that condition. At 63° V-angle, 17.1 Nm average torque and 19.74% torque ripple is reached by applying wide range optimization on IPM motor.

Although a lot of optimisations are done to obtain the best design, only a few are given since the main idea is the same for all: variations are applied and its effect on output torque characteristics are considered.

Other than magnet shape optimisation, length of the distance between the IPM magnets and length of the distance from the top point of the magnets to outer surface of the rotor are examined. These values are chose such that no mechanical limitation is not exceeded.

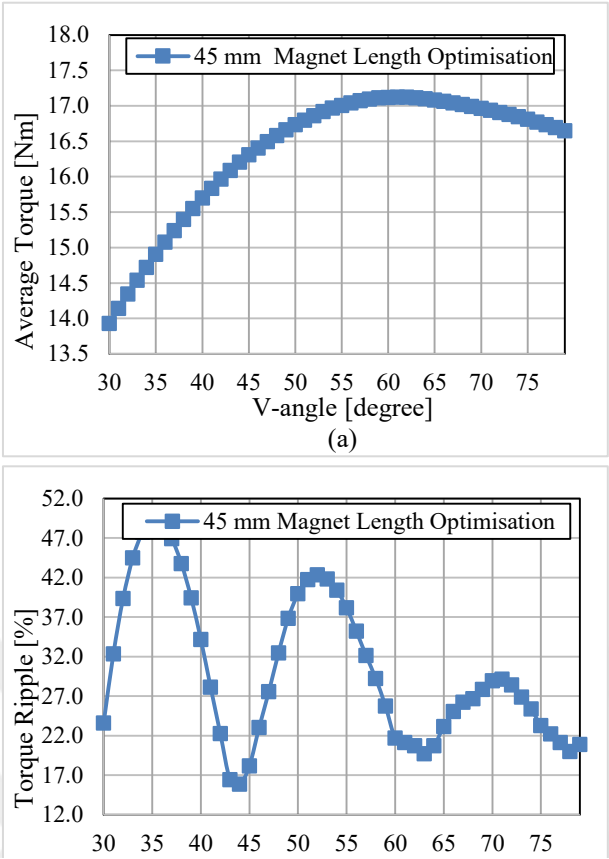

Figure 4.13: Effect of V-angle on output torque: (a) average torque, (b) torque ripple.

4.2.1.1 No-load analysis

No-load flux density distribution of the IPM motor is shown in Figure 4.14 where legend is limited to a maximum value of 1.5 T which is the maximum value in the motor except the upper parts of the magnet. Upper parts of the magnet exposed to short circuiting flux which causes saturation.

Cogging torque waveform is obtained and presented in Figure 4.14. Peak to peak value of the cogging torque is approximately 1.85 Nm which corresponds to 10.8% of average torque. This value is rather high for electric motors and not preferred as it causes vibration and noise. Slot pole combination is the number one cause of this amount and magnets being buried creates less proper flux distribution when compared to other magnet configurations.

In Figure 4.16 and Figure 4.17 induced voltage waveforms and corresponding harmonic spectrums are shown at 1000 rpm. Phase and line induced voltage waveforms are quite distorted. Phase THD value is 9.18% and line THD value is 5.67% which is very high.

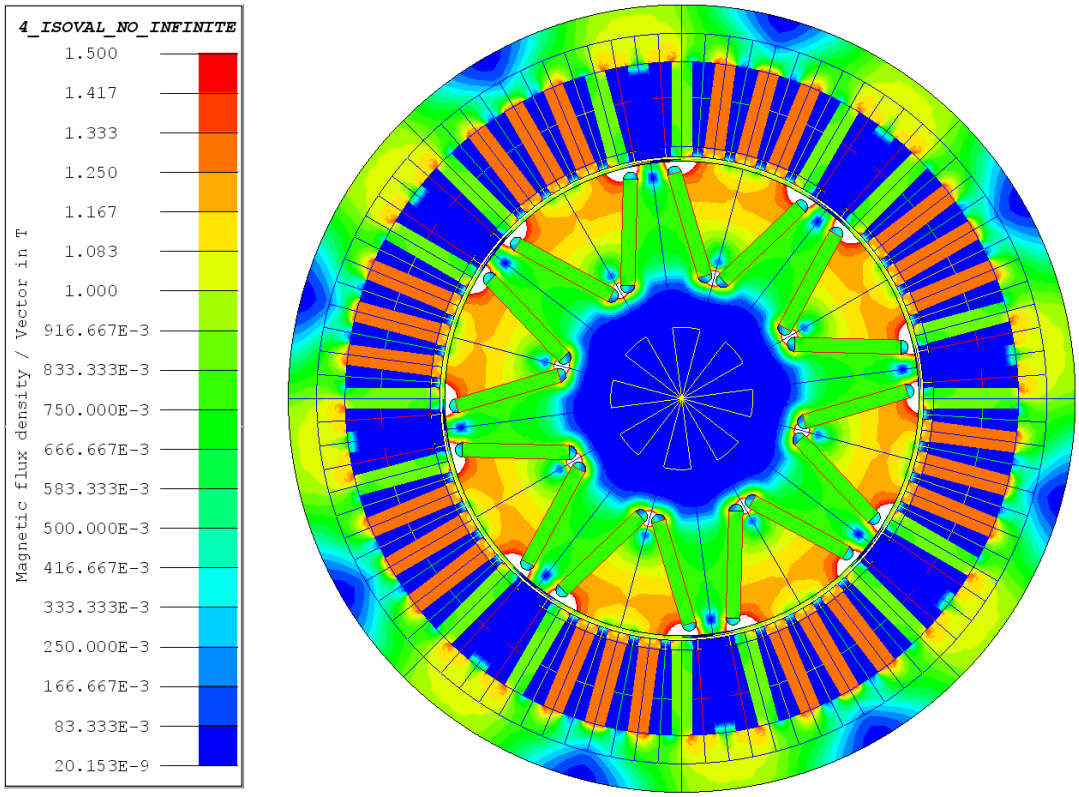

Figure 4.14: No-load flux density distribution of the final IPM motor design obtained by 2D FEA.

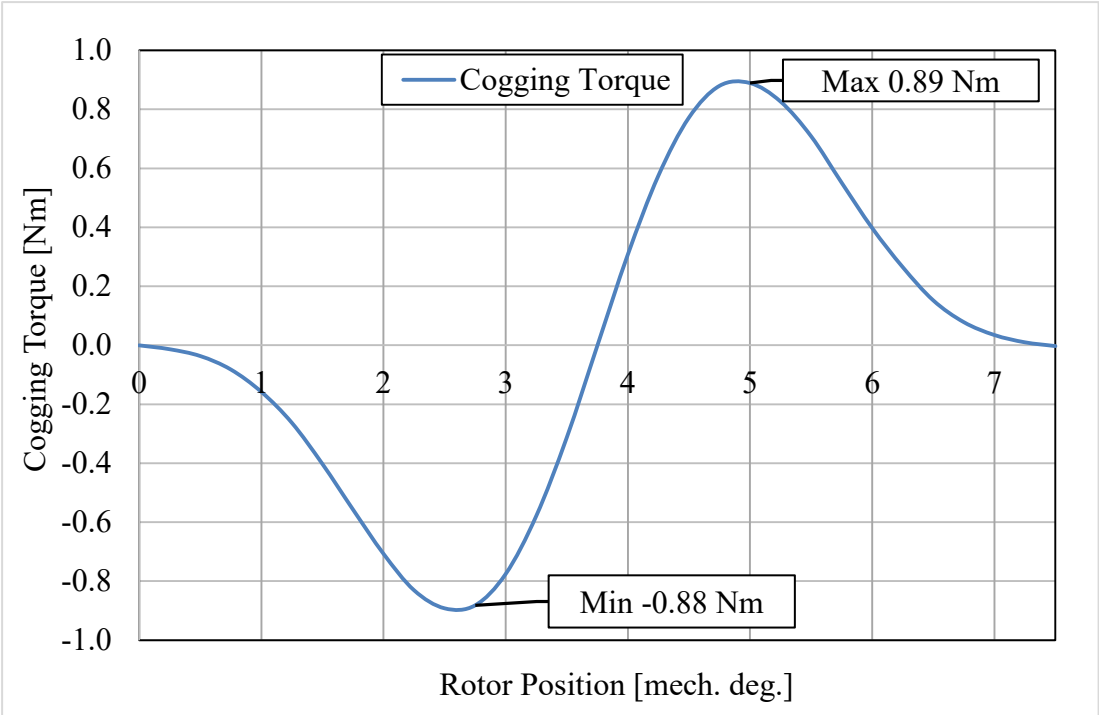

Figure 4.15: Cogging torque waveform of the final IPM motor design obtained by 2D FEA.

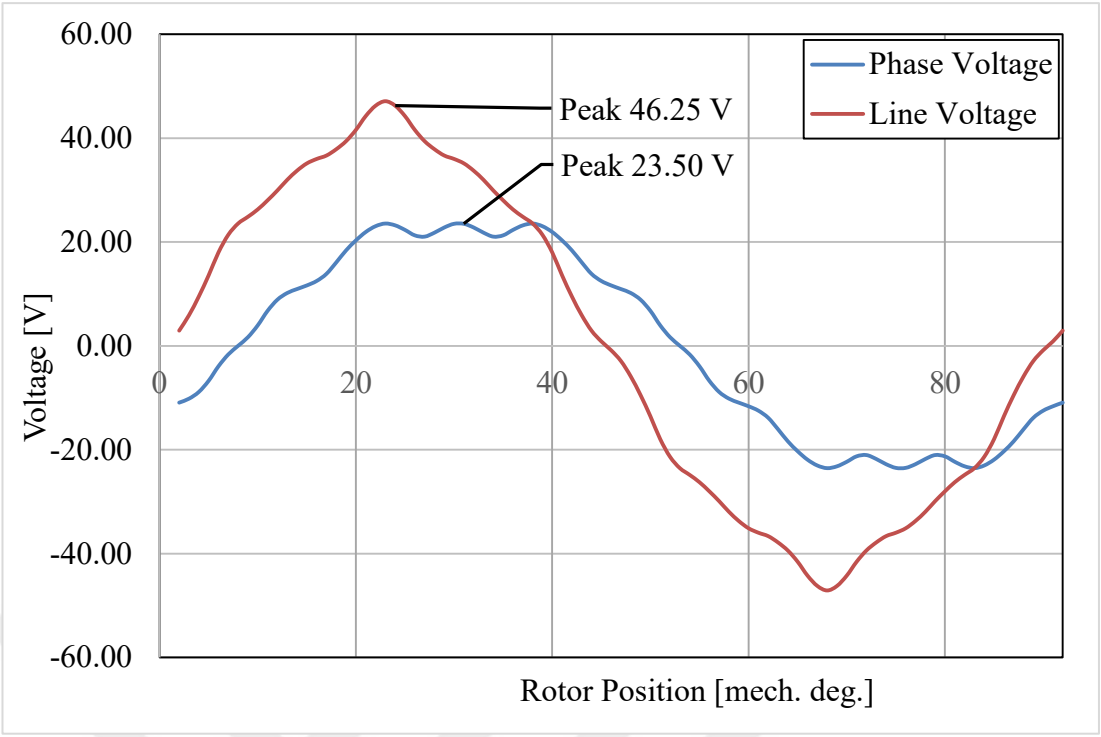

Figure 4.16: Induced voltage waveforms of the final IPM motor design obtained by 2D FEA.

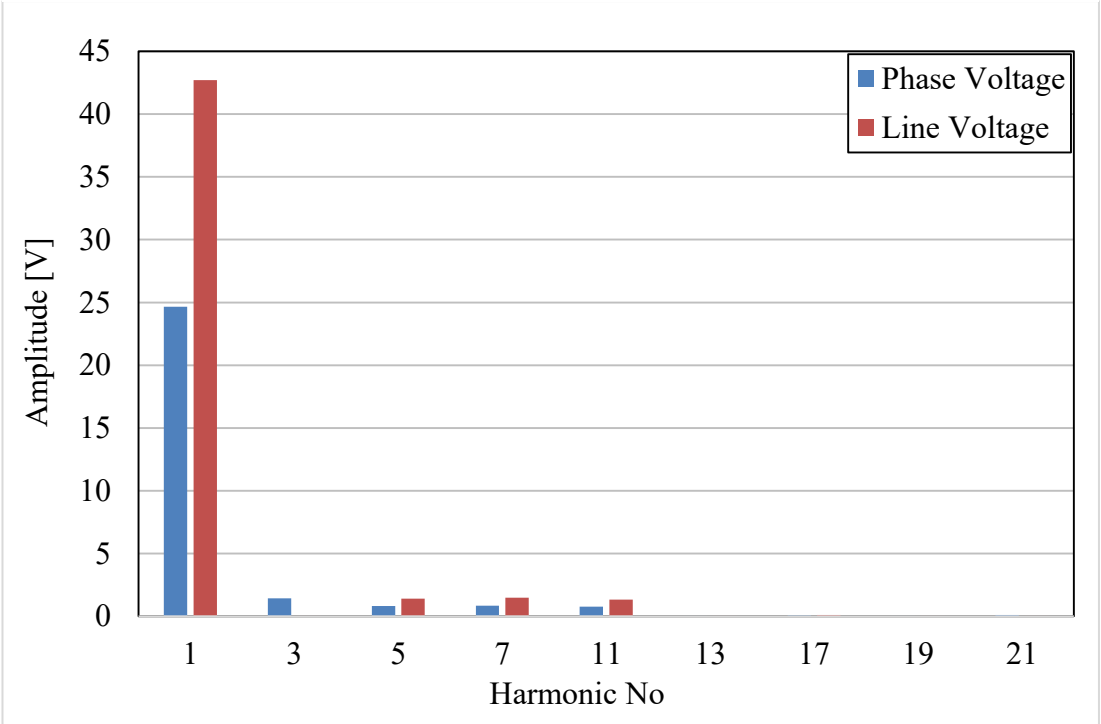

Figure 4.17: Harmonic spectrum of the final IPM motor design obtained by 2D FEA.

4.2.1.2 On load analysis

Flux density distributions and output torque waveforms are obtained at on-load analysis. Figure 4.18 shows the flux density distribution at rated load. Maximum value of 1.5 T is obtained throught the motor, near tooth tips. In Figure 4.20, flux lines distribution is given. Pole formations are proper and selectible in stator and rotor regions, however leakage flux between two magnets forming a pole and two consequent poles causes saturation in rotor region which is inevitable but increases THD and torque ripple. Determined by the optimisation, output torque of the final IPM design is presented in Figure 4.20. With high fluctuations, 19.74% torque ripple is obtained.

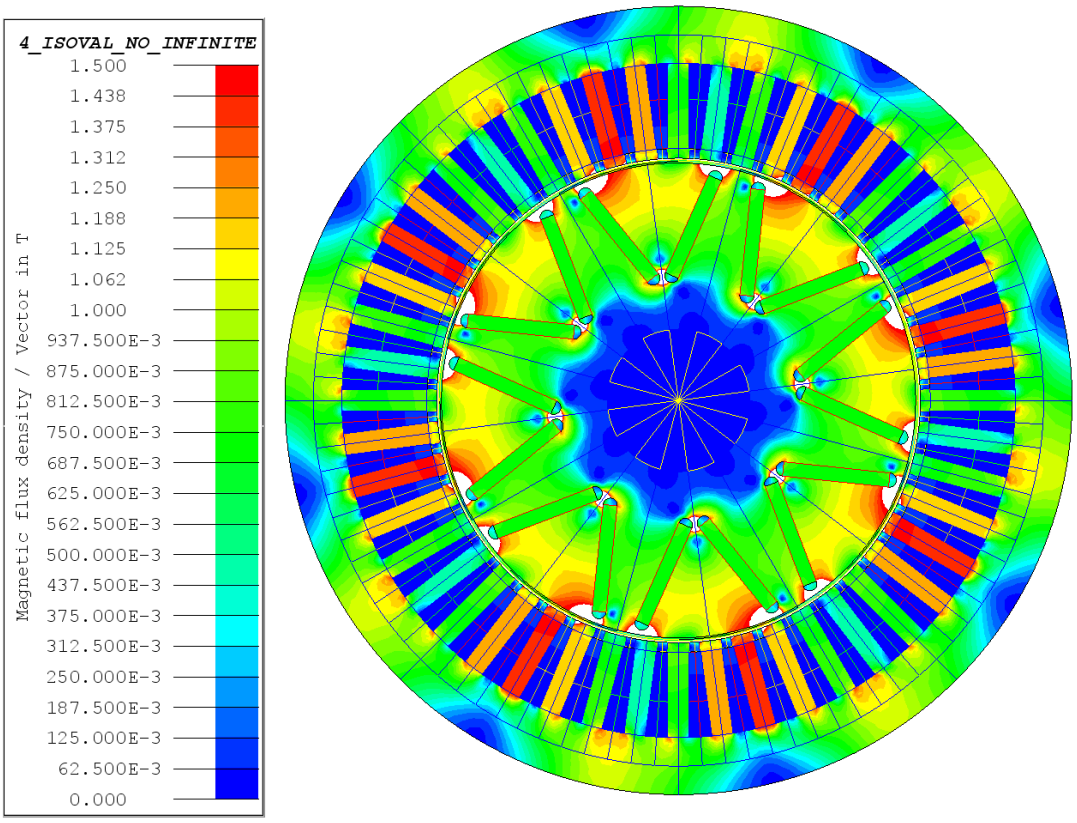

Figure 4.18: On-load flux density distribution of the final IPM motor design obtained by 2D FEA.

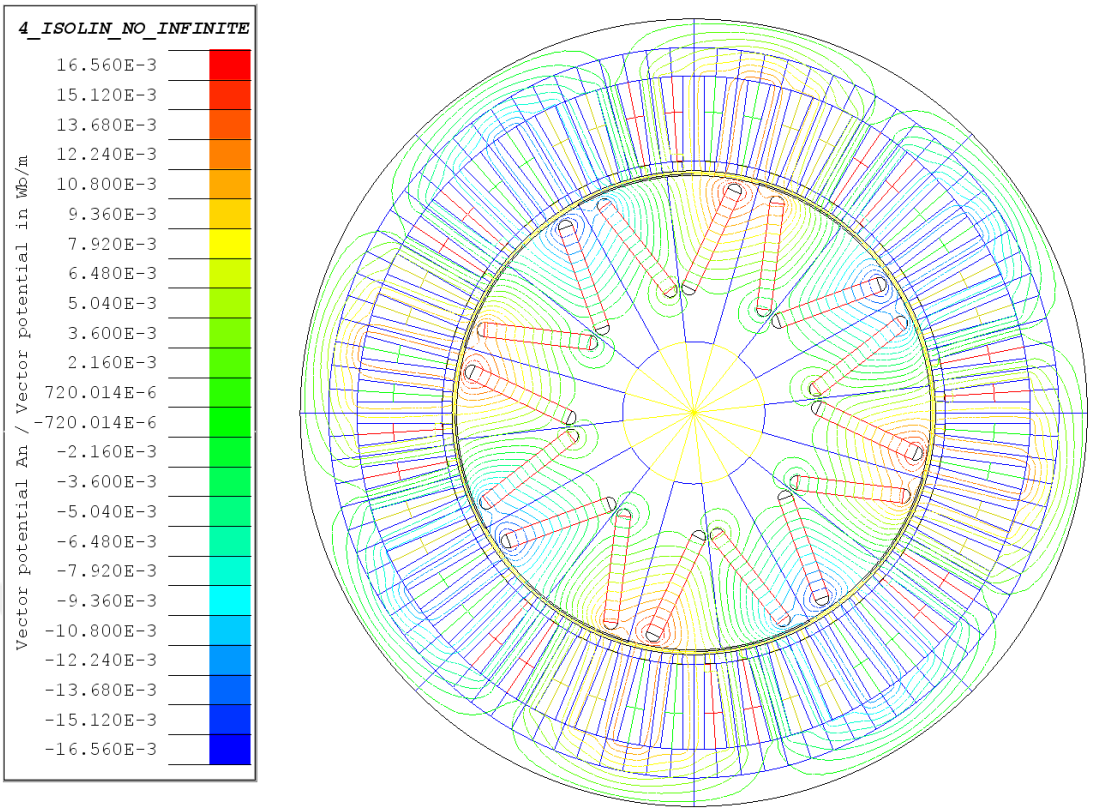

Figure 4.19: Output torque waveform of the final IPM motor deisgn obtained by 2D FEA.

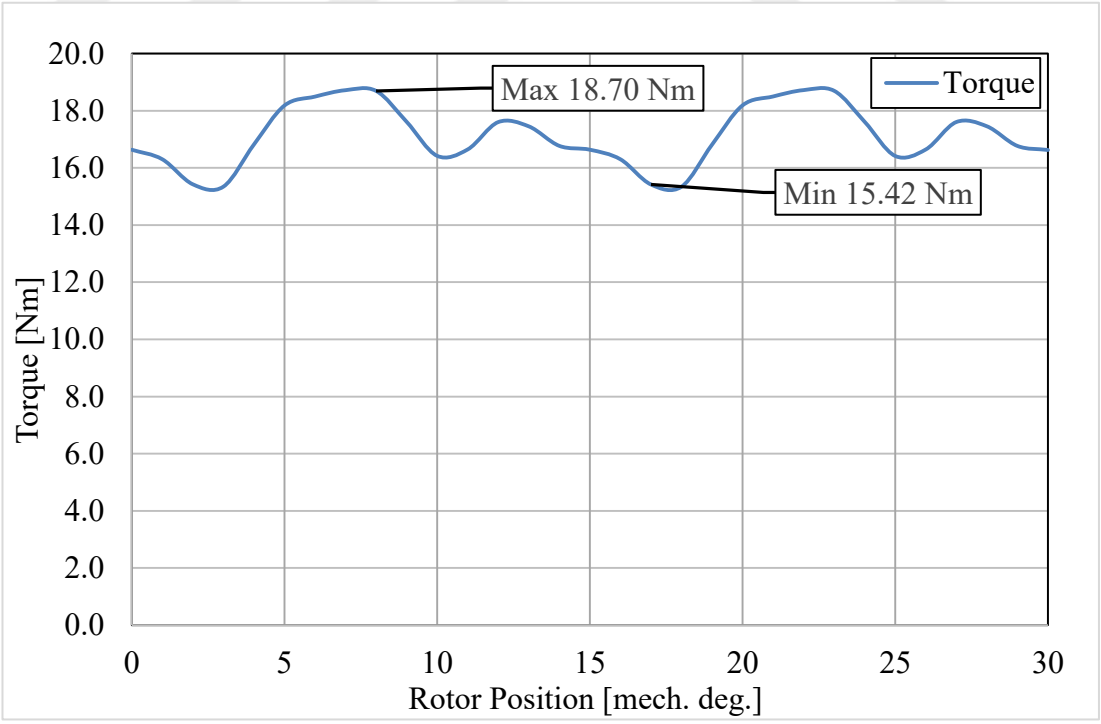

Figure 4.20: On-load flux lines distribution of the final IPM motor design obtained by 2D FEA.

4.3 Hybrid Motor Design

In order to design the hybrid rotor, formulations are applied to the rotor geometry in order to vary and optimise the motor in FLUX 2D. Special care has been taken for precise formulation as mesh and analysis depend on the geometry.

First optimization is done by varying magnet length between 35 and 45mm in 1mm steps and V-angle between 50º and 70º in 2º steps. This optimization is done for obtaining general insight about the motor characteristics. In Figure 4.21 scatter type visualization of optimization is given, where colouring is applied to the points according to the torque ripple.

In Figure 4.21 where general optimisation is done, general operating characteristics are obtained. It is seen that when the magnet length is 45 mm, average torque values are the highest. Generally in IPM motors, when magnet length is increased, flux leaving the magnet surface increases because the magnet surface increases. When compared, magnet width does not cause an in increase in flux as much as magnet length does. This effect can also be seen in the figure, as magnet width and length are changed together to get the same magnet volume. When the magnet length is between 35 and 40mm, lowest torque ripple designs are obtained. By giving the maximum average torque and minimum torque ripple design points, first optimisation can be followed by more detailed analysis.

Since the highest average torque designs are known, pole arc of SPMs and V-angle of IPMs can be further analysed for 45 mm magnet length. V-angle is varied between 50º and 70º in 2º steps and pole arc is varied from 42.5º to 38.2º in 0.25º making 231 analysis in total. The result is given in table form in Table 4.3 and Table 4.4. Average torque varies between a maximum value of 18.04 Nm and a minimum value of 17.6 Nm whereas torque ripple varies between 7.18% and 23%. Maximum average torque point is obtained at 60º V-angle and 40.61º pole arc and minimum torque ripple point is obtained at 58º V-angle and 42.54º pole arc. It is seen that at 45 mm magnet length average torque is high, and angle between magnets do not have a devastating effect on average torque but torque ripple.

In order to do detailed analysis near the design points where torque ripple is minimum in the first optimisation, magnet length is varied between 35 and 40 mm, V-angle is varied in 50-56º in 1º steps and pole arc is varied between 42.54º and 38.2º in 0.45º steps making 462 analysis in total.

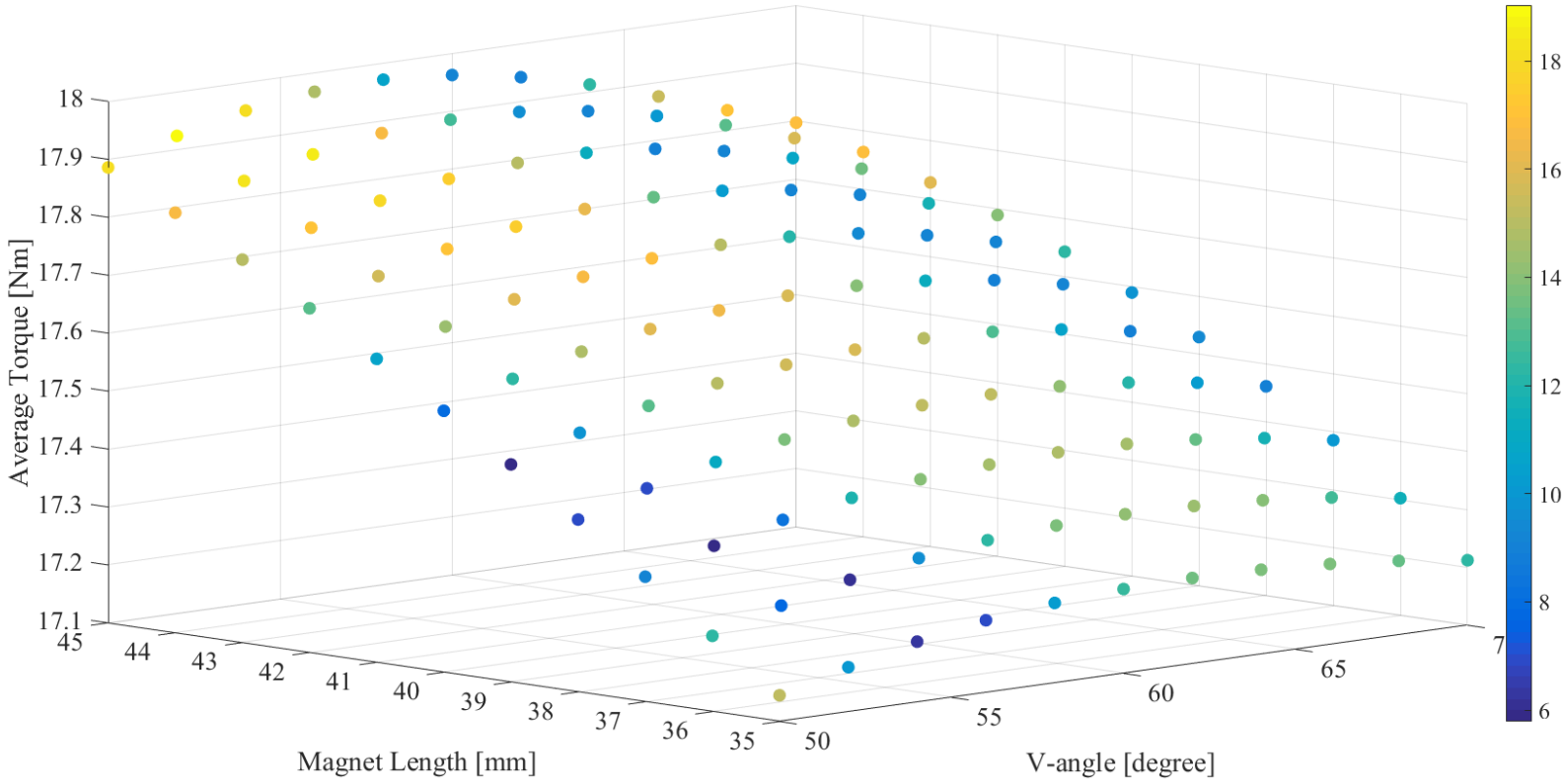

Figure 4.21: Magnet length and V-angle optimization of hybrid motor obtained by 2D FEA.

Table 4.3: V-angle and pole arc optimisation (part 1) at 45mm magnet length obtained by 2D FEA.

		Pole Arc [mech. deg.]										
V-angle [degree]		40.37	40.16	39.95	39.76	39.56	39.37	39.17	38.94	38.70	38.47	38.23
50.00	Average Torque [Nm]	17.89	17.87	17.86	17.84	17.82	17.80	17.77	17.76	17.74	17.72	17.68
	Torque Ripple [%]	18.10	17.73	17.41	17.10	16.81	16.52	16.29	16.04	15.82	15.65	15.49
52.00	Average Torque [Nm]	17.92	17.91	17.90	17.88	17.86	17.84	17.81	17.80	17.78	17.76	17.72
	Torque Ripple [%]	19.03	18.74	18.45	18.20	17.96	17.73	17.54	17.34	17.18	17.04	16.91
54.00	Average Torque [Nm]	17.95	17.94	17.93	17.91	17.88	17.87	17.84	17.83	17.81	17.78	17.75
	Torque Ripple [%]	18.15	17.86	17.56	17.30	17.05	16.82	16.62	16.42	16.25	16.11	15.97
56.00	Average Torque [Nm]	17.97	17.95	17.94	17.92	17.90	17.88	17.85	17.84	17.82	17.80	17.76
	Torque Ripple [%]	14.82	14.52	14.21	13.94	13.68	13.44	13.22	13.02	12.84	12.68	12.54
58.00	Average Torque [Nm]	17.97	17.96	17.95	17.93	17.90	17.89	17.86	17.85	17.83	17.80	17.77
	Torque Ripple [%]	10.71	10.45	10.16	9.84	9.49	9.15	8.80	8.46	8.13	7.86	7.60
60.00	Average Torque [Nm]	17.96	17.95	17.94	17.92	17.90	17.88	17.85	17.84	17.82	17.80	17.76
	Torque Ripple [%]	9.27	9.09	8.88	8.62	8.34	8.08	7.81	7.53	7.28	7.19	7.32
62.00	Average Torque [Nm]	17.94	17.93	17.92	17.90	17.88	17.86	17.83	17.82	17.80	17.77	17.74
	Torque Ripple [%]	8.91	8.73	8.86	8.95	9.03	9.13	9.22	9.32	9.58	9.93	10.28
64.00	Average Torque [Nm]	17.91	17.90	17.89	17.87	17.85	17.83	17.80	17.79	17.77	17.75	17.71
	Torque Ripple [%]	12.29	12.39	12.75	13.13	13.48	13.83	14.15	14.44	14.72	14.99	15.23
66.00	Average Torque [Nm]	17.88	17.86	17.85	17.83	17.81	17.79	17.76	17.75	17.73	17.71	17.68
	Torque Ripple [%]	15.48	15.91	16.34	16.72	17.08	17.43	17.76	18.05	18.34	18.62	18.87
68.00	Average Torque [Nm]	17.84	17.82	17.81	17.79	17.77	17.75	17.72	17.71	17.69	17.67	17.64
	Torque Ripple [%]	17.00	17.43	17.87	18.26	18.63	18.98	19.32	19.61	19.90	20.18	20.50
70.00	Average Torque [Nm]	17.80	17.78	17.77	17.75	17.73	17.71	17.69	17.68	17.66	17.63	17.60
	Torque Ripple [%]	16.82	17.24	17.67	18.09	18.48	18.87	19.23	19.56	20.14	20.74	21.30

Table 4.4: V-angle and pole arc optimisation (part 2) at 45mm magnet length obtained by 2D FEA.

		Pole Arc [mech. deg.]									
V-angle [degree]		42.54	42.33	42.12	41.91	41.70	41.50	41.30	41.07	40.84	40.61
50.00	Average Torque [Nm]	18.04	18.04	18.02	18.01	17.99	17.98	17.96	17.95	17.93	17.90
	Torque Ripple [%]	22.26	22.00	21.71	21.39	21.02	20.60	20.16	19.67	19.16	18.62
52.00	Average Torque [Nm]	18.08	18.08	18.06	18.04	18.03	18.02	17.99	17.99	17.97	17.94
	Torque Ripple [%]	23.09	22.67	22.18	21.68	21.20	20.79	20.35	19.93	19.59	19.32
54.00	Average Torque [Nm]	18.10	18.10	18.08	18.07	18.05	18.05	18.02	18.01	18.00	17.97
	Torque Ripple [%]	21.98	21.54	21.13	20.75	20.34	19.93	19.49	19.08	18.76	18.45
56.00	Average Torque [Nm]	18.12	18.12	18.10	18.08	18.07	18.06	18.04	18.03	18.01	17.98
	Torque Ripple [%]	19.31	18.88	18.39	17.91	17.51	17.08	16.63	16.16	15.68	15.17
58.00	Average Torque [Nm]	18.12	18.12	18.10	18.09	18.07	18.07	18.04	18.03	18.02	17.99
	Torque Ripple [%]	15.47	15.07	14.61	14.13	13.67	13.19	12.68	12.16	11.62	11.04
60.00	Average Torque [Nm]	18.11	18.11	18.09	18.08	18.06	18.06	18.03	18.02	18.01	17.98
	Torque Ripple [%]	11.94	11.54	11.29	11.08	10.82	10.54	10.18	9.80	9.67	9.48
62.00	Average Torque [Nm]	18.09	18.09	18.07	18.06	18.04	18.04	18.01	18.00	17.99	17.96
	Torque Ripple [%]	10.79	10.69	10.59	10.44	10.28	10.11	9.88	9.65	9.40	9.12
64.00	Average Torque [Nm]	18.06	18.06	18.04	18.03	18.01	18.01	17.98	17.97	17.96	17.93
	Torque Ripple [%]	11.14	11.30	11.46	11.58	11.68	11.83	11.91	12.02	12.11	12.21
66.00	Average Torque [Nm]	18.03	18.02	18.01	17.99	17.97	17.97	17.94	17.94	17.92	17.89
	Torque Ripple [%]	13.20	13.35	13.52	13.64	13.75	13.89	13.98	14.10	14.58	15.04
68.00	Average Torque [Nm]	17.98	17.98	17.97	17.95	17.93	17.93	17.90	17.90	17.88	17.85
	Torque Ripple [%]	13.45	13.59	13.75	13.87	14.12	14.62	15.11	15.60	16.08	16.55
70.00	Average Torque [Nm]	17.94	17.94	17.92	17.91	17.89	17.89	17.86	17.86	17.84	17.81
	Torque Ripple [%]	13.33	13.55	13.81	14.10	14.42	14.78	15.17	15.56	15.97	16.39

Table 4.5: V-angle and pole-arc optimisation results for different magnet lengths: (a) 35mm, (b) 36mm, (c) 37 mm, (d) 38 mm, (e) 39 mm.

(a)

		Pole Arc [mech. deg.]										
V-angle [degree]		42.54	42.12	41.7	41.3	40.84	40.37	39.95	39.56	39.17	38.7	38.23
50	Average Torque [Nm]	17.31	17.29	17.26	17.22	17.20	17.14	17.12	17.08	17.03	17.00	16.93
	Torque Ripple [%]	12.53	12.95	13.30	13.82	14.55	15.30	16.01	16.63	17.18	17.62	17.97
51	Average Torque [Nm]	17.32	17.31	17.27	17.24	17.21	17.16	17.14	17.09	17.04	17.02	16.95
	Torque Ripple [%]	10.66	11.08	11.41	11.69	12.01	12.75	13.46	14.08	14.63	15.06	15.54
52	Average Torque [Nm]	17.34	17.32	17.29	17.25	17.23	17.18	17.15	17.11	17.06	17.04	16.97
	Torque Ripple [%]	8.74	9.15	9.48	9.75	9.96	10.08	10.79	11.40	12.06	12.61	13.15
53	Average Torque [Nm]	17.35	17.34	17.30	17.27	17.24	17.19	17.17	17.12	17.07	17.05	16.98
	Torque Ripple [%]	8.28	8.09	7.66	7.80	8.00	8.12	8.34	8.92	9.60	10.16	10.68
54	Average Torque [Nm]	17.36	17.35	17.31	17.28	17.26	17.20	17.18	17.14	17.09	17.06	17.00
	Torque Ripple [%]	9.21	8.57	8.15	7.52	6.69	6.38	6.66	6.86	7.10	7.65	8.17
55	Average Torque [Nm]	17.37	17.36	17.32	17.29	17.27	17.22	17.19	17.15	17.10	17.07	17.01
	Torque Ripple [%]	10.41	9.58	8.63	7.96	7.13	6.11	5.01	5.15	5.32	5.51	5.74
56	Average Torque [Nm]	17.38	17.37	17.33	17.30	17.28	17.22	17.20	17.16	17.11	17.08	17.02
	Torque Ripple [%]	12.24	11.56	10.69	9.63	8.34	6.89	5.56	4.28	3.60	3.79	4.00

(b)

		Pole Arc [mech. deg.]										
V-angle [degree]		42.54	42.12	41.7	41.3	40.84	40.37	39.95	39.56	39.17	38.7	38.23
50	Average Torque [Nm]	17.39	17.38	17.34	17.31	17.28	17.23	17.21	17.16	17.11	17.09	17.02
	Torque Ripple [%]	10.31	10.73	11.07	11.34	11.60	12.34	13.05	13.68	14.24	14.80	15.36
51	Average Torque [Nm]	17.41	17.39	17.36	17.32	17.30	17.25	17.23	17.18	17.13	17.11	17.04
	Torque Ripple [%]	8.25	8.67	9.00	9.27	9.48	9.60	10.17	10.95	11.65	12.22	12.77
52	Average Torque [Nm]	17.43	17.41	17.38	17.34	17.32	17.27	17.24	17.20	17.15	17.12	17.06
	Torque Ripple [%]	8.31	8.10	7.67	7.18	7.39	7.66	7.95	8.32	9.00	9.56	10.10
53	Average Torque [Nm]	17.35	17.34	17.30	17.27	17.24	17.19	17.17	17.12	17.07	17.05	16.98
	Torque Ripple [%]	8.28	8.09	7.66	7.80	8.00	8.12	8.34	8.92	9.60	10.16	10.68
54	Average Torque [Nm]	17.45	17.44	17.40	17.37	17.35	17.29	17.27	17.23	17.18	17.15	17.09
	Torque Ripple [%]	10.92	10.22	9.37	8.30	7.20	6.18	5.08	4.54	4.72	4.91	5.13
55	Average Torque [Nm]	17.46	17.45	17.41	17.38	17.36	17.31	17.28	17.24	17.19	17.16	17.10
	Torque Ripple [%]	13.04	12.33	11.47	10.43	9.14	7.69	6.13	4.65	3.33	3.24	3.52
56	Average Torque [Nm]	17.47	17.45	17.42	17.39	17.37	17.32	17.29	17.25	17.20	17.18	17.11
	Torque Ripple [%]	14.89	14.21	13.34	12.28	10.99	9.55	7.99	6.37	5.01	3.95	3.44

(c)

		Pole Arc [mech. deg.]										
V-angle [degree]		42.54	42.12	41.7	41.3	40.84	40.37	39.95	39.56	39.17	38.7	38.23
50	Average Torque [Nm]	17.47	17.46	17.43	17.39	17.37	17.32	17.29	17.25	17.20	17.17	17.10
	Torque Ripple [%]	7.83	8.25	8.57	8.85	9.06	9.20	9.80	10.58	11.28	11.86	12.41
51	Average Torque [Nm]	17.49	17.48	17.44	17.41	17.39	17.34	17.31	17.27	17.22	17.19	17.13
	Torque Ripple [%]	8.33	8.12	7.70	7.06	6.97	7.31	7.60	7.82	8.45	9.02	9.55
52	Average Torque [Nm]	17.51	17.49	17.46	17.43	17.40	17.35	17.33	17.28	17.24	17.21	17.14
	Torque Ripple [%]	9.66	8.81	8.26	7.64	6.81	5.79	5.69	5.90	6.09	6.28	6.69
53	Average Torque [Nm]	17.52	17.51	17.48	17.44	17.42	17.37	17.34	17.30	17.25	17.23	17.16
	Torque Ripple [%]	11.60	10.92	10.05	9.00	7.71	6.28	5.19	4.03	4.16	4.35	4.58
54	Average Torque [Nm]	17.54	17.52	17.49	17.45	17.43	17.38	17.36	17.31	17.26	17.24	17.18
	Torque Ripple [%]	13.76	13.10	12.24	11.19	9.90	8.45	6.89	5.27	4.09	3.24	3.51
55	Average Torque [Nm]	17.55	17.53	17.50	17.47	17.44	17.39	17.37	17.33	17.28	17.25	17.19
	Torque Ripple [%]	15.66	14.96	14.12	13.07	11.78	10.34	8.77	7.15	5.79	4.74	4.47
56	Average Torque [Nm]	17.56	17.54	17.51	17.47	17.45	17.40	17.38	17.34	17.29	17.26	17.20
	Torque Ripple [%]	17.17	16.52	15.66	14.61	13.32	11.88	10.32	8.69	7.15	6.45	6.23

(d)

		Pole Arc [mech. deg.]										
V-angle [degree]		42.54	42.12	41.7	41.3	40.84	40.37	39.95	39.56	39.17	38.7	38.23
50	Average Torque [Nm]	17.56	17.54	17.51	17.47	17.45	17.40	17.37	17.33	17.28	17.25	17.19
	Torque Ripple [%]	8.33	8.12	7.71	7.08	6.67	7.01	7.31	7.53	7.99	8.56	9.09
51	Average Torque [Nm]	17.57	17.56	17.53	17.49	17.47	17.42	17.39	17.35	17.30	17.27	17.21
	Torque Ripple [%]	9.85	9.02	8.31	7.69	6.87	5.87	5.28	5.50	5.70	5.90	6.13
52	Average Torque [Nm]	17.59	17.58	17.54	17.51	17.48	17.43	17.41	17.37	17.32	17.29	17.23
	Torque Ripple [%]	12.20	11.52	10.66	9.62	8.33	6.89	5.32	4.14	3.65	3.85	4.08
53	Average Torque [Nm]	17.61	17.59	17.56	17.52	17.50	17.45	17.43	17.38	17.33	17.31	17.25
	Torque Ripple [%]	14.44	13.77	12.92	11.87	10.59	9.15	7.58	5.96	4.81	3.75	3.50
54	Average Torque [Nm]	17.62	17.60	17.57	17.54	17.51	17.46	17.44	17.40	17.35	17.32	17.26
	Torque Ripple [%]	16.35	15.65	14.83	13.78	12.50	11.06	9.50	7.87	6.53	5.59	5.39
55	Average Torque [Nm]	17.63	17.61	17.58	17.55	17.53	17.48	17.45	17.41	17.36	17.33	17.27
	Torque Ripple [%]	17.84	17.20	16.35	15.31	14.03	12.59	11.02	9.40	7.87	7.37	7.16
56	Average Torque [Nm]	17.64	17.62	17.59	17.56	17.53	17.49	17.46	17.42	17.37	17.35	17.28
	Torque Ripple [%]	18.96	18.33	17.46	16.44	15.16	13.71	12.15	10.52	9.40	8.98	8.71

Table 4.6: V-angle and pole-arc optimisation results for different magnet lengths: (a) 39 mm and (b) 40 mm.

(a)

		Pole Arc [mech. deg.]										
V-angle [degree]		42.54	42.12	41.7	41.3	40.84	40.37	39.95	39.56	39.17	38.7	38.23
50	Average Torque [Nm]	17.63	17.62	17.58	17.55	17.53	17.48	17.45	17.41	17.36	17.33	17.27
	Torque Ripple [%]	10.07	9.40	8.54	7.74	6.93	5.92	4.94	5.17	5.36	5.57	5.81
51	Average Torque [Nm]	17.65	17.64	17.60	17.57	17.55	17.50	17.47	17.43	17.38	17.35	17.29
	Torque Ripple [%]	12.71	12.04	11.19	10.15	8.87	7.42	5.86	4.43	3.43	3.59	3.87
52	Average Torque [Nm]	17.67	17.65	17.62	17.59	17.56	17.51	17.49	17.45	17.40	17.37	17.31
	Torque Ripple [%]	15.01	14.36	13.49	12.47	11.18	9.76	8.18	6.58	5.45	4.38	4.01
53	Average Torque [Nm]	17.68	17.67	17.64	17.60	17.58	17.53	17.51	17.46	17.41	17.39	17.32
	Torque Ripple [%]	16.97	16.27	15.43	14.39	13.14	11.70	10.14	8.52	7.19	6.43	6.21
54	Average Torque [Nm]	17.70	17.68	17.65	17.62	17.59	17.54	17.52	17.48	17.43	17.40	17.34
	Torque Ripple [%]	18.48	17.79	16.97	15.93	14.66	13.22	11.65	10.03	8.58	8.20	7.99
55	Average Torque [Nm]	17.71	17.69	17.66	17.63	17.60	17.56	17.53	17.49	17.44	17.41	17.35
	Torque Ripple [%]	19.54	18.86	18.05	17.02	15.74	14.30	12.74	11.14	10.48	10.06	9.79
56	Average Torque [Nm]	17.72	17.70	17.67	17.64	17.61	17.57	17.54	17.50	17.45	17.43	17.36
	Torque Ripple [%]	20.16	19.54	18.70	17.66	16.39	14.96	13.42	12.44	11.96	11.52	11.26

(b)

		Pole Arc [mech. deg.]										
V-angle [degree]		42.54	42.12	41.7	41.3	40.84	40.37	39.95	39.56	39.17	38.7	38.23
50	Average Torque [Nm]	17.71	17.69	17.66	17.62	17.60	17.55	17.53	17.48	17.43	17.41	17.35
	Torque Ripple [%]	13.11	12.47	11.60	10.58	9.31	7.87	6.31	4.91	3.80	3.64	3.91
51	Average Torque [Nm]	17.73	17.71	17.68	17.64	17.62	17.57	17.55	17.50	17.46	17.43	17.37
	Torque Ripple [%]	15.54	14.87	14.03	12.99	11.72	10.28	8.72	7.12	6.01	4.93	4.68
52	Average Torque [Nm]	17.74	17.73	17.70	17.66	17.64	17.59	17.57	17.52	17.47	17.45	17.38
	Torque Ripple [%]	17.51	16.85	16.00	14.97	13.70	12.27	10.70	9.08	7.78	7.18	6.94
53	Average Torque [Nm]	17.76	17.74	17.71	17.68	17.65	17.61	17.58	17.54	17.49	17.46	17.40
	Torque Ripple [%]	18.98	18.36	17.52	16.48	15.22	13.78	12.22	10.60	9.51	9.08	8.79
54	Average Torque [Nm]	17.77	17.76	17.73	17.69	17.67	17.62	17.60	17.55	17.50	17.48	17.42
	Torque Ripple [%]	20.04	19.36	18.53	17.52	16.26	14.83	13.26	11.95	11.45	11.02	10.74
55	Average Torque [Nm]	17.78	17.77	17.74	17.70	17.68	17.63	17.61	17.57	17.52	17.49	17.43
	Torque Ripple [%]	20.61	19.96	19.13	18.10	16.83	15.41	14.15	13.38	12.88	12.46	12.16
56	Average Torque [Nm]	17.80	17.78	17.75	17.71	17.69	17.64	17.62	17.58	17.53	17.50	17.44
	Torque Ripple [%]	20.72	20.11	19.28	18.25	17.02	15.93	14.87	14.30	13.80	13.36	13.12

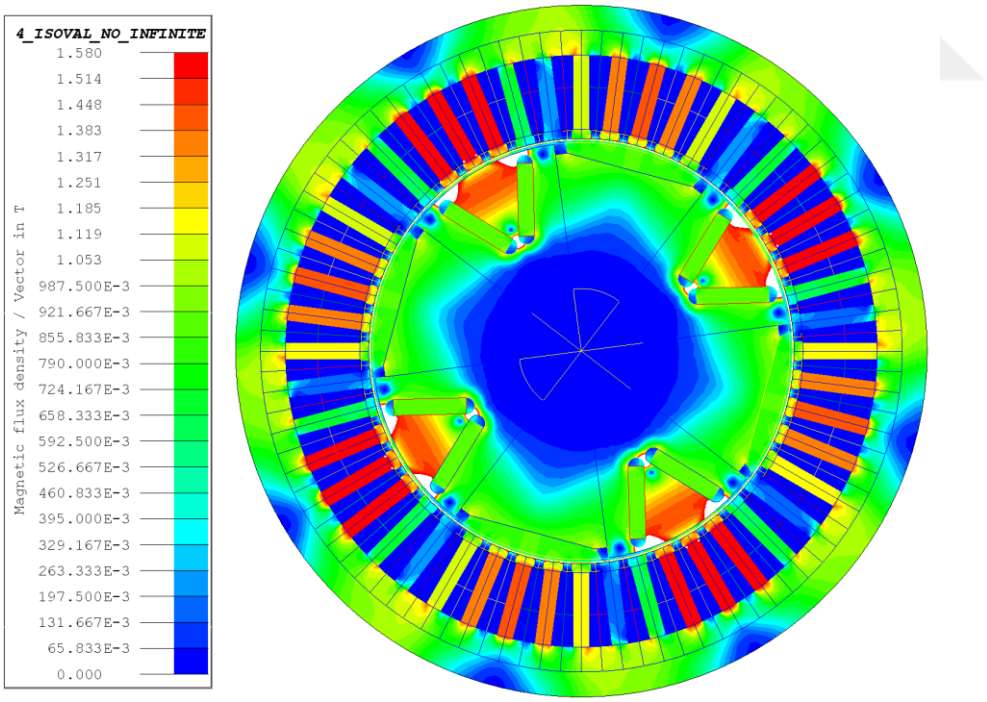

Figure 4.22: No-load flux density of the final hybrid motor design obtained by 2D FEA.

Results of optimisations are given in Table 4.5 and Table 4.6. When magnet length goes towards 40mm, average torque increases as expected, torque ripple also increases. On the other hand, 35mm magnet length design has the lowest torque ripple designs at 56° V-angle.

To further detail and narrow the optimisation, 38.9°, 38.4° and 38° pole arc values are also analyzed at 57° V-angle and 35mm magnet length. At 38.4° pole arc 17.07 Nm average torque and 3% torque ripple is obtained. Since the aim was to find best torque ripple design, this geometric parameters are determined as the final design parameters.

4.3.1 No load analysis

Figure 4.22 shows the no load flux density distribution where maximum flux density is 1.58 T. In Figure 4.23 cogging torque waveform is shown for both initial and final designs of hybrid motor with its positive and negative peak values. Initial design is the design where magnets belonging to SPM and IPM motors are directly placed into the rotor. It is seen that peak to peak value of cogging torque has increased to 0.5 Nm from 0.36 Nm in final design.

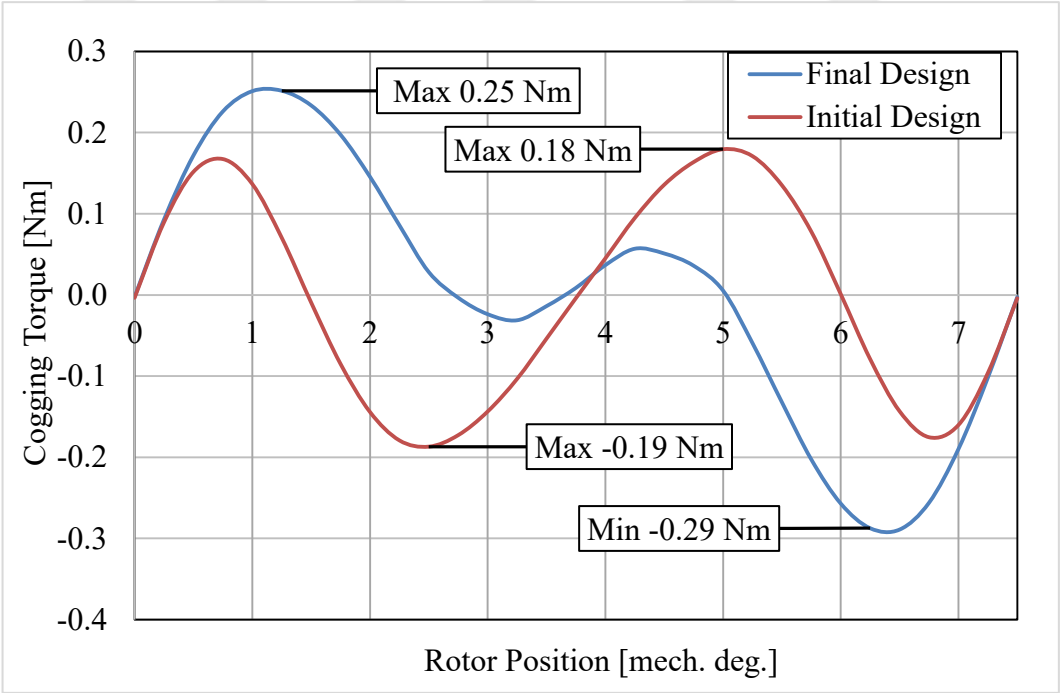

Figure 4.23: Cogging torque waveform of the final hybrid motor design obtained by 2D FEA.

Figure 4.24 shows the line voltage BEMF of initial and hybrid motor designs at 1000 rpm. It is seen that in the final design waveform is much more sinusoidal without distortions. THD for final design is 1.65% and 4.7% for the initial design.

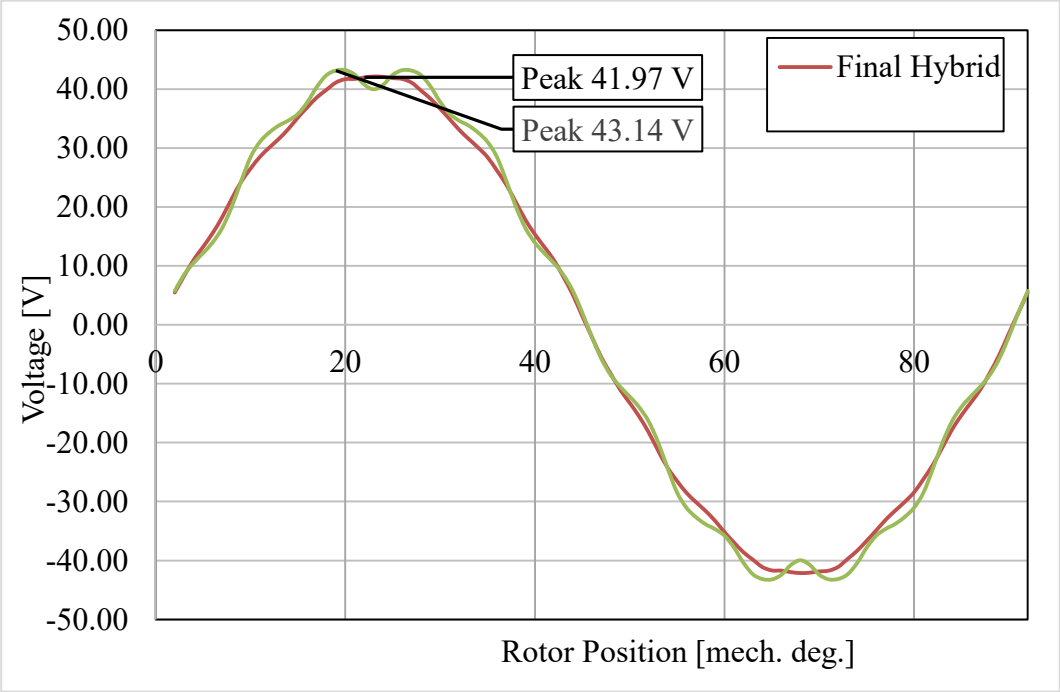

Figure 4.24: Induced line voltage waveforms of the initial and final hybrid motor designs obtained by 2D FEA.

4.3.2 On-load analysis

Final design of the hybrid motor is analysed at rated load and consequent results are shared. In Figure 4.25 on-load flux density distribution is given. Here maximum value of the flux density is observed as 1.72T at stator tooth. In Figure 4.26 flux lines distribution is given at on-load condition. Good pole forming is obtained according to the flux lines distribution throughout the motor. It is also seen that leakage flux between IPM and SPM magnets are also minimized by doing optimisation.

Torque waveform is also obtained for initial design as well as final design and given in Figure 4.27. Improvement of torque quality is selectible when initial and hybrid designs are compared. It is shown that by doing effective optimisation not only torque but also BEMF characteristics are improved.

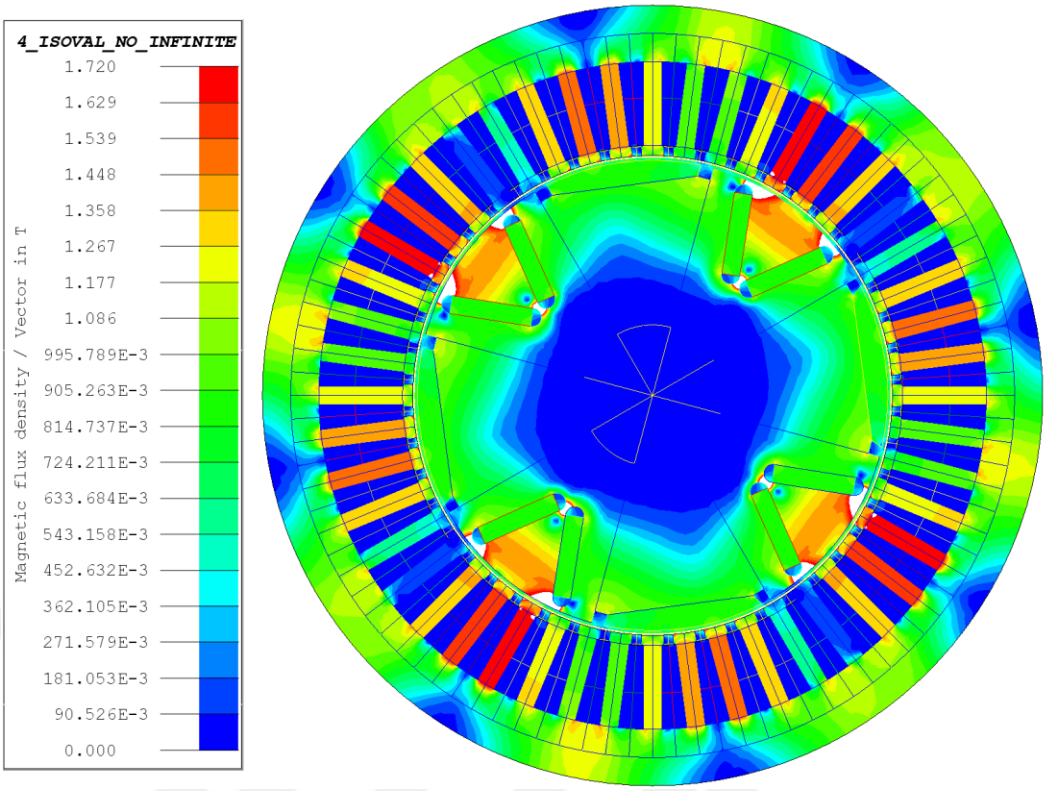

Figure 4.25: On-load flux density distribution of final hybrid motor design obtained

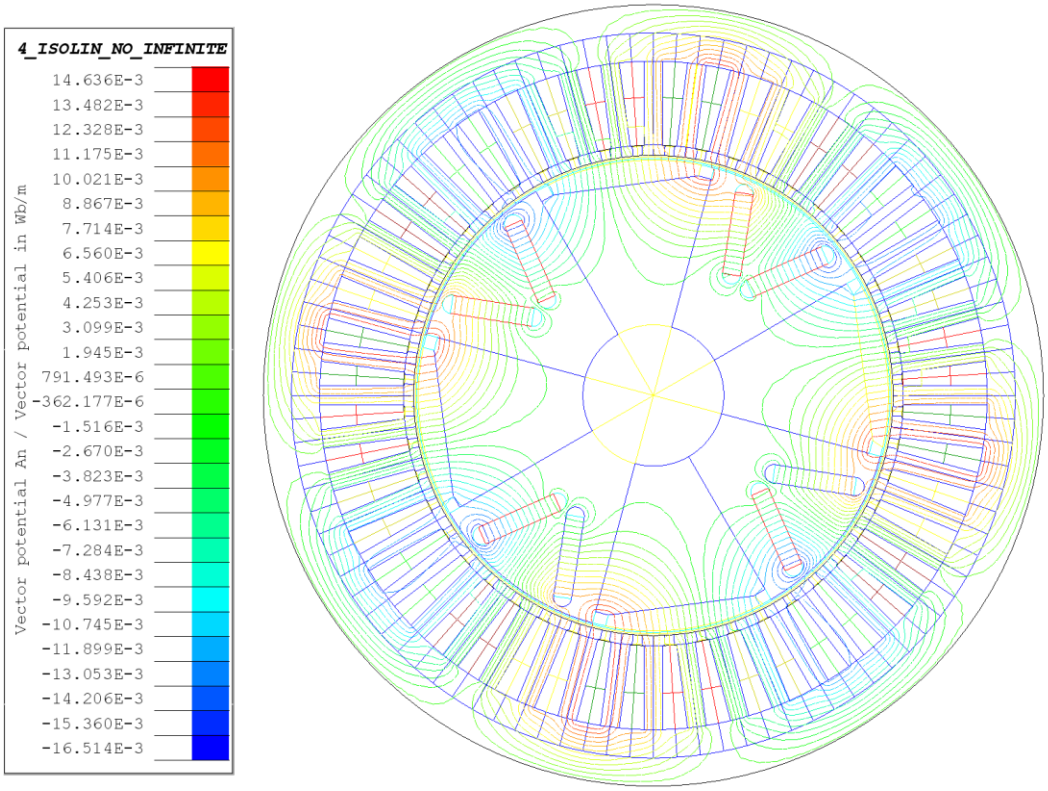

Figure 4.26: On-load flux lines distribution of the final hybrid motor design obtained by 2D FEA. by 2D FEA.

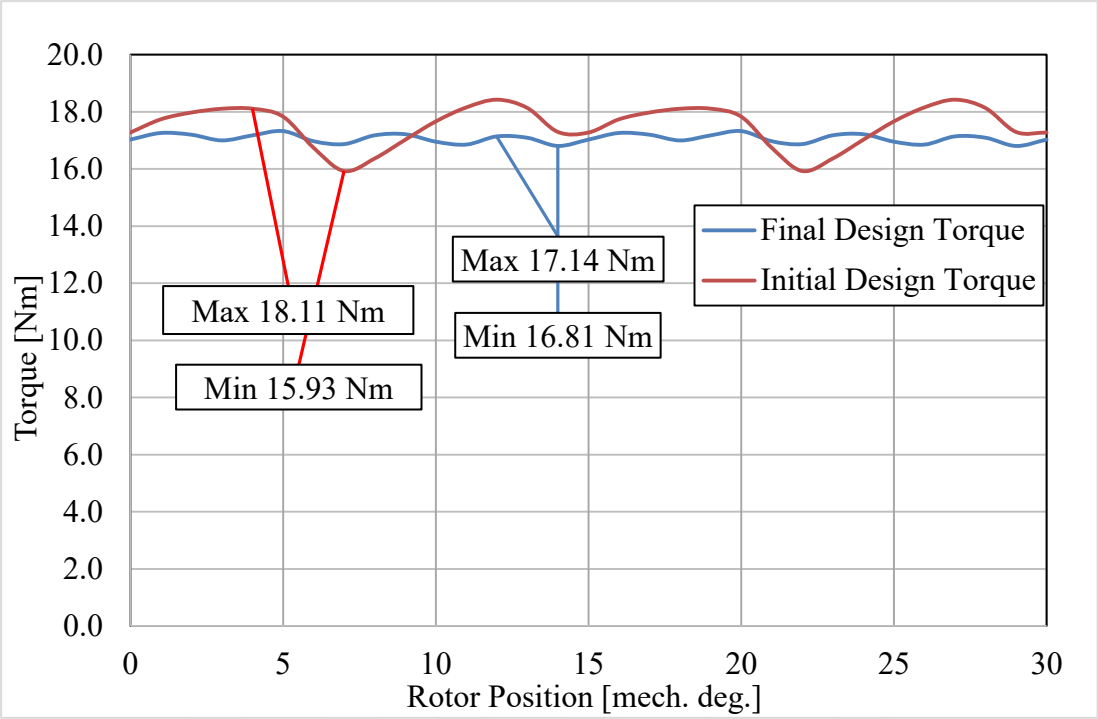

Figure 4.27: Output torque waveforms of the initial and final hybrid motor designs obtained by 2D FEA.

4.3.3 Torque-speed curves

Torque-speed curves are one of the most important characteristics of an electric motor. The maximum speed that can be reached is generally obtained by decreasing the total flux in a machine. This is is achieved by applying field weakening. In this work where 2D FEA is used as a design tool, field weakening is done by varying the current angle of the input current, thus opposing the magnet flux. As a result, main flux of the motor decreases, enabling it to reach higher speeds without surpassing the voltage limit of the system. Line voltage peak value of SPM motor is determined as the maximum voltage of the system.

Torque-speed curves of three machines are obtained and shown in Figure 4.28. It is seen that SPM motor has the highest average torque at rated speed with lowest maximum speed whereas IPM motor and hybrid motor has the same average torque at rated speed . IPM motor has the highest maximum speed and hybrid motor has a maximum speed in between SPM and IPM motor.

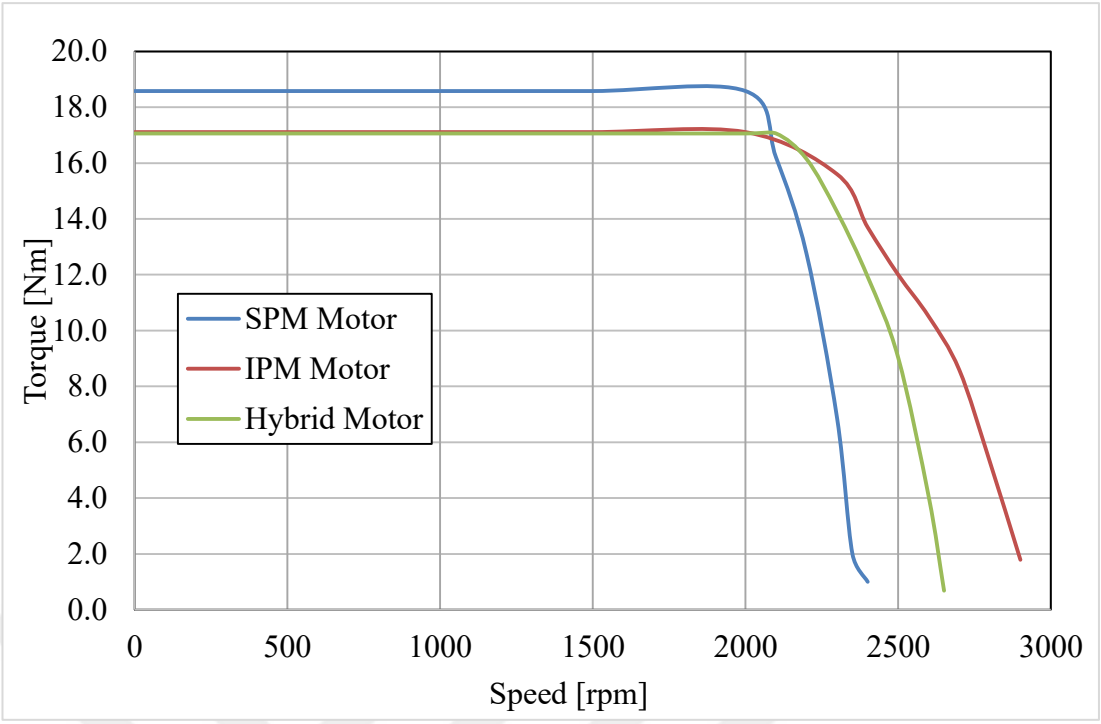

Figure 4.28: Torque-speed curves of SPM, IPM and hybrid motors.

4.3.4 Efficiencies and Comparison

In order to build the hybrid motor, SPM and IPM machines built and by their combination initial hybrid structure is formed. In Table 4.7 performances of these machines are depicted. It is seen that by proper optimisation hybrid motor becomes superior to SPM and IPM motor in terms of THD, torque ripple and cogging torque.

Table 4.7: Performance parameter comparison of designed motors.

Parameter	Unit	SPM	IPM	Initial Hybrid	Final Hybrid
Peak to peak cogging torque	Nm	0.6	1.8	0.37	0.54
Peak value of the line induced voltage	V	45	46.25	43.14	41.97
THD	%	4.44	5.67	4.7	1.65
Average torque	Nm	18.6	17.1	17.4	17.17
Torque ripple	%	7.73	19.7	14.2	3.3
Peak to peak cogging torque to average torque	%	3.22	10.5	2	3

Efficiencies of three motors are given in Table 4.8 at 500,1000,1500 and 2000 rpm speeds. It is seen that, at rated speed IPM motor has the highest efficiency following by SPM and hybrid motor.

Table 4.8: Efficiencies of three motors at different speeds obtained by 2D FEA and analytical methods.

Speed [rpm]	500			1000			1500			2000		
	SPM	IPM	Hybrid	SPM	IPM	Hybrid	SPM	IPM	Hybrid	SPM	IPM	Hybrid
Iron Loss [W]	9.13	8.95	9.66	20.48	20.17	21.80	33.83	33.41	36.18	49.00	48.61	52.00
Magnet Loss [W]	0.08	0.01	0.16	0.32	0.03	0.42	0.72	0.06	0.74	1.28	0.08	1.13
Copper Loss [W]	97.57	97.57	97.57	97.57	97.57	97.57	97.57	97.57	97.57	97.57	97.57	97.57
Friction (Bearing) Loss [W]	0.17	0.17	0.17	0.33	0.33	0.33	0.50	0.50	0.50	0.67	0.67	0.67
Windage Loss [W]	0.0042	0.0042	0.0042	0.0256	0.0256	0.0256	0.0754	0.0754	0.0754	0.16	0.16	0.16
Mechanical Power [W]	964.59	886.23	889.18	1926.95	1770.19	1775.88	2887.28	2652.07	2660.30	3845.74	3531.98	3543.25
Torque [Nm]	18.60	17.10	17.17	18.60	17.10	17.17	18.60	17.10	17.17	18.60	17.10	17.17
Input Power [W]	1071.37	992.76	996.58	2045.35	1887.98	1895.70	3019.47	2783.19	2794.87	3993.76	3678.40	3694.11
Efficiency [%]	90.03	89.27	89.22	94.21	93.76	93.68	95.62	95.29	95.19	96.29	96.02	95.92

5. PROTOTYPE MOTOR AND TEST RESULTS

In order to verify the hybrid motor it is aimed to built a prototype. For production purposes, original hybrid motor, which is designed in the previous section, is resized. Stator outer radius is increased to 90 mm, axial length of the motor is decreased to 36mm and air gap length is increased to 1.1mm in order to ease the production. By doing so rated speed of the motor is decreased to 1000 RPM where DC bus voltage is also decreased to 24 V.

5.1 On load and No load Analysis

Figure 5.1 shows the flux density distribution at rated load where maximum value is 1.53 T.

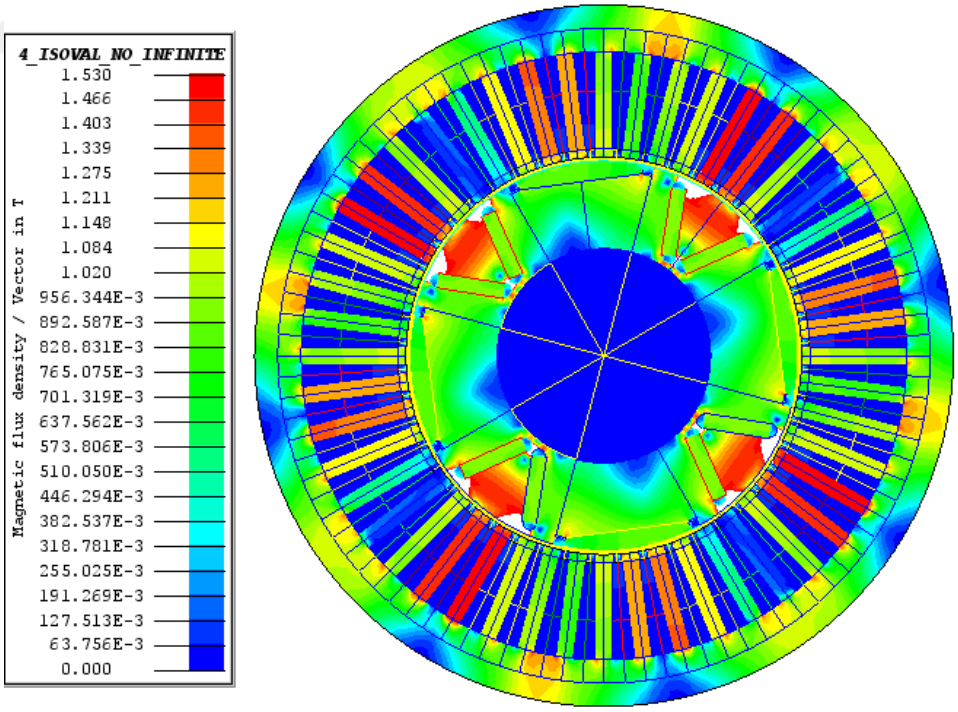

Figure 5.1: On-load flux density distribution of the prototype motor obtained by 2D FEA.

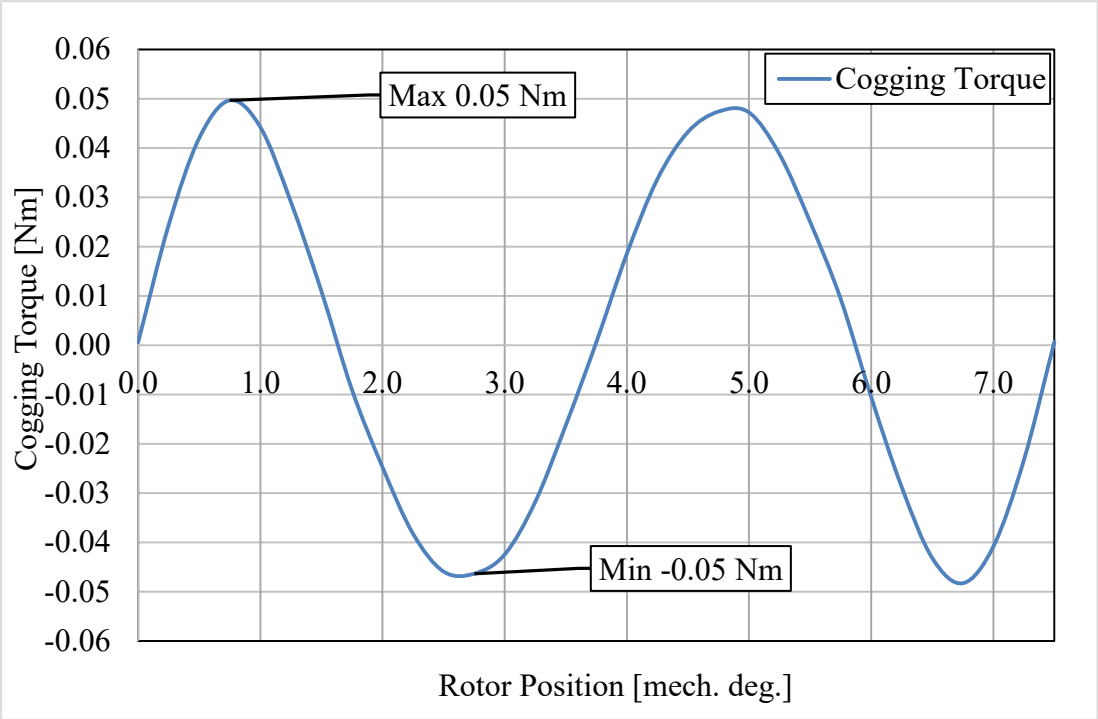

Figure 5.2: Cogging torque waveform of the prototype motor obtained by 2D FEA.

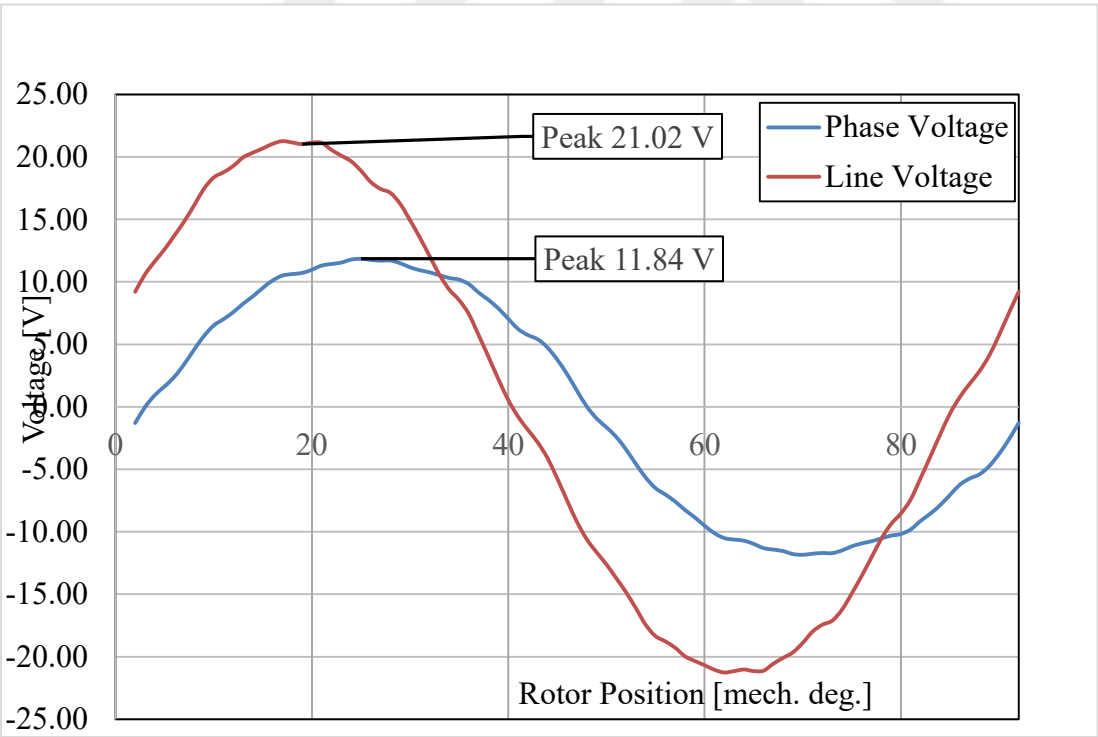

Figure 5.3: Phase and line induced voltage waveforms of the prototype motor obtained by 2D FEA at rated speed.

In order for IPM magnets to stay in the exact position, rotor slots are shaped differently than previous designs. Semi-circles on and under the IPM magnets are shifted for a certain amount which is also analyzed before production stage. It is also seen that by shifting the IPM slots torque characteristics may be affected. In order for these characteristics to remain special care has been taken. Same precaution is also taken for SPM magnets in order to place them correctly. A certain amount of thickness is let where SPM magnets are placed. This thickness is also analyzed for determination. In Figure 5.2 cogging torque waveform of the prototype motor is given. Peak to peak value of the cogging torque to average value of the output torque is 1.2%. Figure 5.3 and Figure 5.4 shows the BEMF characteristics of the prototype motor where line voltage THD is found to be 1.85%. Figure 5.5 shows the output torque waveform of the motor where average torque is 8.15 Nm with 2.17% ripple. Change in the rotor geometry for placement of magnets decreased torque ripple to 2.17% from 4%.

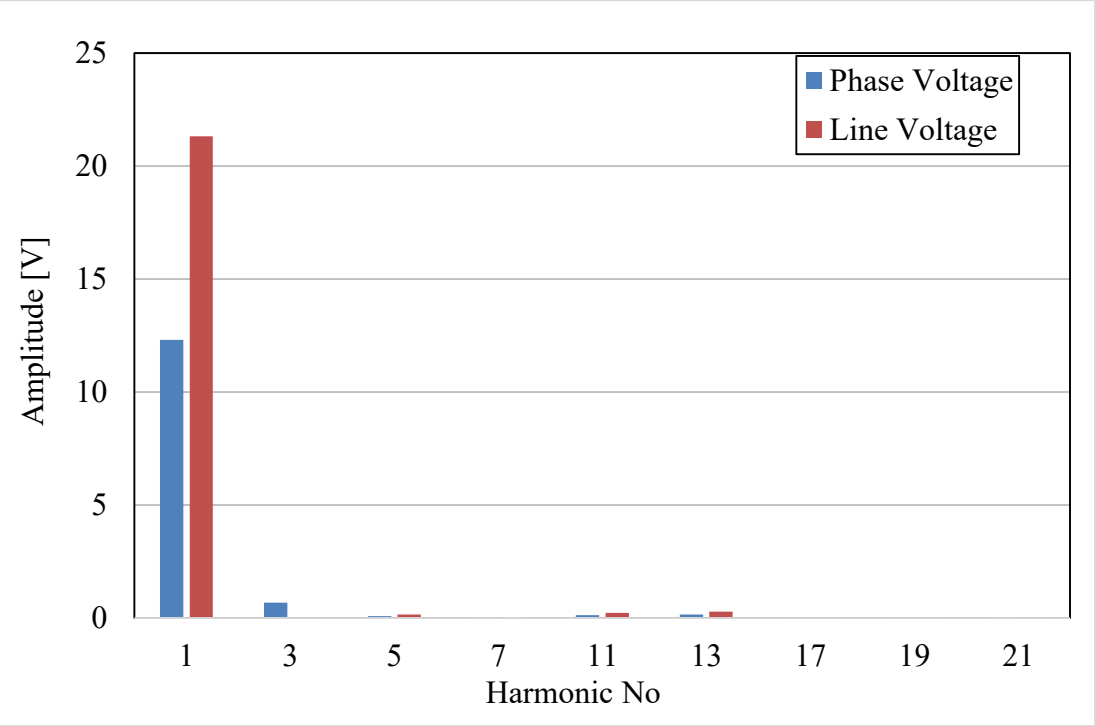

Figure 5.4: Harmonic spectrum of the phase and line induced voltages obtained by 2D FEA.

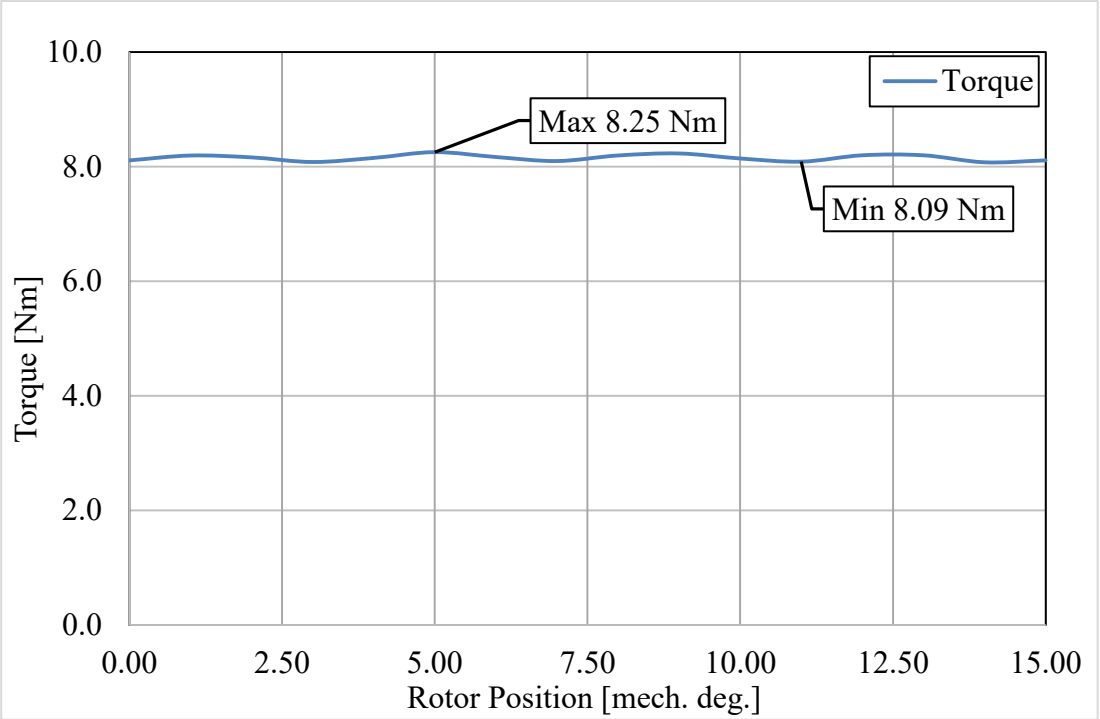

Figure 5.5: Output torque waveform of the prototype motor obtained by 2D FEA.

5.2 Test Results

After the prototype motor is built, no-load an on-load tests are done in order to verify the motor and compare the test results with analysis results.

Stator and rotor laminations are obtained by laser cutting machine which is shown in Figure 5.6. After the laminations are obtained, they are welded from predefined places. Stator of the prototype motor is shown in Figure 5.7.

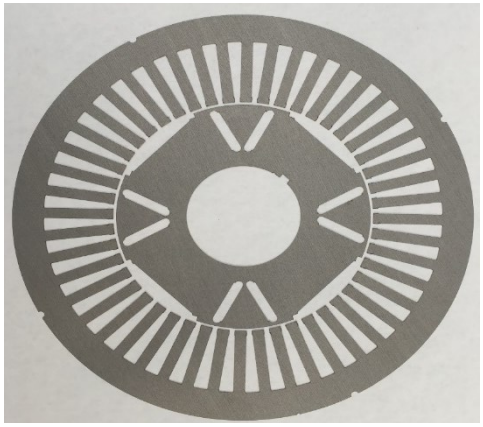

Figure 5.6: Single stator and rotor laminations of prototype motor cut from M270 steel sheet by using laser.

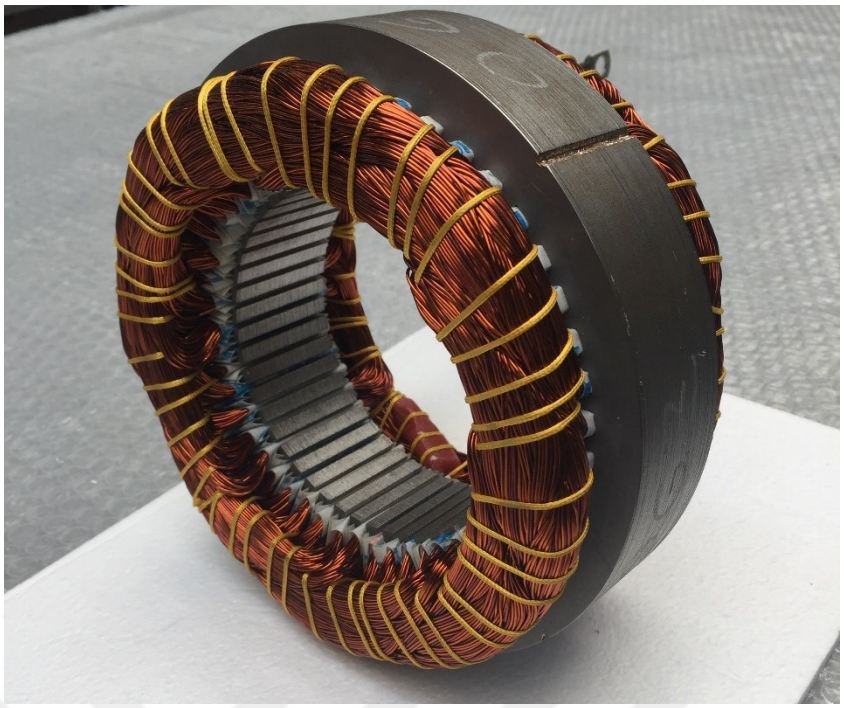

Figure 5.7: Stator of the prototype motor.

In order to weld the rotor, spaces near SPMs are used. SPM and IPM magnets are placed after welding process. Magnets are glued to the rotor by using special magnet glue. In Figure 5.8, rotor is shown with magnets installed.

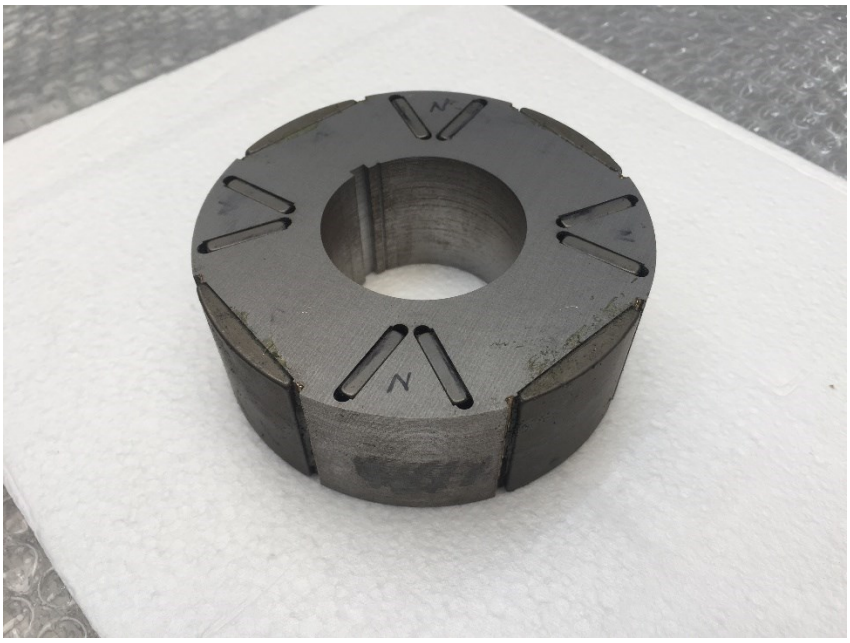

Figure 5.8: Rotor of the prototype motor with magnets installed.

Stator laminations are welded by using the small semi-circular area which is designed for this purpose. Later, winding of the stator is done. Two turns of the stator is winded in 29 strands each having an outer diameter of 0.7mm. Insulation of class H is inserted into the slots before the coils are inserted. By using high voltage insulation test device, insulation tests of the prototype motor is done with phase-phase resistance and inductances. Calculated values of phase-phase resistance is 23.6 m-ohm and phase-phase inductance is 0.2 mH. Maximum value of difference between calculated and obtained values by test is within 5.5%. This is caused by unpredictable end winding lengths. Shaft of the prototype motor is built with sufficient tolerances in order to get in the welded rotor laminations. Shaft of the motor is shown in Figure 5.9.

Table 5.1: Insulation test of the prototype motor with phase resistance and inductances

Testing Item	Lower Limit	Upper Limit	Testing Value
Hi-pot [mA]	0.3	10	0.867
Insulation Resistance [M-ohm]	20	-	>500
Phase-Phase Resistance 1 [m-ohm]	-	-	25.04
Phase-Phase Resistance 2 [m-ohm]	-	-	24.83
Phase-Phase Resistance 3 [m-ohm]	-	-	24.78
Resistance Balance [%]	-	-	0.64
Phase-Phase Inductance 1 [mH]	-	-	0.2014
Phase-Phase Inductance 2 [mH]	-	-	0.1926
Phase-Phase Inductance 3 [mH]	-	-	0.1898
Balance Inductance [%]	-	-	3.49

In order to test the prototype motor, an existing test fixture is used. Stator and rotor is mounted into the fixture. Test fixture is then, mounted on the test system where it is coupled to torque transducer as shown in Figure 5.10. Prototype motor is drove by 30kW load motor.

Figure 5.9: Shaft of the prototype motor.

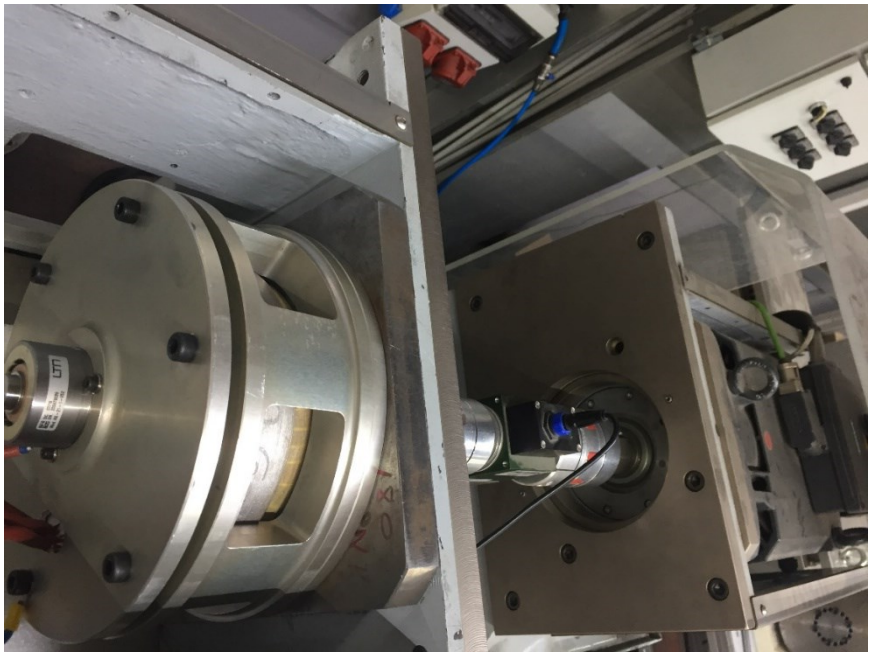

Figure 5.10: Test fixture and test system of the prototype motor.

5.2.1 No-load Tests

In order to test the motor without load, load motor is operated in speed mode. Prototype motor phases are left open and by using probes, induced voltages are made to be displayed on Tektronix TPS 2024B oscilloscope. In addition to BEMF tests, torque is measured at very low speed in order to obtain cogging torque.

Since magnet properties from datasheets are generally different in real tests, residual flux density and permability of the SPM and IPM magnets are changed and analysis are re-done. Magnets tests are given in Appendix E and Appendix F, in Figure E.1 and Figure F.1 Comparison data is based on the test data of magnets.

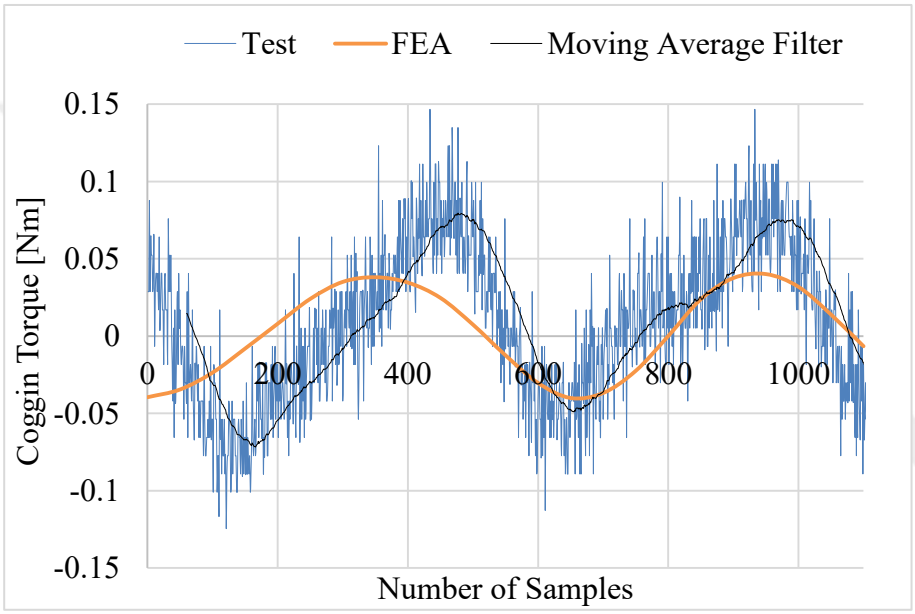

Figure 5.11: Cogging torque of the prototype motor obtained from test.

In order to measure the cogging torque, load motor is rotated at 1 rpm at no-load where prototype motor is given no current. Obtained data is given in Figure 5.11. It can be seen that, test data is rich in noise. This disturbances are caused by mechanical vibrations where couplings of two motors are the main reason for vibrations. In order to filter the test data, moving average is applied and shown in figure. If analysis result and filtered waveform of the test data is compared, it is seen that they are close to each other. It is imporant to note that, measuring cogging torque is not an easy task as it requires precise measurement tools. Moreover, in the test system prototype motor is drove by a load motor, which has 30 times the power of prototype motor. Although the load motor is operated at no-load, its cogging torque and no-load torque is also transferred to torque sensor, making the measured data disturbed.

Induced voltage of the prototype motor is measured by rotating the load motor at various speeds. In Figure 5.12 phase to phase BEMF of the prototype motor is given. Even though the waveforms are smooth, peak area of the waveform contains some noise caused by the load motor and test system.

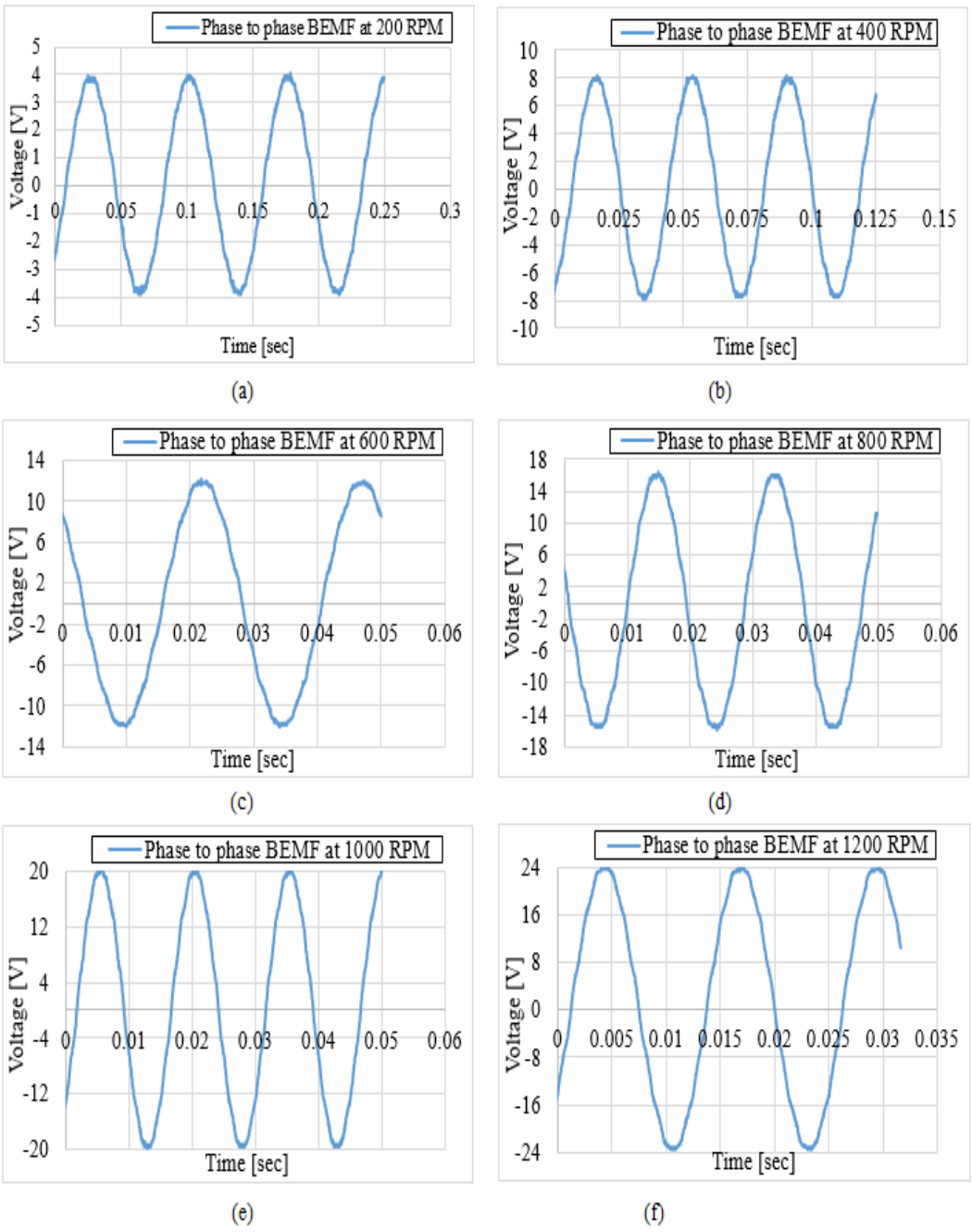

Figure 5.12: Phase to phase induced voltage of prototype motor at different speeds obtained from test: (a) 200 RPM, (b) 400 RPM, (c) 600 RPM, (d) 800 RPM, (e) 1000 RPM, (f) 1200 RPM.

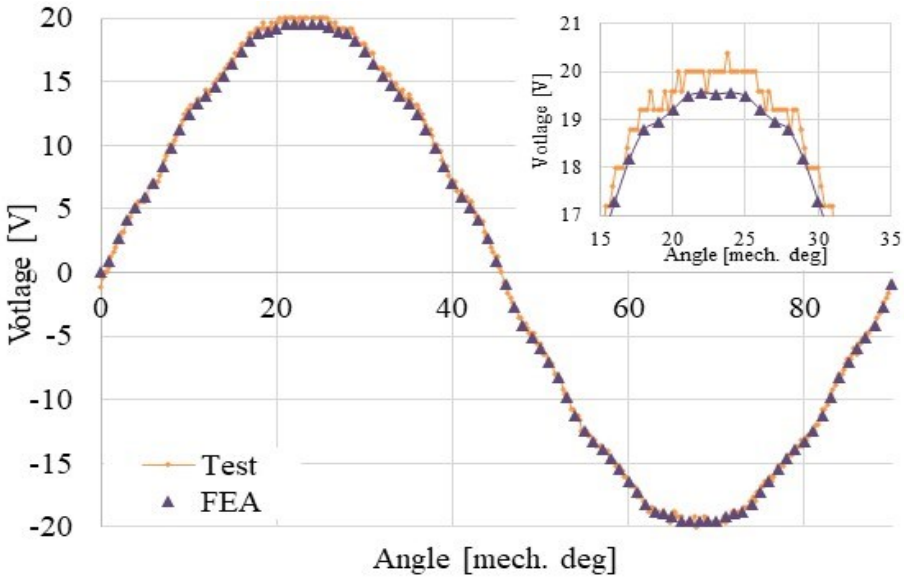

Figure 5.13: Comparison of analysis and test result for phase to phase BEMF at 1000 RPM.

In order to compare induced voltage at rated speed, test data and analysis data are plotted together in Figure 5.13. It is seen that fine agreement between test and analysis results is obtained. BEMF waveform as seen in oscilloscope screen is shown in Figure 5.14.

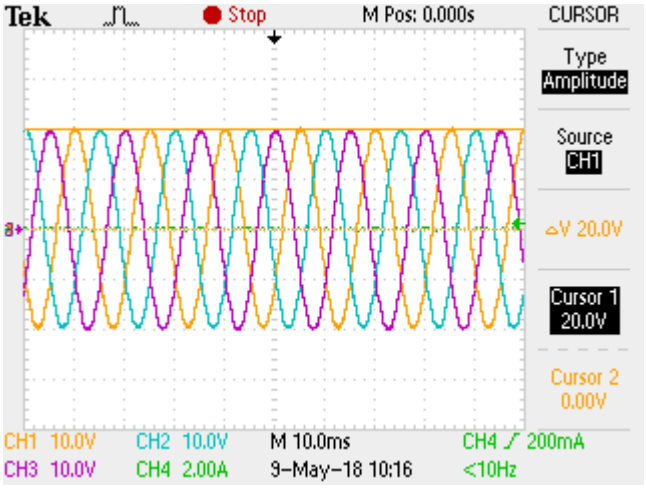

Figure 5.14: Oscilloscope view of the induced BEMF at rated (1000 RPM) speed.

5.2.2 On-load tests

On-load tests are done by rotating the load motor at no load and desired speed where the prototype motor is given three phase current. By doing so, data from the torque transducer gives the shaft torque of the motor. It is important to note that, in the previous analysis results electromagnetic torque obtained by 2D FEA software was given. However, electromagnet torque is not the shaft torque as losses are not taken into account. In order to do so, core loss and mechanical loss of the machine is subtracted from the electromagnetic power to find output power. In Table 5.2 efficiency compıtation of prototype motor is given. At this speed, 8.05 Nm of output torque is expected.

Table 5.2: Efficiency computation of the protoype motor at rated speed obtained by 2D FEA.

Electromagnetic Torque [Nm]	8.15
Speed [rpm]	1000.00
Electromagnetic Power [W]	853.47
Iron Loss [W]	10.48
Magnet Loss [W]	0.09
Copper Loss [W]	52.33
Windage Loss [W]	0.02
Friction Loss [W]	0.16
Total Loss [W]	63.08
Output Power [W]	842.80
Input Power [W]	905.89
Shaft Torque [Nm]	8.05
Efficiency	93.04

By giving the half of the rated current, prototype motor is driven at half-load where load motor is rotated at 400,800,100 and 1200 RPM speeds. Output torque of the prototype motor is shown in Figure 5.15. It is seen that the obtained waveforms are not smooth. Fluctuations occure due to mechanical vibrations caused by the couplings and load motor. Although the average torque can be computed, it is not possible to account for precise torque ripple. Average torques of output torque waveforms for 400, 800, 1000 and 1200 RPM speeds are 4.05, 4.01, 4 and 1.4 respectively. As the motor BEMF becomes very close to 24V DC bus voltage, driver can not provide the 17.6 A (RMS) current, this is the reason that 1.4 Nm of output torque is obtained at 1200 RPM.

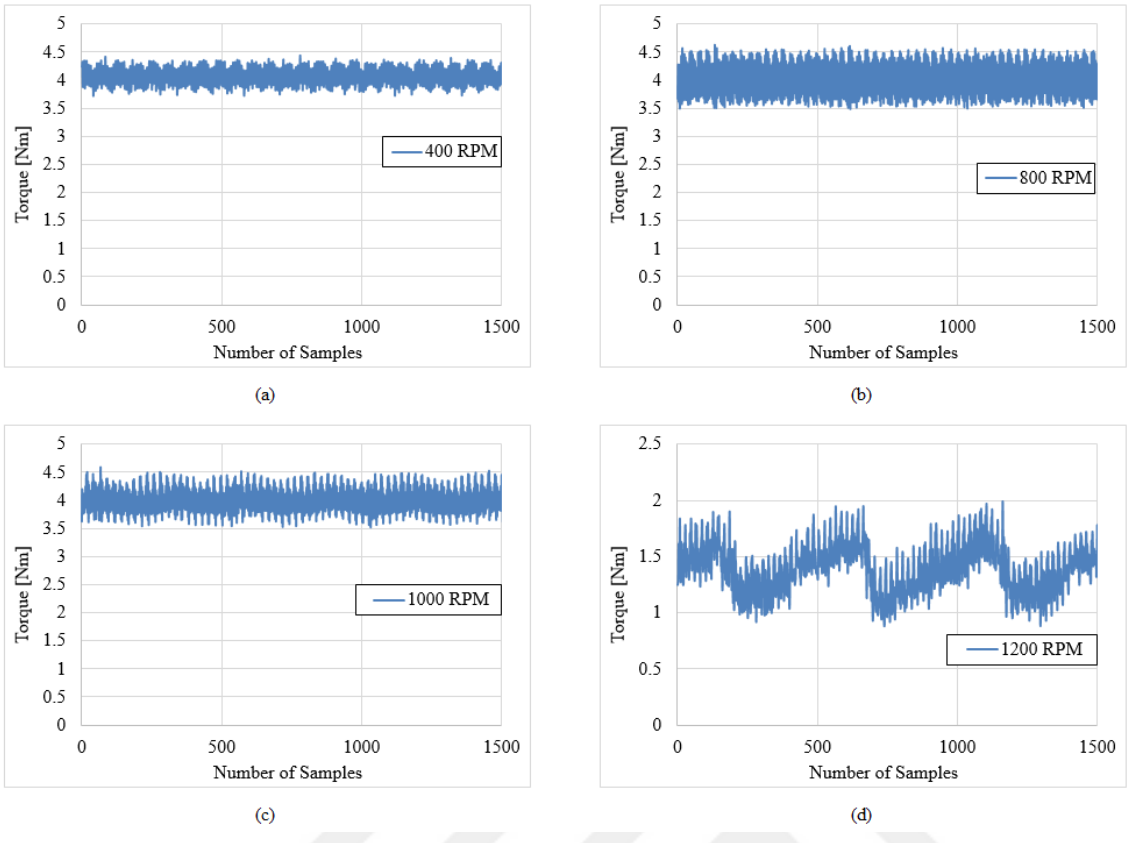

Figure 5.15: Output torque of the prototype motor obtained at different speeds for half load condition: (a) 400 RPM, (b) 800 RPM, (c) 1000 RPM, (d) 1200 RPM.

Prototype motor is operated by load motor at 400, 800, 1000 and 1200 RPM speeds at rated current (35.3 A-RMS) and output torque waveforms are given in Figure 5.16. As explained before, because of the mechanical vibrations caused by load motor and couplings, there are fluctuations in the output torque data waveform. 7.84 Nm, 7.8 Nm, 7.78 Nm and 1.36 Nm average values are obtained at 400, 800, 1000 and 1200 RPM speeds. When averages values of test and analysis results are compared, the difference is 3.35%, which concludes as good agreement.

Another cause of the difference between test and analysis results is the current supplied by the driver. Motor drive in the test system lacked precise current adjustment and 34.8 A (RMS) current value is the closes value that could be obtained. Supply current waveform with its RMS and peak value is shown in Figure 5.17.

It is seen that at 1200 RPM speed in Figure 5.16 (d), output torque decreases to an average value of 1.36 Nm. As it was in the case in half-load tests, at this speed, since the motor BEMF becomes close to 24V DC bus voltage, power supply is unable to give desired torque,

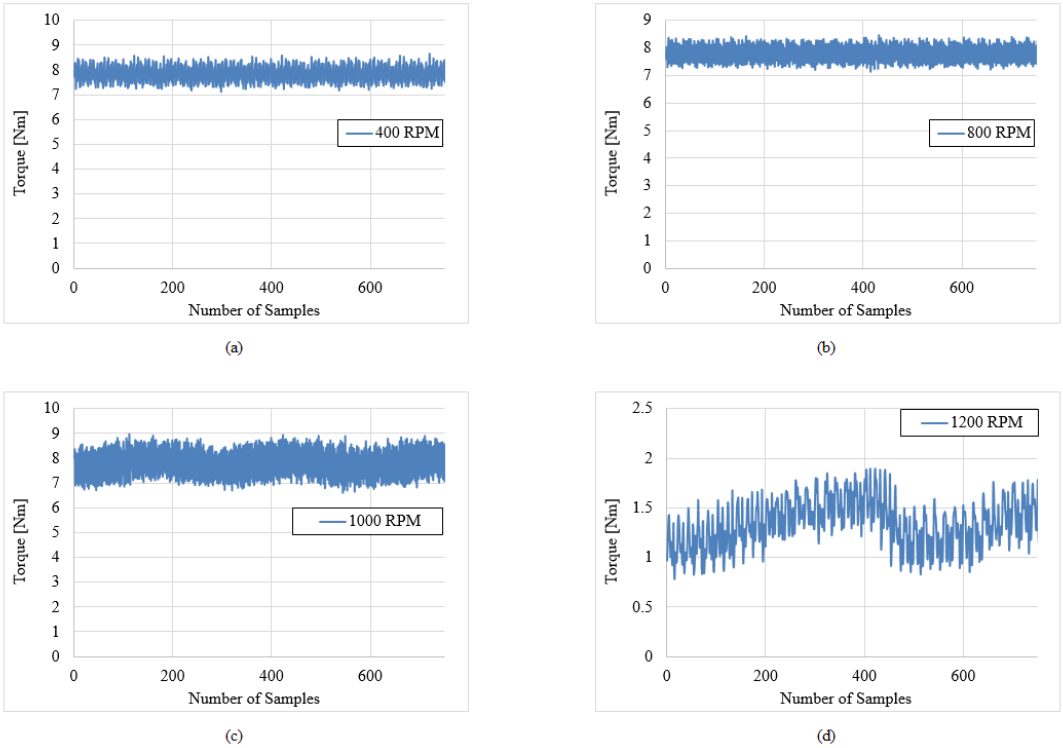

Figure 5.16: Output torque of the prototype motor obtained at different speeds for full load condition: (a) 400 RPM, (b) 800 RPM, (c) 1000 RPM, (d) 1200 RPM.

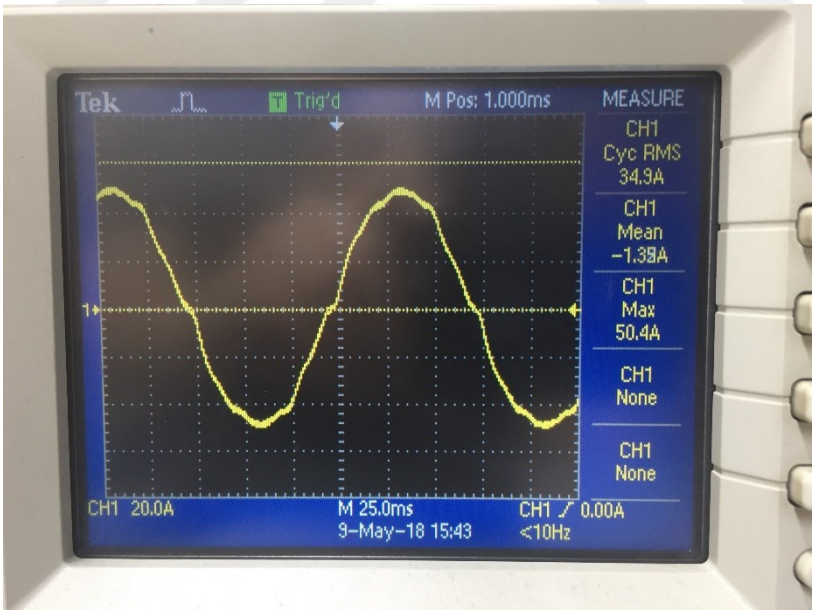

Figure 5.17: Supply current of the prototype motor at rated load and speed.

By using 2D FEA, field weakening operation is simulated by adjusting the current angle. Current angle is adjusted so that, on-load BEMF peak value at speeds higher than 1000 RPM does not exceed 24 V DC bus voltage. Change of current angle causes displacement of stator magnetic field to oppose rotor magnetic field in order to reduce total flux, hence enables operation at higher speeds. By applying field weakening in analysis, torque-speed curve of the prototype motor is obtained. Torque-speed curve obtained by analysis and test results are given in Figure 5.18. It is important to note that, test system does not have the capability to operate in field weakening region. As in contrast to analysis results, torque-speed curve obtained by the test is due to the power supply and drive effect where at higher speeds motor drive and power supply reduces the supply current as it can not give desired value at low potential difference.

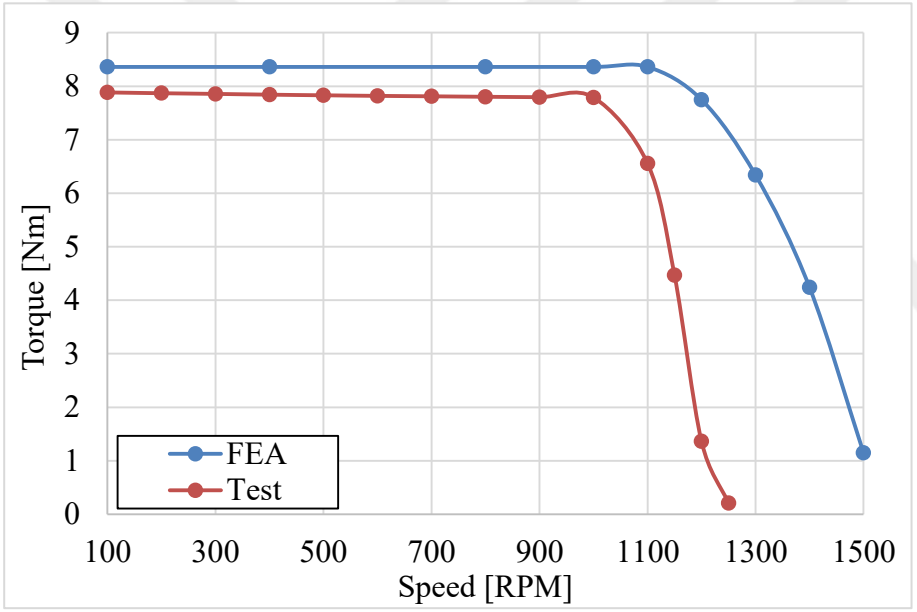

Figure 5.18: Torque-speed curves of prototype motor obtained by FEA and test.

6. CONCLUSION

Considering the recent concerns about environment, it is obvious that the trend is to get more performance from less or same amount of material. When this concerns meet electric motors, it can be said that improvement in any performance parameter will contribute. In this study, a hybrid permament magnet rotor structure is investigated in order to search for its limits and capabilities.

Hybrid rotor is first designed for a 27 slot 8 pole fractional combination. An SPM motor which is already designed is used as a reference motor for the design of an IPM motor. Later by combining the SPM and IPM motors' rotors, hybrid structure is formed. Dimensions and positions of SPMs and IPMs are varied together in order to see the effect on cogging torque and output torque characteristics by using 2D FEA. It is seen that the optimisation results for obtaining the best cogging torque do not cover the optimisation results for output torque characteristics. The reason is the assymmetrical structure of the slot-pole combination which is further increased by combining SPMs and IPMs. Final model is chose according to the lowest torque ripple. Cogging torque is much more higher than SPM and IPM motors and average torque is same. Torque ripple of the final design is also higher than SPM and IPM motors. When these parameters are evaluataed alone, hybrid motor provide quite good output characteristics in terms of both harmonic distortion, average torque, torque ripple and cogging torque. However when a comparison is made, hybrid motor becomes a poor competitor for reference SPM and IPM motors.

In order to investigate hybrid motor in a different combination, an SPM motor is designed with 48 slot 8 pole integer slot combination. Design procedure is started with analytical equations for the initial design and continued with 2D FEA for detailed design and optimisation. Afterwards an IPM motor is designed keeping the magnet volume same as a constraint and necessary optimisations are done in order to find the lowest torque ripple design. Hybrid rotor is then formed by combining the SPMs and

IPMs. Wide range optimisation is done in order to find the best design giving the lowest torque ripple. The difference between initial and final designs of hybrid motor is quite an amount, showing the importance of optimisation in an electric motor. Torque-speed curves of SPM, IPM and hybrid motor is obtained by using 2D FEA and efficiencies are calculated. According to the results, highest average torque is obtained with the SPM motor and lowest torque ripple is obtained with hybrid motor which was the aim at the beginning. Maximum speed that can be reached by field weakening is achieved with IPM motor where hybrid motor is in the middle between SPM and IPM. It is also important to note that, although the efficiencies are close at the rated speed hybrid motor has the lowest efficiency followed by the SPM motor.

A prototype motor is decided to be built in order to demonstrate its performance. Resizing is done on the final 48 slot 8 pole hybrid design for ease in manufacturing and testing. After the protoype has been built, it has been tested in laboratory. Necessary comparisons are made in order to verify analysis results with test results. Less than 1% difference is measured between test and analysis results for BEMF computation and nearly 3.5% difference is measured between test and analysis results of output torque.

In this study main aim was to obtain minimum tork ripple and optimisations are done accordingly. High number of geometric parameters of the hybrid rotor structure enables to search and focus for a certain performance parameter. For further work, hybrid motor can be studied to obtain high maximum speed, low cogging torque, high peak BEMF, high average torque, high efficiency and high power density by multi-parameter and/or multi-function optimisation technique. Also, by using advanced analytical methods hybrid structure can be further studied.

REFERENCES

[1] **ABB.** (2011). Powering the world economy: Is there a better way to use electricity?

[2] **Waide P., Brunner C. U.** (2011). Energy-Efficiency Policy Opportunities for Electric Motor-Driven Systems. International Energy Agency.

[3] **Url-1** <https://www.abb-conversations.com/2017/07/abb-motor-sets-world-record-in-energy-efficiency> , 27.02.2018.

[4] **Doppelbauer M.** The Invention of the Electric Motor 1800-1854:A short history of electric motors-Part 1. Karlshure Institute of Technology.

[5] **Doppelbauer M.** The Invention of the Electric Motor 1856-1893:A short history of electric motors-Part 2. Karlshure Institute of Technology.

[6] **Urquhart J. W.** (1882). A Treatise on the Means and Apparatus Employed in the Transmission of Electrical Energy and Its Conversion into Motive Power.

[7] **Ohio Electric Motors Inc.** (2015) A Historical Overview of Permanent Magnet Motors.Retrievedfrom:http://www.ohioelectricmotors.com/2015/07/a-historical-overview-of-permanent-magnet-motors

[8] **Livingston J.D.** (1996). Driving Force: The Natural Magic of Magnets. Harvard Univeristy Press,Cambridge.

[9] **Gieras J.** (2010). Permanent Magnet Motor Technology: Design and Applications (3rd ed. p.5)

[10] **Arnold Magnetics.** Sintered Neodymium-Iron-Boron Magnets N30UH Datasheet.Retrieved from: http://www.arnoldmagnetics.com/products/neodymium-iron-boron-magnets

[11] **Widmer J., Martin R., Kimiabeigi M.** (2015). Electric Vehicle Traction Motors Without Rare Earh Materials. Sustainable Materials and Technologies. vol. 3, pp 7-13.

[12] **Altair Flux.** Troy, Michigan. (Computer Software)

[13] **Soong W. L., Miller T.J.E.** (1994). Theoretical Limitations to the Field-Weakening Performance of the Five Classes of Brushless Synchronous AC Motor Drive.

[14] **Özpineci B. (2016).** Oak Bridge National Laboratory Annual Progress Report for the Electric Drive Technologies Program. Oak Ridge National Laboratory Annual Progress Report for the Electric Drive Technologies Program

[15] **Burress T. A, Campbell S. L., Coomer C. L., Ayers C. W., Wereszczak A. A., Cunningham J. P., Marlino L. D., Seiber L. E., Lin H. T.** (2011) Evaluation of the 2010 Toyota Prius Hybrid Synergy Drive System. Energy and Transportation Science Division, Oak Ridge National Laboratory.

[16] **Binns K. J., Jabbar M. A. and Parry G. E.** (1979). Hybrid permanent-magnet synchronoys motors. Electrical Engineers, Proceedings of the Institution of. vol.125, no.3, pp. 203-208.

[17] **Binns K. J., Jabbar M. A. and Parry G. E.** (1979). Choice of parameters in the hybrid permanent-magnet synchronous motor. Electrical Engineers, Proceedings of the Institution of, vol. 126, no. 8, pp. 741-744.

[18] **B. N. Chaudhari, B. G. Fernandes and S. K. Pillai.**(1998) A new hybrid rotor geometry for permanent magnet synchronous motor. *International Conference on Power Electronic Drives and Energy Systems for I ndustrial Growth, 1998. Proceedings*. vol.1. pp. 260-263

[19] **I. Petrov, Y. Liu, V. Abramenko, P. Lindh and J. Pyrhönen.** (2017). Direct-on-line-start permanent-magnet-assisted synchronous reluctance machine with ferrite magnets. *IECON 2017 - 43rd Annual Conference of the IEEE Industrial Electronics Society*. pp.1911-1918.

[20] **Zhang F., Jia G. Zhao Y., Yang Z., Cao W. (2015).** Simulation and Experimental Analysis of a Brushless Electrically Excited Synchronous Machine with a Hybrid Rotor. IEEE Transaction on Magnetics. vol. 51

[21] **Zhang L., Fan Y., Cui R., Li C., Cheng M.** (2016). Design and Analysis of a New Five-Phase Brushless Hybrid –Excitation Fault-Tolerant Motor for Electric Vehicles.

[22] **Zhu X., Wang X., Zhang C., Wang L., Wu W.** (2017). Designed and Analysis of a Spoke-Type Hybrid Permanent Magnet for Electric Vehicles. IEEE Transactions on Magnetics. vol.53. no.11

[23] **Yang H., Li Y., Lin H., Zhu Z.Q., Lyu S., Wang H.** (2017). Novel Reluctance Axis Shifted Machines with Hybrid Rotors.

[24] **Liu G., Xu G., Zhao W., Du X.** (2017). Improvement of Torque Capability of Permanent-Magnet Motor by Using Hybrid Rotor Configuration. IEEE Transactions on Energy Conversion. vol.32, no.3.

[25] **Xu G., Liu G., Jiang S., Chen Q.** (2018). Analysis of a Hybrid Rotor Permanent Magnet Motor Based on Equivalent Magnetic Network. IEEE Transactions on Magnetics. vol.54, no.4.

[26] **Jahns T. M., and Soong W.L.** (1996). Pulsating Torque Minimization Techniques for Permanent Magnet AC Motor Drives-A Review. IEEE Transactions on Industrial Electronics. vol. 43, no. 2, pp. 321-330.

[27] **Zhu Z. Q. Howe D.** (2000). Influence of Design Parameters on Cogging Torque in Permanent Magnet Machines. IEEE Transactions on Energy Conversion. vol. 15, no. 4, pp. 407-412

[28] **Chu W. Q., Zhu Z. Q.** (2013). Reduction of On-Load Torque Ripples in Permanent Magnet Synchronous Machines by Improved Skewing. IEEE Transactions on Magnetics. vol. 49, no. 7, pp. 3822-3825

[29] **Fei W., Zhu Z. Q.** (2013). Comparison of Cogging Torque Reduction in Permanent Magnet Brushless Machines by Conventional and Herringbone Skewing Techniques. IEEE Transactions on Energy Conversion. vol. 28, no. 3, pp. 664-674

[30] **Pyrhönen J., Jokinen T. Hrabovcova V.** (2008). Design of Rotating Electrical Machines.

[31] **Fukui S., Ogawa J., Sato T., Tsukamoto N., Kashima N., Nagaya S.** (2011). Study of 10MW-Class Wind Turbine Synchronous Generators with HTS Field Windings. IEEE Transactions on Applied Superconductivity. vol.21, no.3, pp. 1151-1154.

[32] **Huyn C., Zheng L., Acharya D.** (2008). Losses in High Speed Permanent Magnet Machines Used in Microturbine Applications.

[33] **Krdings A., Soulard J.** (2010). Overview of Comparison of Iron Loss Models for Electrical Machines.

[34] **Jubb G. A., McCurrie A.** (1986). Hystheresis and magnetic viscosity in a Nd-Fe-B permanent magnet. IEEE Transaction on Magnetics. vol.23. no. 2. pp. 1801-1805.

[35] **Fukuma A., Kanazawa S., Miyagi D., Takahashi N.** (2005). Investigation of AC Loss of Permanent Magnet of SPM Motor Considering Hystheresis and Eddy-current losses. IEEE Transaction on Magnetics. vol.41. no.5. pp. 1964-1967.

[36] **Pyrhönen J., Ruoho S., Nerg J., Paju M., Tuominen S., Kankaanpaa H.i Stern R., Boglietti A.** (2015). Hystheresis Losses in Sintered NdFeB Permanent Magnets in Rotating Electrical Machines.

[37] **Vranrick J. E.** (1968). Prediction of Windage Power Loss in Alternators. NASA-Langey Report No: TND-4849.

[38] **Dutta R., Chong L., Rahman F. M.** (2013). Analysis and Experimental Verification fo Losses in a Concentrated Wound Interior Permanent Magnet Machine. Progress in Electromagnetics Research B. vol.48. pp 221-248.

[39] **International Standart IEC 60034-(1-31).** (2010-2016). Standarts for rotating electric machines.

APPENDICES

APPENDIX A: Properties of used material.

APPENDIX B: Winding layouts.

APPENDIX C: Test results of the magnet materials.

Table A.1 : B and H data for the M270 Steel used in all analysis and prototype motor.

H [A/m]	B [T]
0.00	0.00
29.38	0.10
37.39	0.20
45.24	0.30
50.18	0.40
55.45	0.50
62.07	0.60
70.32	0.70
81.92	0.80
96.58	0.90
118.68	1.00
155.51	1.10
226.67	1.20
416.07	1.30
1059.27	1.40
2756.65	1.50
5441.90	1.59
7069.65	1.64
8213.34	1.67
10000.00	1.72
20000.00	1.86
30000.00	1.92
50000.00	1.99
100000.00	2.09
200000.00	2.23
300000.00	2.37

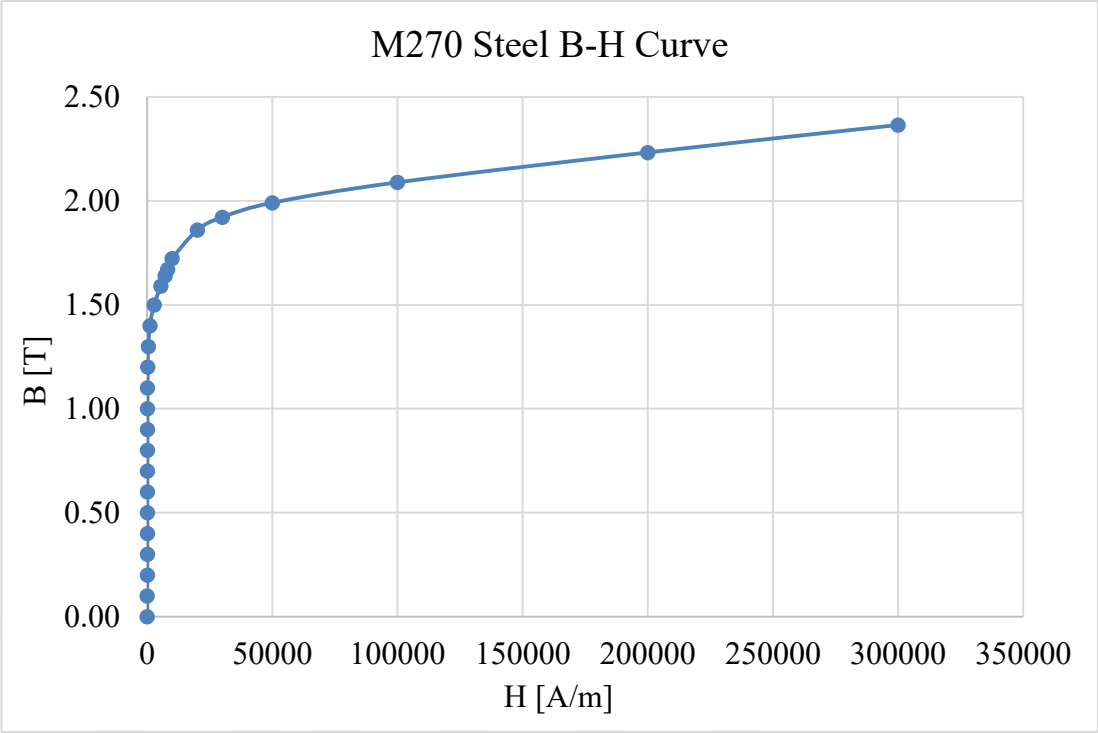

Figure A.1 : B-H curve of M270 steel.

N30UH

Sintered Neodymium-Iron-Boron Magnets

These are also referred to as "Neo" or NdFeB magnets. They offer a combination of high magnetic output at moderate cost. Please contact Arnold for additional grade information and recommendations for protective coating. Assemblies using these magnets can also be provided.

	Characteristic	Units	min.	nominal	max.
Magnetic Properties	**Br**, Residual Induction	Gauss	10,800	11,250	11,700
		mT	1080	1125	1170
	H_{cB}, Coercivity	Oersteds	10,200	10,700	11,200
		kA/m	812	852	891
	H_{cJ}, Intrinsic Coercivity	Oersteds	25,000		
		kA/m	1,990		
	BHmax, Maximum Energy Product	MGOe	28	31	33
		kJ/m^3	223	243	263

	Characteristic	Units	C //	C ⊥
Thermal Properties	Reversible Temperature Coefficients (1)			
	of Induction, α(Br)	%/°C	-0.120	
	of Coercivity, α(Hcj)	%/°C	-0.465	
	Coefficient of Thermal Expansion (2)	ΔL/L per °Cx10^{-6}	7.5	-0.1
	Thermal Conductivity	W / (m • K)	7.6	
	Specific Heat (3)	J / (kg • K)	460	
	Curie Temperature, Tc	°C	310	
Other Properties	Flexural Strength	psi	41,300	
		MPa	285	
	Density	g/cm^3	7.5	
	Hardness, Vickers	Hv	620	
	Electrical Resistivity, ρ	μΩ • cm	180	

Notes: (1) Coefficients measured between 20 and 180 °C
(2) Between 20 and 200 °C (3) Between 20 and 140 °C

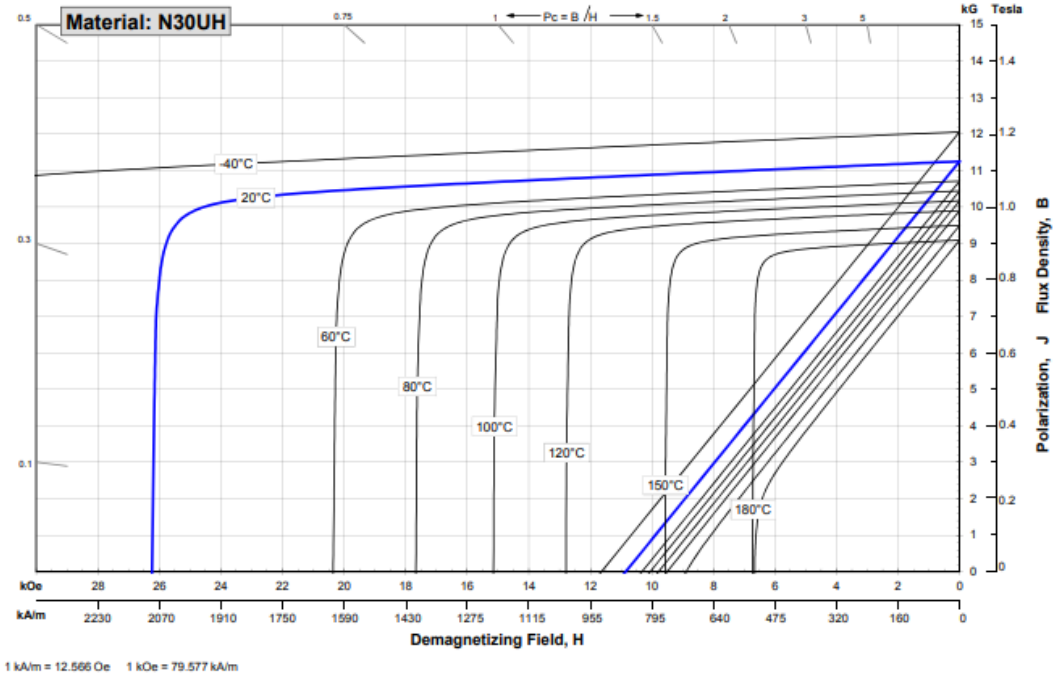

1 kA/m = 12.566 Oe 1 kOe = 79.577 kA/m

Figure A.2: Properties of N30UH class magnet acquired from [10].

APPENDIX B: Winding layouts.

Table B.1 : Winding layout of 27-slot 8-pole combination.

	Phase A		Phase B		Phase C	
Coil	In	Out	In	Out	In	Out
1	1	4	19	22	10	13
2	1	25	19	16	10	7
3	7	4	25	22	16	13
4	8	11	26	2	17	20
5	14	11	5	2	23	20
6	14	17	5	8	23	26
7	15	18	6	9	24	27
8	21	18	12	9	3	27
9	21	24	12	15	3	6

Table B.2 : Winding layout of 48-slot 8-pole combination.

	Phase A		Phase B		Phase C	
Coil	In	Out	In	Out	In	Out
1	1	7	5	11	9	15
2	2	8	6	12	10	16
3	13	7	17	11	21	15
4	14	8	18	12	22	16
5	13	19	17	23	21	27
6	14	20	18	24	22	28
7	25	19	29	23	33	27
8	26	20	30	24	34	28
9	25	31	29	35	33	39
10	26	32	30	36	34	40
11	37	31	41	35	45	39
12	38	32	42	36	46	40
13	37	43	41	47	45	3
14	38	44	42	48	46	4
15	1	43	5	47	9	3
16	2	44	6	48	10	4

APPENDIX C: Test results of the magnet materials.

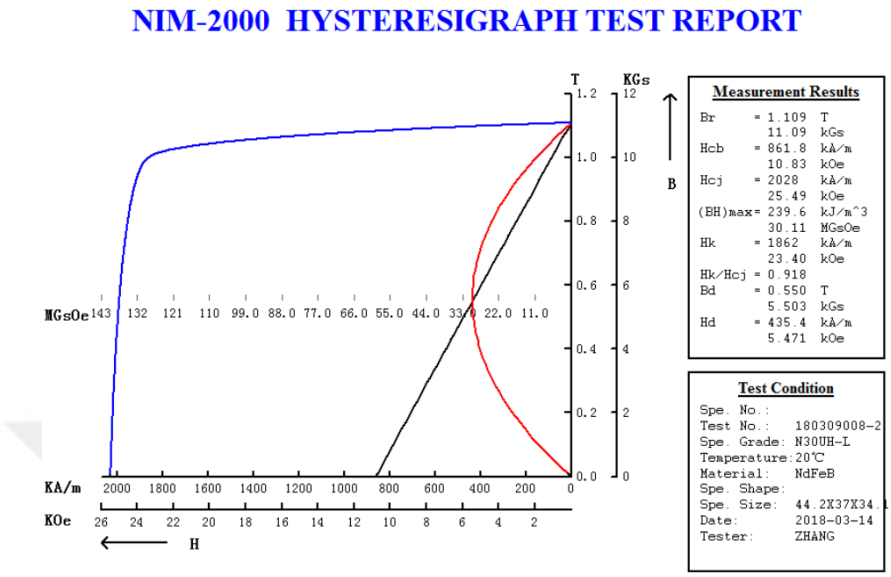

Figure C.1 : Hysteresigraph test of the IPM magnets used in prototype motor.

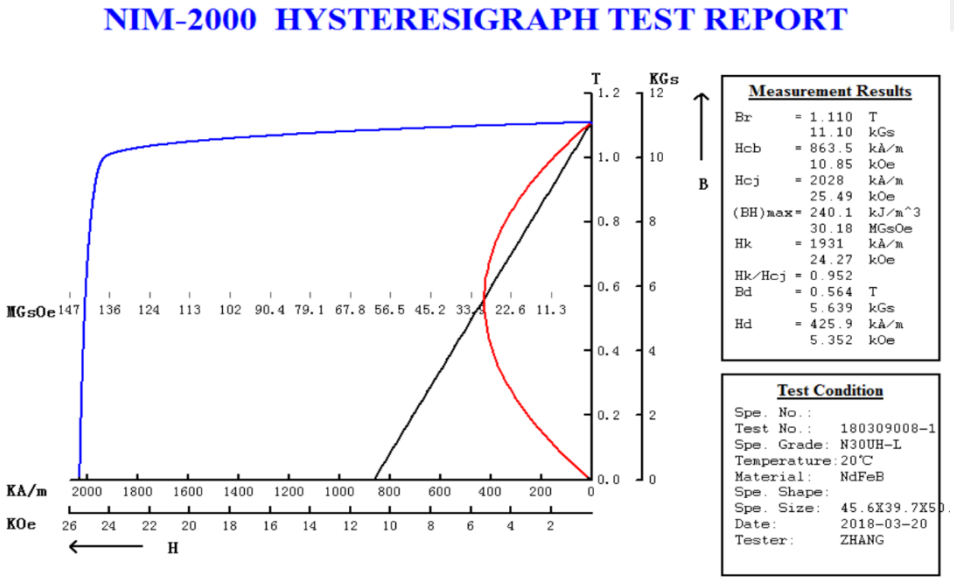

Figure C.2 : Hysteresigraph test of the SPM magnets used in prototype motor.

CURRICULUM VITAE

Name Surname : Oğuz Korman

Place and Date of Birth : Nicosia – 04/06/1993

E-mail : oguz.korman@gmail.com

Education

- **B.Sc** : 2015, Istanbul Technical University, Faculty of Electrical and Electronic Engineering, Electrical Engineering
- **M.Sc** : Continues, Istanbul Technical University, Faculty of Electrical and Electronic Engineering, Electrical Engineering

PROFESSIONAL EXPERIENCE AND REWARDS:

- (2017-), Electromagnetic Design Engineer, Akım Metal San. Tic. A.Ş

OTHER PUBLICATIONS, PRESENTATIONS AND PATENTS:

Ulu, C., Korman, O., Kömürgöz, G. 2017**.** Electromagnetic and Thermal Analysis/Design of an Induction Motor for Electric Vehicles. *ICMAE 2017*